S. R. Iovanovici

Particle Concentration Measurements using Laser Doppler Anemometry

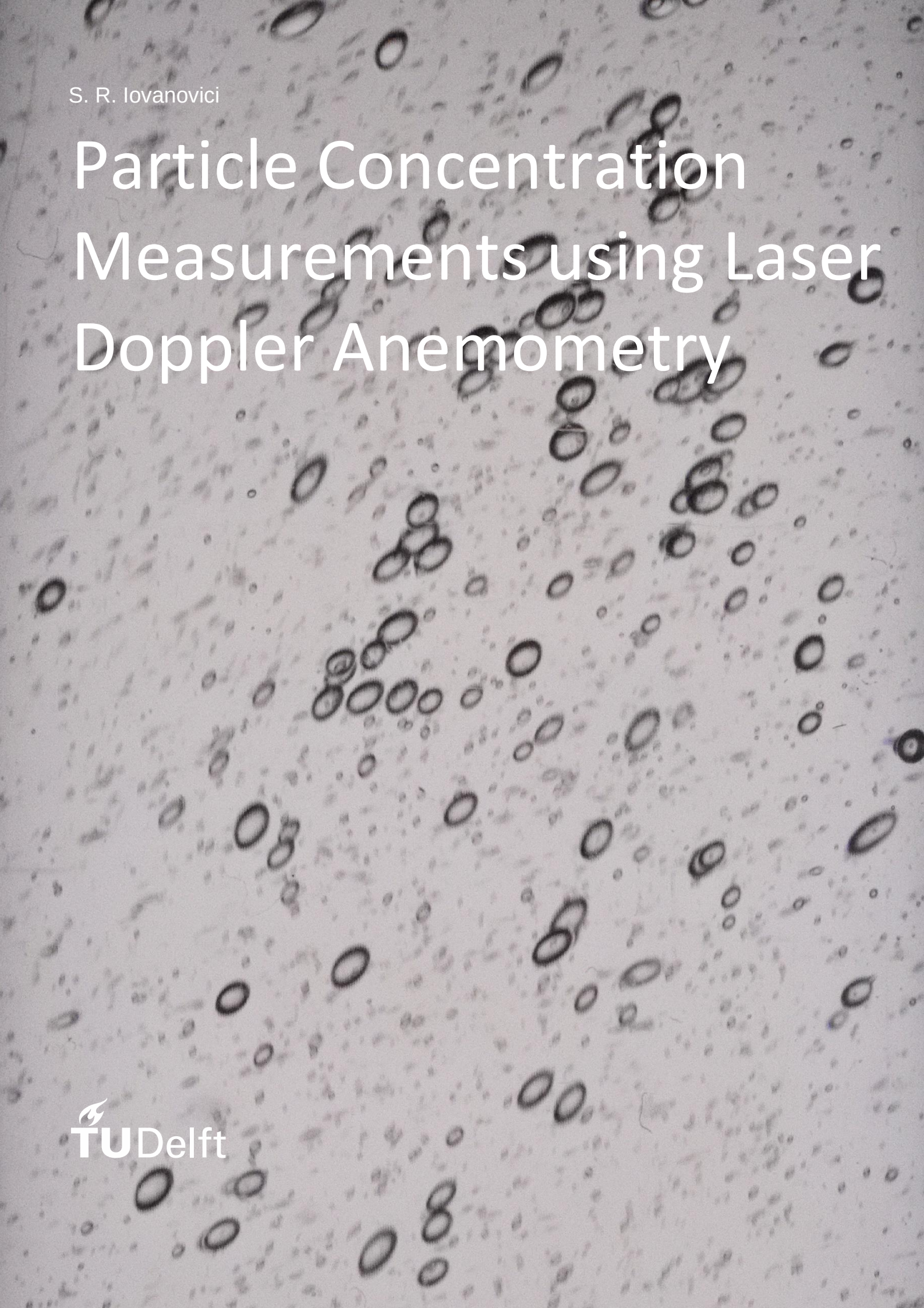

TU Delft

Particle Concentration Measurements using Laser Doppler Anemometry

By

S. R. Iovanovici

in partial fulfilment of the requirements for the degree of

Master of Science
in Applied Physics

at the Delft University of Technology,
to be defended publicly on Monday January 30, 2023 at 9:30 AM.

Supervisor:	Dr. ir. M. Rohde	TU Delft
Thesis committee:	Dr. ir. M. Rohde	TU Delft
	Prof.dr. A.P. Siebesma	TU Delft
	Prof. dr. ir. Jan Leen Kloosterman	TU Delft

TU Delft

Contents

Acknowledgements

Several people provided considerable support in making this study. Dick de Haas helped with the initial start-up of the project. He provided guidance in operating the Laser Doppler Anemometry equipment and explained some of the methodology that he had used in prior measurements. John Vlieland provided helpful documentation, made adjustment to the mounting of the flotation column and was always available for questions regarding lab procedures. With regards to measurements of particle sizes using DLS and TEM, Eline van den Heuvel provided a considerable contribution in planning out and performing these measurements. The provided software for analysing the DLS data and the accompanying documentation was also greatly appreciated. Finally, Martin Rohde, as the supervisor of this study, provided great insight into the interpretation of results and into the direction of the study through discussing the results on a (bi)-weekly schedule. Additional effort in reviewing this study prior to submission was also of great importance.

Abstract

Globally, a renewed interest in nuclear power has developed over the recent years due to increasing energy demands and to fulfil climate goals set for 2050. To succeed older nuclear power plants that are planned to be decommissioned around or after 2030 and to address current concerns regarding safety and sustainability with the current use of nuclear power, a new fourth generation of nuclear reactor designs has seen significant research and development. One of the proposed designs related to this study is the Molten Salt Reactor (MSR). Noble metal fission products in MSRs have been known to deposit on crucial reactor components which reduce their effectiveness and their lifetimes. A well-studied method known as Helium bubbling is one of the proposed methods of extracting these solid fission products. Prior studies on Helium bubbling have been carried out at the TU Delft using Laser Induced Fluorescence (LIF). However, as the application of LIF is limited, a new method of measuring particle concentrations in liquids is needed to perform measurements on actual molten salt.

In this research a different method known as Laser Doppler Anemometry (LDA) is proposed for studying particle concentrations during bubbling. LDA is an optical laser-based technique which relies on the Doppler effect to measure the velocities of particles crossing a local measurement volume of a few mm in size. Using inverse velocity weighting, a relative particle concentration can be computed by eliminating the flow rate dependency of the rate at which particles are detected. The use of LDA is investigated for two- and three-phase flows using molybdenum particles of different sizes in demineralized water and aqueous glycerol. Three-phase flow measurements have been carried out using a Perspex flotation column and the influence of several parameters has been investigated: the gas flow rate, the particle size, and the measurement depth.

Measurements in two-phase flows have shown that inverse velocity weighting is a viable strategy for relative concentration measurement of monodisperse particles by compensating the flow field dependency and that the correlation between the measured signal and the amount of powder used is linear. Similar to literature, the addition of a gaseous phase in the flotation column has been observed to result in time gaps in the data due to the blocking of one of the laser beams or the measurement volume itself. To quantify the magnitude of this effect, variations in the gas flow rates and measurement depths were utilized to compare the result to relations found in literature. However, the results remain inconclusive due to a large number of data point being rejected. Furthermore, three different filters were investigated to minimize the influence of bubbles on the measured particle concentration, which have shown to produce mixed results depending on the used particle size, sample weight and liquid. Finally, calibration curve measurements were carried out in aqueous glycerol and water which have shown that the increase in viscosity is problematic for measurements using Laser Doppler Anemometry due to the higher number of bubbles observed and due to the larger overlap of the velocity distributions of bubbles and particles.

1. Introduction

With an ever surging demand for energy and rising concerns regarding climate change, the need for large scale low-carbon footprint energy production technologies is increasingly recognized by countries all around the world. Where nuclear power in particular, can provide an excellent base load solution for use alongside other sustainable energy sources. It is only until the recent decades that a significant number of countries have started to show a renewed interest in starting new nuclear power programs and expanding existing ones [1]. More than forty developing countries have shown interest in starting a nuclear program [2], and other countries such as China, Russia, India and Korea are projected to expand their nuclear power capacity significantly in the following thirty years [1]. Within the current climate goals, projections indicate that nuclear power will have a significant relevance in meeting the world energy demand and for reaching current climate goals set for 2050.

Despite the renewed interest, a multitude of concern and challenges with regards to nuclear power remain, especially after the events of Chernobyl and Fukushima Daiichi have shown what kind of impact nuclear accidents can have on the life and health of humankind. The impact of these events on public opinion and governmental policies has been significant, as in their wakes, the construction of new nuclear power plants has been relatively stagnant during the past thirty years up until now [3].

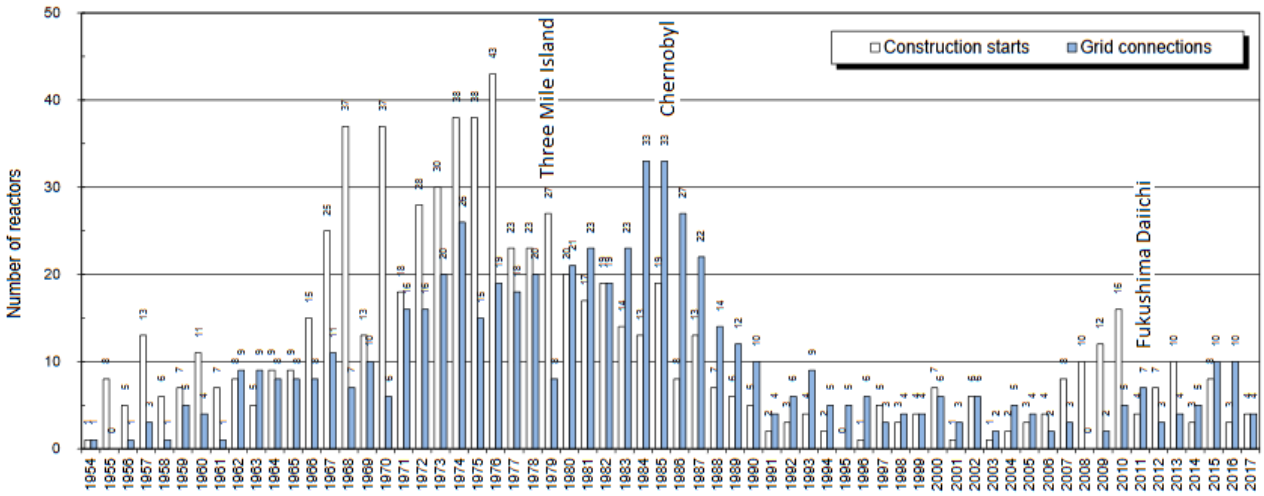

Figure 1. The number of reactor construction starts and grid connections per year [3].

With the future prospects of nuclear power in mind, research and development has already started in the process of addressing existing concerns and to use the experience gained from the development and construction of second and third generation reactors to develop several promising fourth generation reactor designs. Designs which are expected to reach commercial viability near or after 2030, when many nuclear power plants in the world will be at or near the end of their operating licenses [4].

1.1 Generation IV Reactors

The collaborative international endeavour known as the Generation IV International Forum (GIF) was officially formed in 2001 in a joint effort for the research and development of fourth-generation nuclear energy systems as to work towards new sustainable sources of energy [5]. The original goals and challenges set in the 2002 Roadmap and the 2014 Roadmap Update are summarized as followed [4]:

- Sustainability: sustainable energy generation and the promotion of long-term availability of nuclear fuel, minimization of nuclear waste and the reduction of the long-term stewardship burden.
- Safety and reliability: excel in safety and reliability, a very low likelihood and degree of reactor core damage and the elimination for the need of offsite emergency response.
- Economics: having a life cycle cost advantage over other energy sources and having a level of financial risk comparable to other energy projects.
- Proliferation resistance and physical protection: be a very unattractive route for diversion or theft of weapon-usable materials and provide increased physical protection against acts of terrorism.

Additionally, another set of research goals were introduced after the Fukushima Daiichi accident, which relate in particular to [6]:

- The use of non-water coolants in most gen-IV designs,
- higher operating temperatures,
- higher reactor power density.

These six most promising nuclear energy designs as proposed in the roadmap are summarized in Table 1.

Table 1. Summary of the selected six nuclear systems [5].

System	*Neutron spectrum*	*Coolant*	*Outlet Temperature °C*	*Fuel cycle*	*Size (MW_e)*
VHTR (Very-high-temperature reactor)	Thermal	Helium	900-1000	Open	250-300
SFR (Sodium-cooled fast reactor)	Fast	Sodium	500-550	Closed	50-150 300-1500 600-1500
SCWR (Supercritical-water-cooled reactor)	Thermal/fast	Water	510-625	Open/closed	300-700 1000-1500
GFR (Gas-cooled fast reactor)	Fast	Helium	850	Closed	1 200
LFR (Lead-cooled fast reactor)	Fast	Lead	480-570	Closed	20-180 300-1200 600-1000
MSR (Molten salt reactor)	Thermal/fast	Fluoride salts	700-800	Closed	1000

1.2 The Molten Salt Reactor

The MSR (Figure 2) is a distinct class of high temperature reactor systems in which the traditional solid fuel is replaced by a circulating liquid salt in which fissile and fertile materials are dissolved. The salts used in MSRs, usually consisting of a mixture of lithium- and beryllium-fluoride, are highly suited for use in nuclear reactors as they can act as a nuclear reaction medium, a heat transfer medium and as a chemical processing medium simultaneously [7]. Furthermore, the usage of fuel salt also exhibits desirable properties in relation to the enhancement of nuclear reactor safety [4] [8]:

- Highly negative temperature and void reaction coefficients, meaning that as temperature rises, the reaction speed slows down, making the reactor self-regulated.
- Low operating pressures and reduced structural stresses.
- A low inventory of volatile fission products.
- The possibility for fail-safe draining of the fuel salt in sub-critical tanks through the use of freeze plugs.

While MSRs are often discussed in relation to breeding with a closed thorium fuel cycle to minimize the contents of long-lasting radioactive content in waste, the fluid nature of the fuel salt together with a high neutron economy in MSRs also allow for the burning of existing transuranic actinides, resulting from the uranium-plutonium cycle, through the blending of actinide feeds into the fuel salt [8]. Additionally, high fuel burn-up, high flexibility in fuel choice and the possibility for breeding all promote sustainability and long-term availability of nuclear fuel, while the fluid nature of the MSR also allows for on-line reprocessing of fuel salt through a combination of pyrochemical processes and a process called helium bubbling.

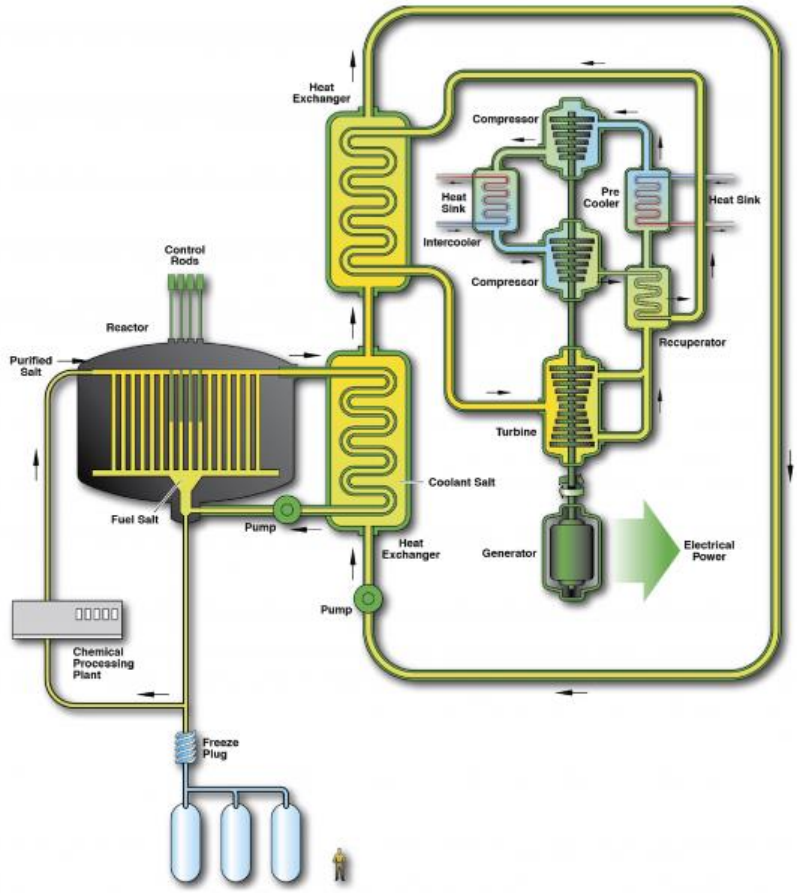

Figure 2. Illustration of a molten salt reactor concept, showing both core components and the scale of the reactor [9].

Research on the MSR concept can be traced back as far as in the late 1940s, when researchers at the ORNL investigated the potential use of fluid fuels in nuclear reactors. Molten salts in particular, were considered due to their stability to high temperatures and radiation, as well as their heat transfer properties and the large solubility of uranium [10]. However, it was not until 1954, when the first actual demonstrator of the MSR concept was realized during the military oriented Aircraft Reactor Experiment (ARE), a program dedicated to the design of nuclear-powered aircrafts. While interest in the program faded, the ARE did at that point in time demonstrate the chemical stability of uranium (IV)-fluoride and showed that the MSR concept was stable and self-regulating through the large thermal expansion coefficient of the fuel salt and the semi-automatic removal of gaseous fission products [8] [11]. Subsequently, the initially promising results from the ARE led to the research and development of a number of concepts intended to be used for civil power production. The resulting program known as the Molten Salt Reactor Experiment (MSRE) operated successfully throughout the 1960s and demonstrated the viability of the MSR while also being the first reactor to use U-233 as fuel [10]. Moreover, the final operating stage of the MSRE was used to conducted a series of experiments relating to various processes in the reactor, such as the stripping of xenon gas and the migration of fission products. Advancements in the reprocessing flowsheet and experience gained from both the ARE and the MSRE led to the proposal of an advanced concept, the Molten Salt Breeder Reactor. However, despite the success of the demonstrators, the MSR program was closed down in the early 1970's in favour of other concept designs [8] [10].

Currently, the Molten Salt Fast Reactor (MSFR) concept operating on a thorium cycle has been selected as the baseline concept for further research and development. While the performance of MSR has been a relatively well studied aspect, further research and development needs to be conducted on the following aspects [6]:

- The physical-chemical behaviour of fuel salts.
- The compatibility of salt with structural materials for fuel and coolant circuits.
- The instrumentation and control of fluid salt.
- Fuel processing of the molten salts.

1.2.1 The Extraction of Fission Products from Molten Salt

One of the large advantages of the liquid nature of the fuel stems from the possibility of continuous on-line treatment and the extraction of fission products that negatively impact the performance of the reactor. The fission products generated in the fuel salt can readily be divided into three different categories according to their chemical properties within the fuel salt [7]:

- Rare gas elements.
- Salt soluble elements (e.g. lanthanides).
- Salt insoluble elements (e.g. noble metals).

Several extraction techniques are currently being researched to separate the various classes of fission product from the fuel salt. As an example, fluorination of the molten salt may be used to extract actinides from fuel salt while electrochemical reduction and oxidation techniques may be used to extract zirconium and rare earth elements (lanthanides) [12].

An extraction technique for the removal of fission gasses, known as helium bubbling, was proposed in the early 1970s by the ORNL for use in the Molten Salt Breeder Reactor program. In this proposal, helium is injected into a bypass of the fuel salt stream through the use of Venturi type bubble generators to remove fission gasses such as xenon and krypton, which act as neutron poisons in the fuel salt [13]. Observations

made during the studying of the migration of noble metals in the MSRE program suggested that the gas-liquid interfaces inside the fuel salt stream represent stable surfaces for noble metal deposition [14]. It is has therefore been proposed that noble metals may also be extracted through helium bubbling by a process called flotation, a process that is widely used in the mineral processing industry, the waste-water treatment industry and traditionally, the mining industry. In this way the deposition of the noble metal fission products on vital reactor circuit components would be minimized and the lifetime of said components increased.

1.2.2 Recent Research

In the recent few years several new collaboration projects have been started in the European union to further develop and mature the key components of the Molten Salt Reactor. As part of SAMOSAFER (Severe Accident MOdeling and Safety Assessment for Fluid-fuel Energy Reactor), a project of Horizon Europe, research has been performed at the Reactor Institute Delft (RID) to investigate the mechanics behind fine particle flotation under differing experimental conditions while using different simulant materials in place of molten salt.

More specifically, Capelli has produced a number of works in which she investigated the recovery efficiencies of iron and micron-sized molybdenum particles under different experimental conditions [15]. Her work was continued in 2020 when Rozing produced a thesis in which he modeled the flotation process in OpenFOAM, a computational fluid dynamics package [16]. Subsequent experimental work was carried out post covid lockdowns by Lakerveld in which he studied the recovery efficiency of nano-sized polystyrene particles using Laser Induced Fluorescence (LIF) [17] and further research and improvements to the same setup were carried out by Grooten [18].

While the thesis of Lakerveld has shown that LIF can be used to good effect in studying the flotation efficiency of polystyrene particle, the requirement of using fluorescent materials limits the selection of which types of particles can be studied. Hereby limiting its use for potential further studies involving molten salt. As such, a different measurement technique called Laser Doppler Anemometry, also known as Laser Doppler Velocimetry, was proposed under the MIMOSA (MultI-recycling strategies of LWR SNF focusing on MOlten SAlt technology) project for measuring particle concentrations.

1.3 Thesis Scope

Laser Doppler Anemometry is a measurement technique that uses the well-known Doppler effect to measure the velocity of particles in transparent or semi-transparent flows and is applicable in both gasses and fluids. The technique has been widely used in flow analysis in particular. An overview of the process is given in Figure 3.

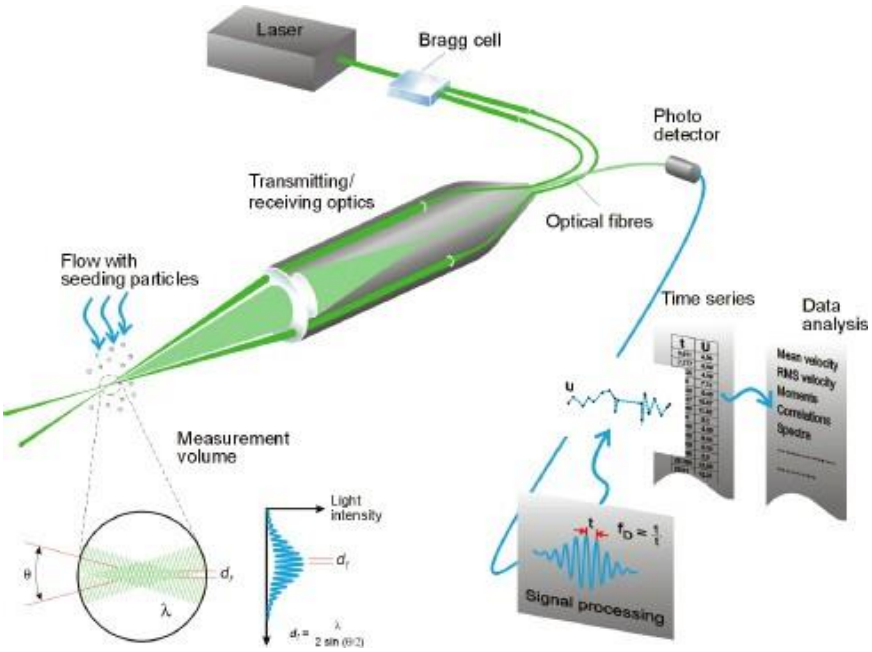

Figure 3. Overview of all the aspects of Laser Doppler Anemometry [19].

While widely used in flow research, there has only been a relative few use cases in which LDA is used for measuring particle concentrations. Expanding on this, the aim of this study is to use the same experimental setup that was used by Lakerveld and Grooten to ascertain the viability and to find potential pitfalls in using LDA to measure particle concentrations in three phase flows. Contents are intended to aid future researchers in developing a suitable strategy for using LDA to measure particles in real molten salt, whereas this study is limited to the use of simulants only. The goal of this research is to study LDA measurements of the remaining particle concentration inside a flotation column. More specifically, the following sub questions are defined:

- Using only solid particles in a fluid, how do the LDA measurements depend on a number of parameters, including: the number of particles, the measurement depth, the fluid flow velocity and the particle size?
- How does the addition of a gaseous phase impact the measurement results?
- How does the number of detected particles / the data rate depend on the measurement depth and the gas flow rate?
- How can the impact of the bubbles be minimized and what characteristics of the solids and the bubbles can be used to improve the accuracy of the results?
- Using 1D LDA in a three-phase flow, how does the measured local particle concentration vary with the number of particles, the particle size and the measurement time?
- For a series of different concentration measurements under similar experimental conditions, how consistent are the measurement results?

2. Theory

Contents in this chapter are intended to introduce more of the theoretical side of LDA together with the key principles behind the use of LDA for particle concentration measurements. Additionally, the added complexity of moving from simple two phase flows to three phase flows is discussed and finally, details are given regarding the flotation process that lies central to the use of a flotation column.

2.1 Laser Doppler Anemometry

The following theory presented in section 2.1 is partially based on material presented in the LDA and PDA reference manual produced by Dantec Dynamics [20] and a lab manual provided by former research assistant De Haas at the RID, additional reading material, including a comparison between several techniques can be found in the following references: a paper by Jensen [21] and an informational document by MIT [22].

As mentioned in the introduction, a laser anemometer is an optical instrument used and developed specifically for studying flows in gasses and liquids. Advantages of LDA compared to some other optical and non-optical techniques are:

- The optical nature of the technique allows for performing measurement on flows without physically interfering with the flow itself. The requirements are that there is a sufficient sampling rate and that the medium is (semi-)transparent.
- Calibration is typically not needed and the signal response is entirely linear with regards to the flow velocity. Due to the technique being based on electromagnetic waves, the technique is mostly unaffected by changes in the experimental setup (e.g. pressure, temperature).
- High spatial and temporal resolution due to the small measurement volume and fast processing of signals, allowing for precise local measurement as a function of time.

A typical LDA setup consists of a number of distinct components, including: a laser, a beam splitter, a Bragg cell to shift the frequencies of one of the beam, an optical arrangement, a photoreceiver, a signal processor and a data analysis system. An overview is given in Figure 4.

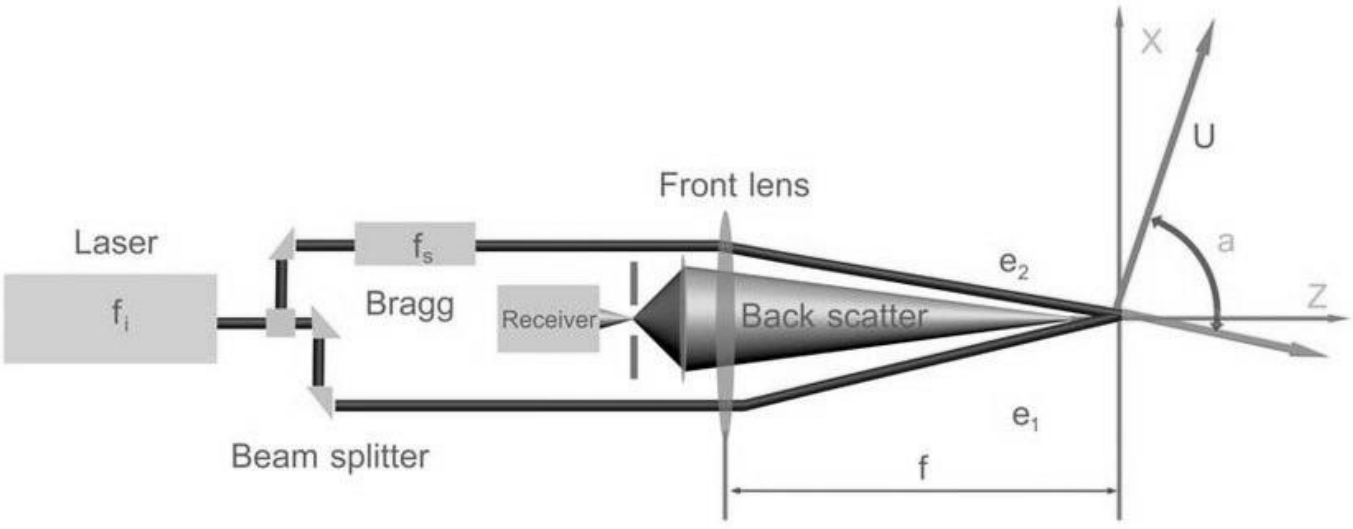

Figure 4. Overview of the LDA components [23].

The converging beams form a measurement volume, which is typical in the order of a couple of mm long, where particle velocities are measured by detecting the scattered light. The scattered light is observed by the receiver and subsequently filtered by the signal processor.

2.1.1 The Doppler Effect

As the name Laser Doppler Anemometry implies, the Doppler effect plays a primary role in the working principles of LDA. Under Doppler effect theory, when incoming light scatters from a moving particle, the observer experiences a shift in frequency in the scattered light with a magnitude directly proportional to the velocity of the moving particle.

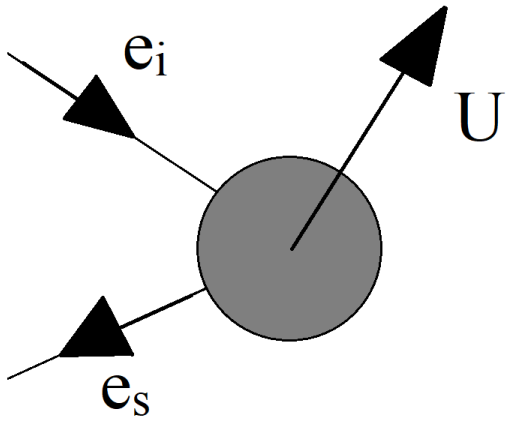

Figure 5. Illustration of light scattering from a moving particle.

An illustration of such a scenario is depicted in Figure 5 above, where U is the speed of the particle and e_i, e_s are the unit vectors of the incoming and scattered light respectively. The frequency of the scattered light, f_s, can be calculated given the following expression, where the speed of light is indicated by c:

$$f_s = f_i \frac{1 - e_i(U/c)}{1 - e_s(U/c)} \tag{1}$$

In practise, the velocity of the measured particles is much lower than the speed of light, i.e. $|U/c| \ll 1$, which simplifies the above expression to:

$$f_s \cong f_i + \frac{f_i}{c} U * (e_s - e_i) = f_i + \Delta f \tag{2}$$

Where Δf is the observed Doppler shift relative to the frequency of the incoming light f_i.

2.1.2 The Fringe Model

While it is in principle possible to determine the particle velocity by directly measuring the above Doppler shift, in practise, the shift is often much too small to accurately measure unless the particle velocity approaches the speed of light.

A more common alternative setup, as can be seen in Figure 4, uses a set of two beams with identical frequencies to obtain a much more practical approach for typical particle velocities. When two incoming beams scatter of the same particle under slightly different angles we can see from Equation 2 that the scattered light from the two different sources obtain a slightly different Doppler shift. This difference

results in an interference pattern with alternating light and dark fringes due to constructive and destructive interference.

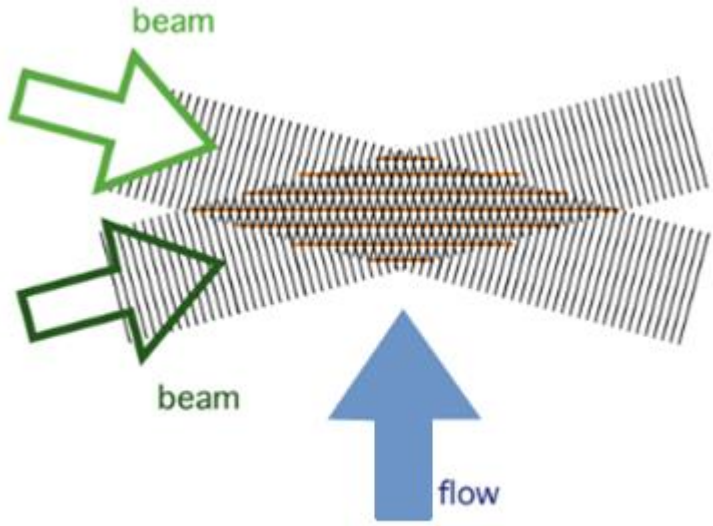

Figure 6. Fringe model showing the interference pattern produced by two intersecting beams [22].

If we define the beat frequency, or also known as the Doppler frequency f_D, of this interference pattern as the difference in frequency from the scattered light of both sources we see that the Doppler frequency is actually directly proportional to the in-plane component of the particle velocity (here taken as u_x):

$$f_D = f_{s,2} - f_{s,1} = f_i\left[\frac{U}{c} * (e_1 - e_2)\right] = \frac{f_i}{c}[|e_1 - e_2| * |U| * cos(\varphi)] = \frac{2sin\left(\frac{\theta}{2}\right)}{\lambda}u_x \qquad (3)$$

Here, φ is the angle between the receiver and the particle velocity vector φ, θ is the angle between both incoming laser beams and λ is the wavelength of the incoming light. Interestingly, another result is that the vector e_s completely drops out, meaning that the result in independent of the angle at which you place your receiver. The intensity however, is still highly dependent on the direction.

Intuitively, it can be helpful to imagine that the particle itself moves through a static interference pattern of dark and light fringes, which would result in a very typical pattern, better known as a Doppler Burst, shown in Figure 7:

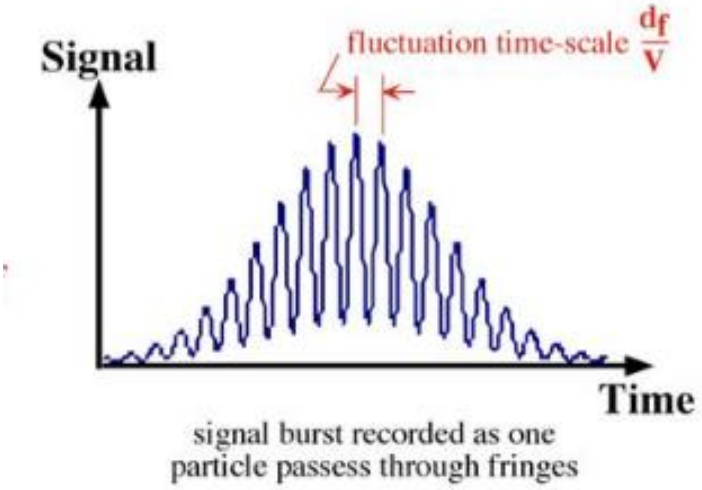

Figure 7. Illustration of a Doppler Burst pattern [22].

The burst pattern shows a Gaussian shaped signal, which is inherited from the Gaussian intensity distribution of the incoming laser beam, modulated by the aforementioned Doppler frequency, which is directly proportional to the speed at which the particles moves through the pattern.

2.1.3 Bragg Cells

Since the Doppler frequency, as given in Equation 4, is simply the subtraction between the frequencies of both scattered light beams, it also possible to obtain a negative Doppler frequency. In practise however, there is no way to make a distinction between the two, meaning that there is a directional ambiguity in the velocity component.

To resolve this problem, most modern LDA setups make use of a Bragg cell to slightly shift the frequency of one of the two beams, here denoted by the additional frequency f_0. Computing the Doppler frequency analogue to the one derived in Equation 3 gives the following expression:

$$f_{s,1} = f_i\left[1 + \frac{U}{c} * (e_s - e_1)\right]$$

$$f_{s,2} = (f_i + f_0)\left[1 + \frac{U}{c} * (e_s - e_2)\right]$$

$$f_D = f_{s,2} - f_{s,1} = f_0 + \frac{2sin\left(\frac{\theta}{2}\right)}{\lambda}u_x + f_0\left|\frac{U}{c}\right|\,|(e_s - e_2)|cos(\varphi) \cong f_0 + \frac{2sin\left(\frac{\theta}{2}\right)}{\lambda}u_x \qquad (4)$$

The introduction of the frequency shift f_0 results into two additional terms, where once again, we can use that $|U/c| \ll 1$ to simplify the expression to something very similar to Equation 3. When measuring the Doppler shift in this instance we see that the ambiguity between positive and negative frequency shifts is now lifted due to the extra constant term f_0. One thing to note however, is that the value of f_0 now forms a practical limit to how large the frequency shift can be to ensure that there is a proper measurement of u_x without directional ambiguity, more specifically, u_x is limited to roughly (using typical values):

$$u_x > -\frac{\lambda f_0}{2sin\left(\frac{\theta}{2}\right)} \approx -60\, m/s \tag{5}$$

In the aforementioned fringe model, the addition of a shifted beam can be thought of as moving fringe pattern instead of a standing pattern (as is the case for two coherent beam), which results in a Doppler burst with either a lower or higher Doppler frequency compared to f_0 based on the magnitude and direction of the measured particle. An illustration of the altered situation is shown below in Figure 8.

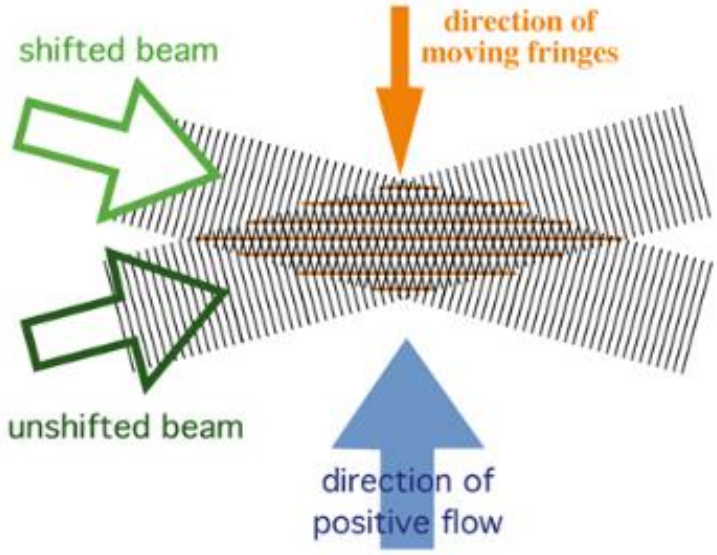

Figure 8. Fringe model showing the moving interference pattern produced by two intersecting beams with different frequencies [22].

2.1.4 Characteristics of the Measurement Volume

The measurement volume of the laser anemometer is given by the overlap of the two intersecting beams, which is ellipsoidal in shape, where d_x is the height, d_y, the width and d_z the length of the measurement volume. Below are the expression given for each quantity where d_f is the beam waist diameter, d_i the beam waist diameter before passing the front lens, f the focal length of the front lens and E the beam expansion.

$$d_f = \frac{4f\lambda}{\pi E d_i} \tag{6}$$

$$d_x = \frac{d_f}{cos\left(\frac{\theta}{2}\right)} \tag{7}$$

$$d_y = d_f \tag{8}$$

$$d_z = \frac{d_f}{sin\left(\frac{\theta}{2}\right)} \tag{9}$$

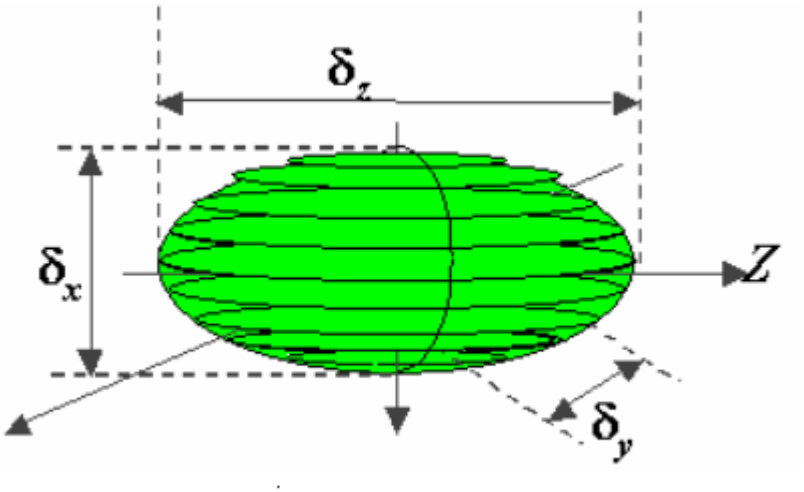

Figure 9. Illustration of the LDA measurement volume [21].

Additionally, the fringe spacing δ_f can also be computed and the expected number of fringes N_f is given by the following expressions:

$$\delta_f = \frac{\lambda}{2sin\left(\frac{\theta}{2}\right)} \tag{10}$$

$$N_f = \frac{d_x}{\delta_f} = \frac{2d_f}{\lambda} tan\left(\frac{\theta}{2}\right) \tag{11}$$

2.1.5 Seeding Particle

One of the most common use cases for LDA is in flow analysis, where various kind of particles are seeded into a flow to obtain information about the flow itself. For this to occur the particles themselves need to be large enough to scatter a sufficient amount of light while also being small enough to be able to accurately follow the stream lines of the flow. In general, the particle sizes that are able to be measured are in the order of the used wavelength of light. The motion of the particles in a fluid is affected by the following parameters:

- Particle shape
- Particle size
- Relative density between the fluid and the particle
- Concentration of particles in the fluid
- Body forces

When considering particles limited to the range of 0.1 - 50 µm in diameter, the body forces can normally be neglected, unless there is a very slow flow. For metallic particles, particles with a size of less than 10 µm are typically used. The particle-particle interactions are only of importance when the particle concentrations are significant, in practice however, concentration are typically far too low to be considered significant and are typically completely neglected.

For particles similar in size to the used wavelength of light, Lorenz-Mie scattering theory can be applied to gain insight into how much light is scattered and also into what the spatial distribution of the scattered light is depending on the size of the particle. For smaller particles, diffraction plays a larger role.

2.1.6 Phase Doppler Anemometry

While the contents of this study are limited to the use of LDA only, it is nonetheless worthwhile to mention that the working principle of LDA can be extended to also allow simultaneous measurements of the particle size. In PDA, an additional receiver is implemented alongside the original receiver. When light is scattered of a particle, the observed difference in optical path length between the two receivers gives rise to a change in phase, which can be directly related to the size of the particle itself. In this manner it is possible to simultaneously measure the velocity as well as the size of the particle. Both of which could potentially be used to perform absolute measurements of particle concentration. More details are given in the following section.

2.2 LDA Particle Concentration Measurements in Three-Phase Flows

While LDA is mostly employed as a method for flow analysis, a number of researchers have extended this concept to use LDA/PDA as a method to derive the local concentration of particles as function of a number of parameters. The key concept behind this method is to include the inverse of the particle velocity as a weight factor to eliminate the influence of the velocity field of the flow on the data rate of the measured particles. An example of why this desirable is given in Figure 10.

When the particle concentration is equal in both pipes, the number of particles measured passing through a perpendicular surface *dA* will be twice as high as in pipe B due to the higher flow speed of the fluid. In theory, dividing this data rate by the velocities of the particles themselves cancels out the extra factor 2, thereby yielding the same concentration. For this to be accurate however, it is required that the particles themselves fulfil the same aforementioned seeding particle conditions as laid out in section 2.1.5: either particle are required to be small enough such that they follow the streamlines of the fluid closely or alternatively, a well-defined correlation needs to be known between the particle velocity and the fluid velocity. The former is the case when the motion of the particles is dominated by the viscous forces as opposed to the inertial forces.

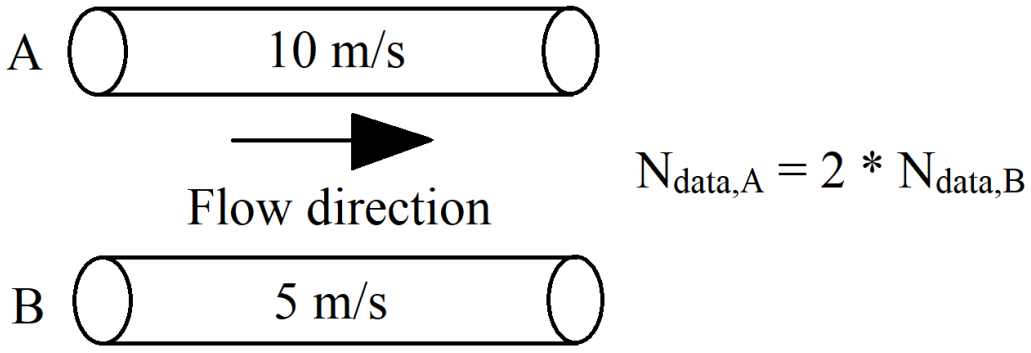

Figure 10. An example showing the dependency of the data rate on the local flow field.

While seemingly straightforward for two-phase flows, experimental difficulties arise when a gas phase is introduced to the setup. In a rather interesting study performed by Harteveld [24], where he performed LDA measurements on bubbly flow with much higher gas fractions than are typically considered, Harteveld describes the effects of the added bubbles on the LDA signals in detail. Harteveld reasons that the effects can be summarized by the following two concepts:

- Due to optical obstruction caused by the bubbles, either by blocking the individual beams or by blocking the measurement volume, extra gaps in the time dependent LDA signal occurs.
- The passage of bubbles through or close to the measurement volume generates extra fluctuations in the measured velocities due the local flow around the bubbles themselves and due to wakes in the fluid.

Similar findings were found by Mudde et al. [25] and by various other authors that were referenced in their works. Unsurprisingly, the magnitude of the optical obstruction is reported to be highly dependent on the measurement depth and the gas flow rate. In Mudde et al., based on research done by Ohba et al. [26], an expression is given for the observed exponential decay of the probability that a laser is not blocked by bubbles:

$$\frac{I}{I_0} = exp\left(-\frac{3}{2}\frac{l}{d_b}\alpha\right) \tag{12}$$

here I and I_0 are the received intensity with and without bubbles, l the path length through the fluid, d_b the mean bubble diameter and α the gas fraction. Figure 11 shows an example of the observed gaps in the LDA data signal.

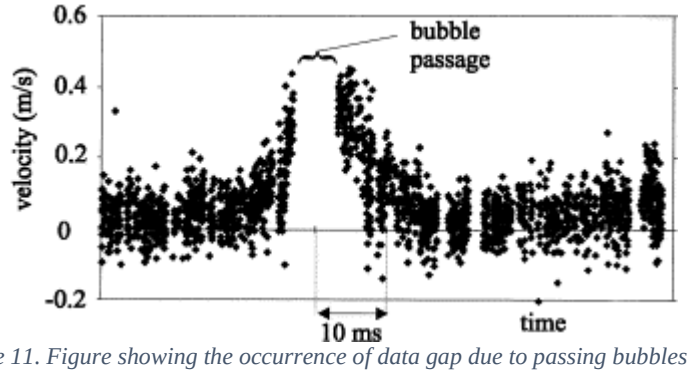

Figure 11. Figure showing the occurrence of data gap due to passing bubbles [25] .

One type of the aforementioned velocity fluctuations mentioned by Harteveld can also be seen in Figure 11; there is rapid increase and decrease in the measure velocity just before and after passage of a bubble. The other type of fluctuation is given in Figure 12 down below on the righthand side.

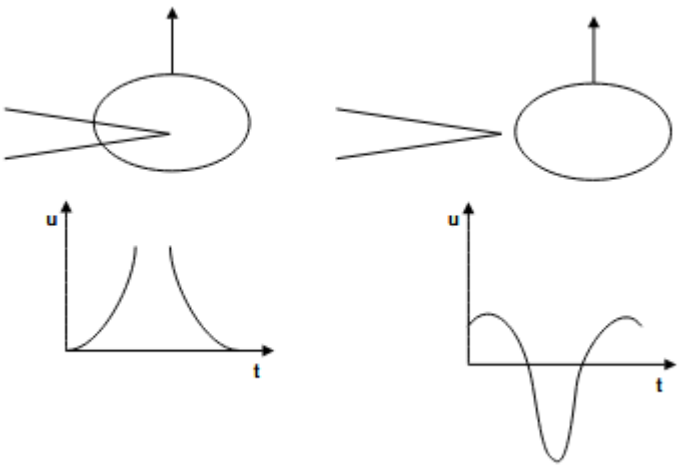

Figure 12. Illustration showing the two types of velocity realizations obtained from passing bubbles. Left: bubbles passes through the measurements volume. Right: the bubbles passes nearby the measurement volume, affecting the measurements via wakes [24].

Unfortunately, while the first type of fluctuation could theoretically be removed through some post-processing based on either the gradients, the existence of a gap or both, the second type of fluctuation is much harder to detect and to remove. The velocity gradients are much smaller in comparison and due to the lack of a time gap in the signal, these fluctuations are practically indistinguishable to normal fluctuations in turbulent flow [24].

In the remainder of section 2.2, an abbreviated overview is given of some of the available literature, specifically on the measurement of particle concentrations. For PDA, the additional information of having the particle diameter as well as its velocity leads a number of researchers to define either a solid phase fraction or an absolute solid concentration. When using LDA only, the particle diameter is not simultaneously measured, which limits the scope of the concentration measurements from a volume fraction to a particle count concentration (i.e. effective number of particles per unit of volume). In some limited cases it may still be possible to estimate a volume fraction with LDA by assuming a particle diameter, e.g. when the size distribution of the particles is known to be monodisperse prior to the measurements.

In a study performed by Gan [27], the holdup and velocity profiles of the gaseous phase and a solid phase consisting of acrylic beads om 3 mm in diameter were measured using PDA in a flotation column setup very similar to the one used in this study. Similar to the results found by Lakerveld [17], Gan found a linear relation in the gas holdup as function of the gas flow and used PDA to find a good agreement between the found velocity distributions and the available literature. Gan acknowledges the difficulties that are paired with general LDA measurements on three phase flows with high gas phase fractions, but circumvents this by limiting the gas fraction to a relatively low 2.58% and by filtering the velocity realizations using the measured diameters. A time averaged solid phase holdup was calculated using:

$$c_s = \frac{\pi}{6}\frac{1}{\Delta t}\sum_{i=1}^{N}\frac{d_i}{|U_i|}\frac{1}{A_i} \tag{13}$$

Where $c_s$denotes the solid phase fraction, N the number of samples, d_i the diameter of the measured particle, Δt the measurement time and A_i the effective probe volume cross section, which depends on the size of the particle and the illuminated probe volume. In other studies performed by Van de Wall and Soo [28], and Xinhua Liu et al. [29] a similar equation is used to compute a particle density. Additionally, Gan showed that the axial velocity distribution inside a bubble column can generally be fitted to the following relation when the velocity profiles are fully developed:

$$U(l/l_0) = (U_0 - U_w)\left(1 - (l/l_0)^m\right) + U_w \tag{14}$$

With l_0 the radius of the column, l the distance to the wall, U_0 the centerline velocity, U_w the velocity near the wall and m some fitting parameter.

Other works produced by Francke and Amouroux [30], Farmer [31] and Ayranci et al. [23] are limited to the use of LDA only, analogue to the contents of this study. Consequently, due to not being to be able to simultaneously measure the particle diameter it is not possible to derive either a phase fraction or solid concentration without detailed prior knowledge of the particle size distribution, rather, in the aforementioned works, the authors calculate a particle number density instead:

$$n = \frac{N_{data}}{\Delta t|U_i|A_i} = \frac{1}{\Delta t}\sum_{i=1}^{N}\frac{1}{|U_i|}\frac{1}{A_i} \tag{15}$$

Where n is the number density and $N_{data,i}$ the total number of data points. In the study produced by Farmer, Farmer concluded that the number density estimates that were produced with LDA were in good agreement with theoretical values and that it is indeed possible to make these estimates when careful instrumental calibration is performed. Similarly, in the work produced by Ayranci et al. a similar conclusion was drawn, however, Ayranci et al. noted that the size range in which particles were detectable with LDA was limited to the same order of the fringe spacing and that therefore, the number density estimates are only reliably possible when the particles are relatively monodisperse in the aforementioned order of size. In other words, the size range of particles that can be detected by LDA is limited and depends on the size of the fringe spacing (Equation 10). Subsequently, accurate number density measurements can only be made when the particle sizes are known to be in this range as smaller and larger particles are not detectable.

What seems to be consistent between most of the literature references is that the definition for the factor A_i and subsequent computation of this parameter is left fairly ambiguously. In most cases the value for A_i appears to be measured and subsequently used as a sort of calibration factor depending on the experimental setup and the diameter of the measured particle.

2.2.1 Gap Time Filter

To partially counteract the velocity fluctuations caused by optical obstruction of the lasers, Harteveld proposed to use two different kinds of data filters, one purely based on gap detection and another one based on gap detection with the addition of the detection of high velocity gradients. From the results he produced he concluded that the filter based on only the gap time produced a better estimate of the true turbulence spectrum albeit it being with the cost of significantly increasing the variance [24].

The basic principle behind the gap time filter is to designate a timescale T_{mingap} which is representative for the amount of time it takes for the optical obstruction to be lifted, and to remove the associated velocity fluctuations by removing data point left and right of the gap in a window of size $T_{removal}$.

Something to note is that while gaps in the data occur due to bubble passages, they may also appear sporadically due to the random nature of the sampling process. In this manner, it is possible that a gap may be falsely associated with the passing of a bubble. Harteveld noted however, that the effect that this may have on the results is negligible when to data rate is sufficient (in his use case, he had typical data rates in the order 400 counts per second). Furthermore, if the data rate is low enough to be in the same order of the bubble passage time, then the detection of bubble passages solely based on the gap length becomes impossible.

2.2.2 Mean Filter

What is possibly one of the most trivial ways to handle the additional fluctuations due to bubbles is by performing a background measurement without introducing the particles and to then subtract the obtained results from the results with the added particles. This is analogue to idea of correcting results based on a background measurement. Assumed is that:

- The velocity realizations produces by the bubbles are approximately independent of the velocity realizations produced by the solid particles.
- That the fluctuation observed in the signal of the bubbles is insignificant compare to those observed in the particles (only when looking at time series).

Implied is that the data rate of the particles should be much higher than that of the bubbles. Hence, this imposes a limit on the gas fraction and on the minimum number of particles that need to be present in the fluid.

2.2.3 Gaussian Mixed Model Filter

While discrimination between bubbles and solids based on the velocity distributions is not often cited due to potential overlap when performing measurements on bubble columns [25], there are some algorithms that may still be employed to detect and reconstruct the original solid particle velocity distribution. The Gaussian Mixed Model (GMM) is one of those.

The GMM is a machine learning algorithm that computes the probability of each data point belonging to a number of Gaussian distributions in an iterative manner. Implied here is that the number of degrees of freedom are known and that the data sets can be approximated by a Gaussian distribution. Additional reading material regarding the basic steps in GMM can be found in an online resource produced by Schlagenhauf [32]. An example of this process is given in Figure 13.

Based on observations made during measurements, there appears to be a notable overlap in the distributions, which is in agreement with some of the found literature. However, while there is overlap, the overlap is not entire. Often, two distinct peaks can be observed. As such, depending on the experimental conditions, it is still possible to separate the two to a certain degree. The observed peak for the solids in particular, appears to be well approximated by a tightly spread Gaussian distribution. For the bubble distribution however, this does not always appear to be the case.

When both the bubbles and the solids are relatively monodisperse it is likely sufficient to assume the existence of two Gaussian distributions. One way to improve the process, is to include a model selection algorithm that computes the maximum likelihood of the number of the degrees of freedom. In this study, an algorithm known as the Bayesian Information Criterion (BIC) is used to compute the likely number of required distributions.

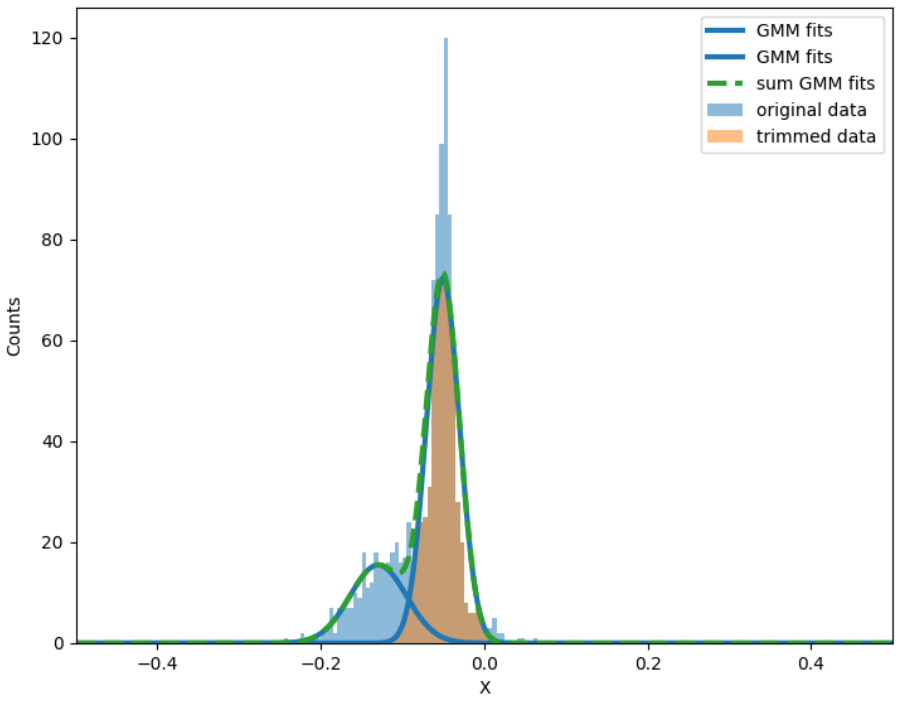

Figure 13. An example of peak detection using GMM.

2.3 Flotation Mechanics

Flotation is a separation technique used to separate materials based on their hydrophobic and hydrophilic characteristics. To this end, gas is dispersed inside aqueous solutions to lift sufficiently hydrophobic particles through buoyancy. The technique has been widely used to separate particles of varying sizes, but is limited by its flotation extraction for fine particles, particles approximately less than 10 μm in size, and for coarse particles, particles approximately more than 100 μm in size. The low flotation extraction of these classes is often ascribed to a decrease in probability of one the fundamental sub-processes of flotation, respectively, bubble-particle collision and the chance for bubble-particle detachment not to occur. The fundamental sub-processes of flotation are described in more detail in the following sections.

2.3.1 Elementary Processes of Fine Particle Flotation

The theory of flotation consists of a range of elementary processes. While physico-chemical research in flotation performed during the last few decades has resulted into a vast improvement of the theory of flotation, it was not until recently that fine particle flotation has seen a rise in interest. When fine particle flotation is considered, the flotation process can be very generally described by the following three sub-processes [33]:

- The collision between bubbles and particles.
- The attachment of particles on a bubble and the formation of a thin film between the two.
- Thinning and rupturing of the film and the formation of stable bubble-particle aggregates.

The bubble-particle collision process is characterized by the number of particles in the bubble trajectory that collide with the bubble. As such, this process is largely dependent on the collision cross-section of the bubble and the trajectories of the individual particles. For sufficiently small particles, particles approximately smaller than 50 μm in size, inertial forces can be neglected, meaning that the particle trajectories are completely dependent on the viscous forces resulting from the flow regime around the bubble [34].

After a particle collides with a bubble, a thin film is formed between the two. The particle then slides alongside the boundary of the bubble for a certain amount of time t_s, the sliding time, depending on the angle at which a particle hits the bubble. While sliding, the film is gradually thinned and drained until the film reaches a critical thickness and ruptures. The minimum time required to thin and rupture the film is known as the induction time t_i. If the sliding time is longer than the induction time, a primary hole is formed which allows for the formation of a three-phase contact [33] [34].

2.3.2 Flotation Models

As mentioned by Schulze, modelling of the flotation process has been approached from various angles, including: chemical kinetic, probabilistic and mixed models [33]. Underlying some mixed kinetic models, models in which the processes in a flotation machine are described by combining concepts used in chemical kinetics and the probabilities of the underlying elementary processes in flotation, is the assumption that the rate of bubble-particle aggregate formation and disintegration can be expressed as a kinetic equation in the form [33] [35]:

$$\frac{dc_p}{dt} = Kc_p^j c_b^k \tag{16}$$

where c_p is the particle concentration, c_b is the bubble concentration, K the flotation rate constant and j, k are the orders of the concertation terms. According to Yoon and Mao [36], previous research performed

by Sutherland, Tomlinson and Fleming has shown that mineral flotation can be described as a first-order process. This finding while assuming a constant gas flow rate, meaning that the change in bubble concentration is neglectable, allows for the above kinetic equation to be reduced to [35]:

$$\frac{dc_p}{dt} = Kc_p \tag{17}$$

After integrating the above equation and assuming that there is a maximum recovery efficiency that can be obtained, a final expression for the recovery is obtained, where R is the fraction of particle recovered and R_{max} is the maximum recovery fraction [37]:

$$R = R_{max}(1 - \exp(-Kt)) \tag{18}$$

The overall probability of a particle being successfully floated is often expressed as the product of the individual probabilities of the elementary sub-processes. Specifically, this probability is given by [33] [34]:

$$P_f = P_c P_a (1 - P_d) \tag{19}$$

where P_c is the probability of bubble-particle collision, P_a is the probability of bubble-particle adhesion and P_d is the probability of bubble-particle detachment. Non-correlation between these probabilities is assumed. In the case where fine particle flotation is considered, the probability of detachment can be omitted, as the inertial forces that play a large role in the detachment probability become sufficiently small to the point where the probability of detachment is zero by approximation [34].

A number of models have been derived by various researchers for the bubble-particle collision probability [35]. Generally, the relation between the bubble-particle collision probability and the ratio between the particle diameter and the bubble diameter is expressed in the form [34] [35]:

$$P_c = A\left(\frac{d_p}{d_b}\right)^n \tag{20}$$

where d_p is the particle diameter and d_b the bubble diameter. In particular, Yoon and Lutrell have developed fine particle flotation models for both the bubble-particle collision probability and the bubble-particle adhesion probability for different flow conditions by deriving the particle trajectories using the Stokes- and potential stream functions. Moreover, an intermediate flow condition model was derived from an empirical stream function. The intermediate model has been shown the hold up well for Reynold number smaller than 100. However, whether the intermediate model holds for larger Reynold numbers is uncertain [34]. Expressions for the parameters *A* and *n* are given in Table 2.

Table 2. Bubble-particle collision probability model derived by Yoon and Lutrell [34].

Flow Conditions	$\boldsymbol{A}$	$\boldsymbol{n}$
Stokes ($\boldsymbol{Re \ll 1}$)	$\frac{3}{2}$	*2*
Intermediate	$\frac{3}{2} + \frac{4Re_b^{0.72}}{15}$	*2*
Potential ($\boldsymbol{Re \gg 100}$)	*3*	*1*

The aforementioned bubble-particle adhesion probability model is given by [34]:

$$P_a = \sin^2\left[2\arctan\exp\left\{\frac{-3u_b t_i}{2r_b\left(r_b/r_p+1\right)}\right\}\right] \tag{21}$$

for the Stokes flow conditions,

$$P_a = \sin^2\left[2\arctan\exp\left\{\frac{-\left(45+8Re^{0.72}\right)u_b t_i}{30r_b\left(r_b/r_p+1\right)}\right\}\right] \tag{22}$$

for intermediate flow conditions, and

$$P_a = \sin^2\left[2\arctan\exp\left\{\frac{-3u_b t_i}{2\left(r_b+r_p\right)}\right\}\right] \tag{23}$$

for the potential flow conditions. In these equations, u_b is the bubble rise velocity, r_b the bubble radius and r_p the particle radius. The stationary bubble rise velocity is expressed by Schulze as [33]:

$$|u_b| = \sqrt{\frac{4gd_b}{3c_d}} \tag{24}$$

where g is the gravitational acceleration and c_d the drag coefficient of the bubble. Alternatively, if the Reynold number of the bubble is less than 0.5, the drag coefficient may be approximated by:

$$c_d = \frac{24}{Re} \tag{25}$$

Finally, the relation between the first-order flotation rate constant and the probability of successful flotation is expressed by Yoon as a function of the superficial gas velocity u_{sg}, the probability of a particle being successfully floated and the bubble diameter [38].

$$K = \left(\frac{3P_f}{d_b}\right)u_{sg} \tag{26}$$

2.3.3 Bubble Size

When considering the relation between the bubble diameter and the flotation rate for intermediate flow conditions, the collision probability is seen to be roughly inversely proportional to the bubble diameter for large Reynold numbers and inversely proportional to the squared bubble diameter for small Reynold numbers. However, a decrease in bubble size generally also increases the probability of adhesion due to an increase in the sliding time t_s, by lowering the bubble rise velocity u_b [34]. A further decrease in bubble size results in a decrease in the sliding time t_s by lowering the sliding distance [34]. Furthermore, there is an additional inversely proportional diameter term in Equation 26. Thus, combining the two models, the bubble size appears to be of great importance for the flotation rate and while overall, the

flotation rate increases with decreasing bubble size, there appears to be an optimal bubble size after which a further decrease in bubble size decreases the flotation rate due to a decrease in adhesion probability.

2.3.4 Gas Holdup

The gas holdup of a multi-phase system can be described as the volumetric gas content of a system. According to Prakash et al. [35], the gas holdup is dependent on the bubble characteristics, the flow characteristics and the bubble rise velocity. Furthermore, the gas holdup is reportedly an important parameter for the extraction of particles in column flotation when combined with flow regime data. Studies on column flotation by Massinaei et al. [39], have shown a linear relation between the gas holdup and the bubble surface area flux S_b, which is related to the bubble size and the superficial gas velocity by:

$$S_b = \frac{6u_{sg}}{d_b} \tag{27}$$

Thus, for a constant bubble size, the gas holdup is also expected to show a linear correlation with the superficial gas velocity. Similar to the flotation rate equation derived by Yoon (10), a linear relation between the collection zone rate constant and the gas holdup has been observed [39], which means that for a constant bubble size, there is a linear relation between the collection zone rate constant and the superficial gas velocity.

While the superficial gas velocity is linearly correlated to the flotation rate according to Equation 27, the impact of the superficial gas velocity on the flow regime should also be considered. For low superficial gas velocities, the flow regime is characterized by a homogeneous bubbly flow in which formed bubbles do not coalesce or breakup. In contrast, at high superficial gas velocities, the flow regime becomes heterogeneous and, depending on the flotation column diameter, is either characterized by a slug flow regime or a Churn-turbulent flow regime [35]. It can be readily conceived that the heterogeneous nature of these high superficial gas velocity regimes alongside the wide variance in bubble size are undesirable for column flotation.

3. Methodology

The contents of this chapter are dedicated to describing the experimental setups that were used in performing the LDA measurements, as well as detailing the procedures followed in the execution of the preparation work, the measurements and the subsequent data processing. In section 3.1 two different experimental setups are described and detailed, additionally, the used fluids and solids are also described. Section 3.2 describes the used procedures and goes into detail about how the measurements were carried out alongside an overview of the different measurements. Subsequent data processing, which includes handling and uncertainty propagation is described in section 3.3.

3.1 Experimental Setup

Experimentation is done using two different experimental setups: a stirred graduated cylinder and a flotation column. With two-phase flows being more straightforward to work with, the graduated cylinder is used to explore LDA as a measurement technique in a more general sense. The goal is to ascertain the effect of a number of different parameters, such as the particles used, measurement depth and the fluid flow velocity on the resulting output. Some of the most important results of the two-phase flow measurements are added to section 4.2. Conclusions drawn from these results are instrumental for figuring out what procedures to follow during the final measurements on three-phase flows in the flotation column. Both setups are described in greater detail in subsections 3.1.1 and 3.1.2.

Common to both setups are the types of particles used and the actual LDA setup. The measurement device that is used, is a Dantec Dynamics FlowExplorer DPSS, featuring a dual laser setup with a backscatter type receiver and is mounted on a 3D traverse system. An image of this setup is shown in Figure 14 down below.

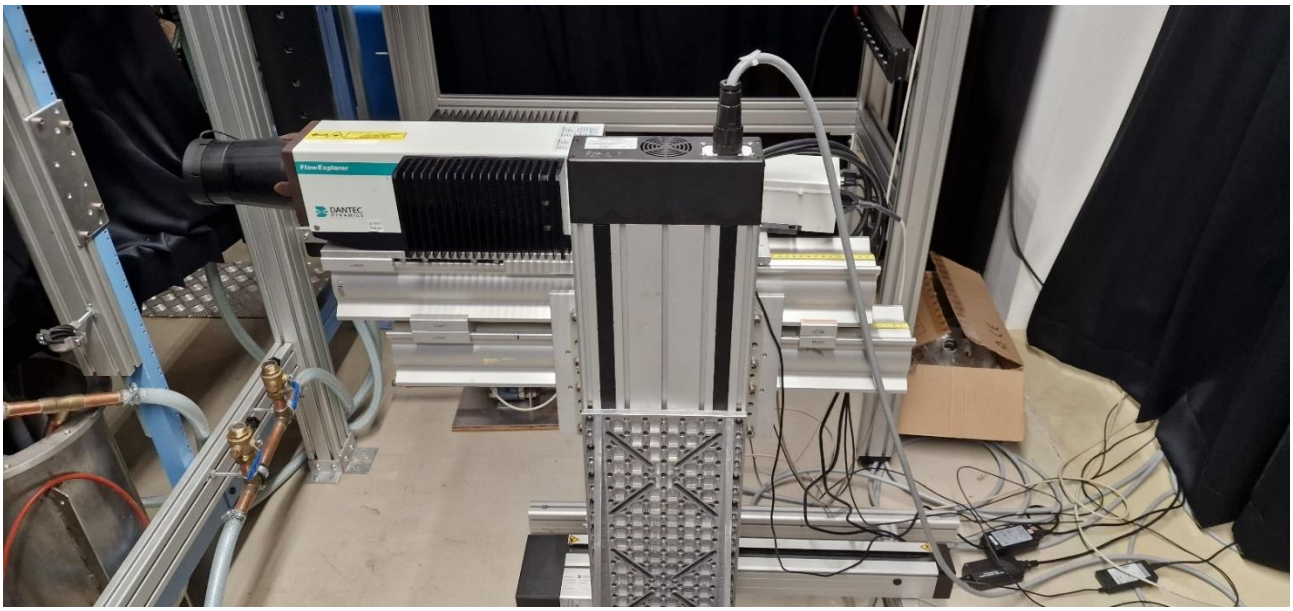

Figure 14. The LDA device mounted on a traverse system..

The dual lasers can output up to 500mW and are of a slightly different wavelength: 532nm and 561nm. Due to the different wavelengths used, discrimination between scattered light from each individual laser is possible and simultaneous measurements of both horizontal and vertical velocity components of particles can be made. Additionally, the FlowExplorer also features a swappable front lens that allows for a selection in the used focal length. Further specification can be found via the manufacturers website [19].

For consistency, a power output of 40mW per laser and a focal length of 30cm is used during all the measurements.

Signals produced by the receiver are processed on-line by a burst spectrum analyzer BSA F60 Flow Processor and subsequent velocity realizations are handled further by the accompanying BSA Flow software package on a separate desktop.

Figure 15.Top: Control unit of the traverse. Bottom: the Burst Spectrum Analyzer.

Given the potential laser output of 500mW, the classification of the used lasers fall within class 3B (this is also the case for the reported output of 40mW). As such, exposure to diffuse reflections can generally be considered safe. Though special care needs to be taken to avoid exposure to the direct and the reflected beam. Safety precautions include:

- The use of safety glasses when changing/handling the setup during operations.
- Inclusion of an interlock system connect to the lab entrance door.
- Direct shielding of the setup by black curtains.

3.1.1 Stirred Two-Phase Flow Setup

For the purpose of exploring LDA as a measurement technique and to start off with only a relatively simple two-phase flow, a graduated cylinder (Figure 16) was used. The setup is magnetically stirred to introduce fluid motion and to enhance the mixing conditions when adding in particles as test subjects, as Brownian motion alone is typically not enough to get sufficient data rates with LDA.

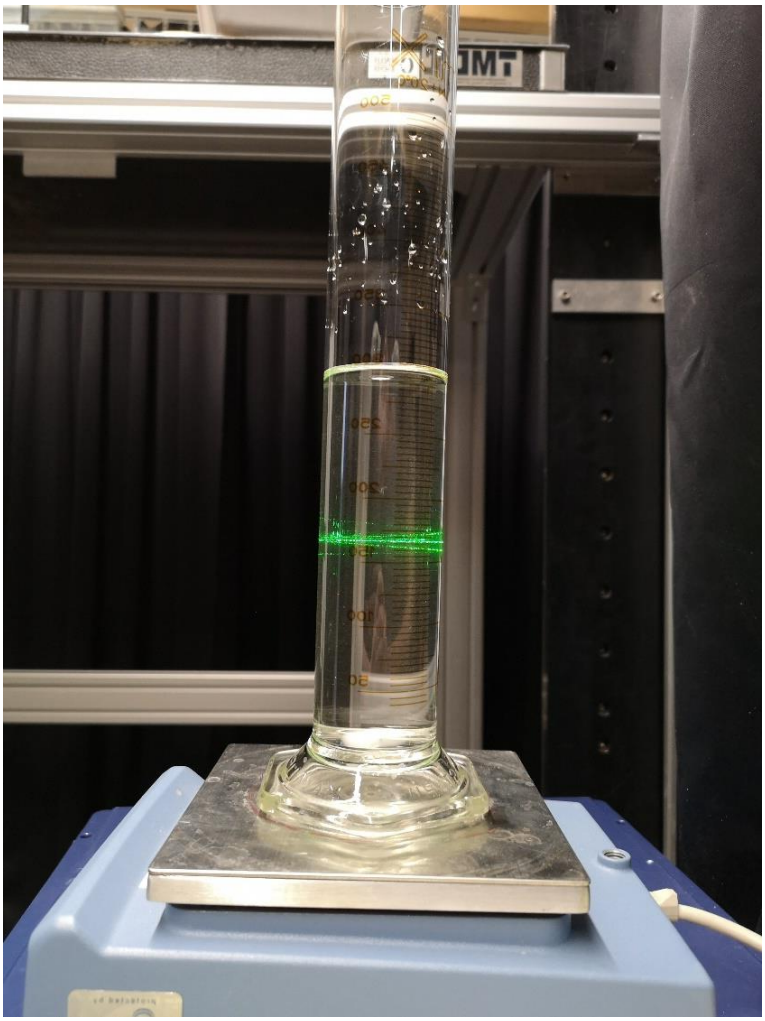

Figure 16. Graduated cylinder standing on a magnetic mixer. Used to perform measurements in two-phase flow.

3.1.2 Flotation Column Setup

The flotation column used to produce the final measurements on three phase flows (as can be seen in sections 4.4-4.6) had been repurposed from previous experiments involving the study of flotation using LIF with polystyrene seeding particles. Figure 17 shows an image of the flotation column and the accompanying design schematics. The actual flotation column has slightly different proportions than the ones states in the schematic, however, the differences have been verified to be minimal.

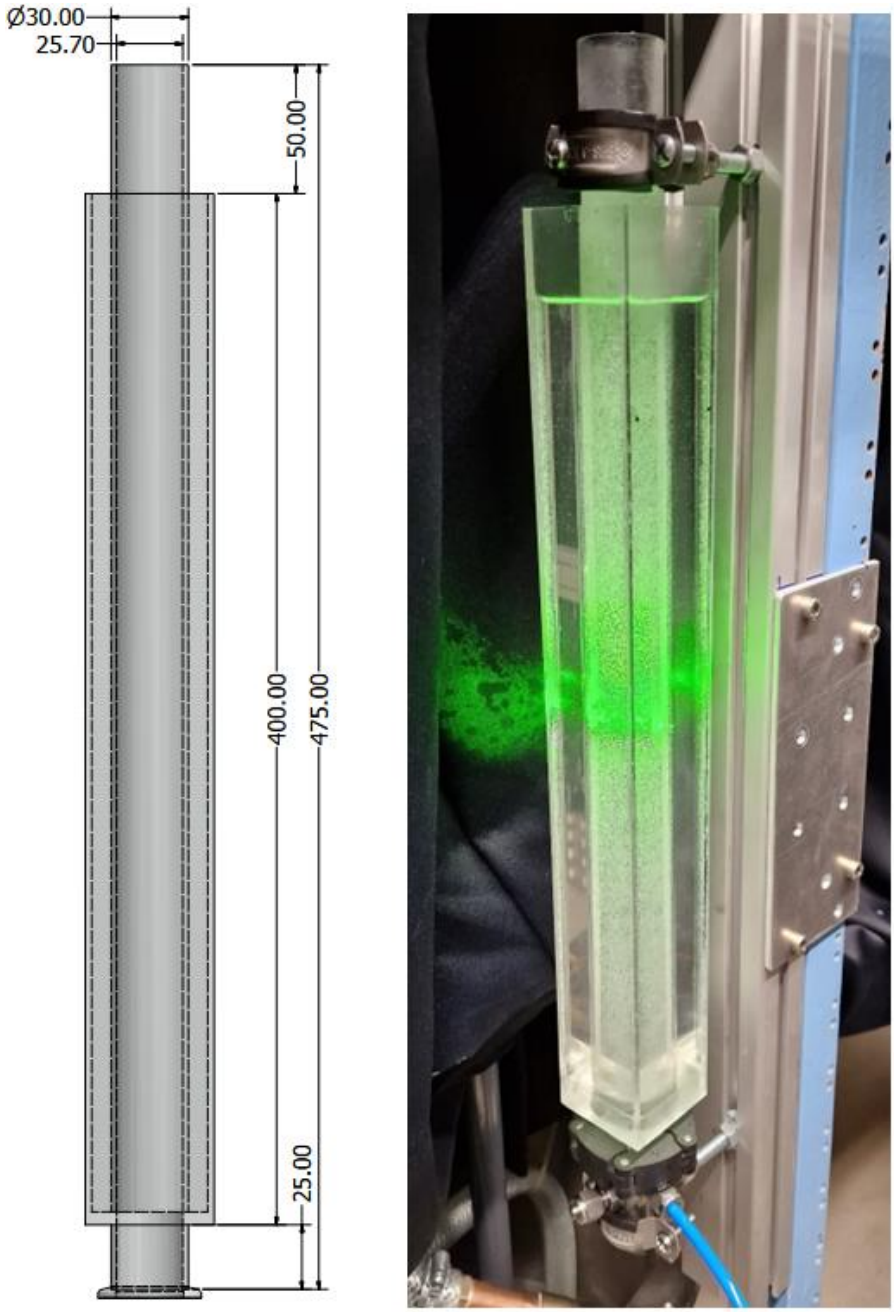

Figure 17. Left: Schematic for the column. Right: The column during operation.

The column itself is made of clear PMMA which allows for the use of optical measurement techniques. It features an inner cylindrical column in which the gas bubbles are injected and an outer rectangular column which typically only contains demineralized water. To minimalize movement of the column in between measurements, the column is secured to a frame via two brackets, on at the top and one at the bottom.

The reasoning for its design is given in a master thesis produced by Lakerveld [17]. Lakerveld reasons that when using a simple one layer cylindrical column, a significant amount of distortion can be observed due to the combination of the curved surface and the large difference in refractive indices between PMMA and air. To facilitate this transition he constructed the rectangular outer surface to first bridge the aforementioned large difference in refractive index, after which the light only has to pass through the curved surface from water to PMMA, which have refractive indices much closer to one another. Reportedly, a significant reduction in distortion is observed, particularly at the edges of the inner cylinder.

The required gas flow for the flotation column is supplied from a pressurized air supply line which is hooked up to a pressure regulator valve and a Bronkhorst EL-Flow Select mass flow controller with an accuracy of 0.5% [18]. The mass flow controller is controllable via a second desktop and operates in units of standard cubic centimeters per minute (*sccm*). Resulting from previous work produced by Anne Grooten [18], the mass flow controller had been observed to produce accurate results in the range of 5 to 25 *sccm*. However, flow rates lower than 5 *sccm* have been observed to produce inconsistent results. Bubble generation is realized by injection the outgoing mass flow to a SIKA-R3 bubble sparger with a diameter of 26 *mm* and an average pore size of 3 micron, which can also be observed in Figure 17 (bottom of the column).

3.1.3 Simulant Materials

Experimentation is performed using two different kinds of fluids, demineralized water and a mixture of water-glycerol to simulate the flow characteristics of molten salts as closely as possible. To this end, a water-glycerol mixture is used that has a similar kinematic viscosity to a LiF-BeF_2-ThF_4 (71.7-16-12.3 mol%) mixture. The volume ratio of glycerol to water that is required to achieve this is calculated through a web-based tool [40] based on parameterisation by Cheng [41]. Additional information regarding the surface tension in obtained from Mallison et al. [42]. Table 3 displays some of the properties of the molten salt mixture and the simulant fluids.

Table 3. Physico-chemical properties of the simulant fluids and the targeted molten salt composition [41] [43].

Composition	*Density* $[g/cm^3]$	*Dynamic viscosity* $[mPa \cdot s]$	*Kinematic viscosity* $[mm^2/s]$	*Surface tension* $[10^{-3}\ N/m]$	*Temperature* $[K]$
LiF-BeF_2-ThF_4 (71.7-16-12.3)	*3.342*	*10.703*	*3.202*	*185*	*900*
Water	*0.99805*	*1.0049*	*1.0068*	*72*	*293*
Glycerol	*1.2608*	*1413.8*	*1121.4*	*63.5*	*293*
Water-glycerol (65.5-34.5 vol%)	*1.0985*	*3.5564*	*3.2376*	*65.5*	*293*

To simulate the occurrence of noble metal fissions products in molten salt reactors, molybdenum particles of three different sizes are added to the fluids in separate experiments. Size ranges indicated on the used products are given as 170 mesh or 88 micron, 1-2 micron and <100 *nm* (see Appendix A for detailed images on the products used, including the glycerol). Additionally, glass bead tracer particles were also used to perform measurements on the flow during the two-phase flow measurements. Molybdenum particle concentrations in an actual single-region MSR were calculated in an ORNL publication by W.L. Carter [44], were a number of around 0.2121 g/l is given. With LDA, a data rate of a few hundred realizations per second is typically desired. For the purpose of this study, a total sample mass in the range of 1 – 20 mg was observed to provide adequate data rates for all three powders in the flotation column, meaning, data rates in the order of 100-1600 Hz.

3.1.4 Particle Collection

The aforementioned previous studies involving this flotation column [17] [18], required some sort of method to collect the particles after successful flotation. The device used to realize this is a Hallimond tube, a commonly used tool for this exact purpose (Figure 18).

Figure 18. The Hallimond tube used in previous experiments.

From personal experience and from the aforementioned studies [17] [18], the Hallimond shows a good collection efficiency when micron-sized particles are used. However, due to the growing tendency of increasingly smaller particles to follow streamlines and due to the existence of backflow in the Hallimond tube, collection efficiency is expected to be not as high for the case of nano-sized particles. Grooten reported similar findings for nano-sized particle during her thesis [18]. In an attempt to resolve the issue with fine particle flotation an effort was made to find an alternative method.

Given the hydrophobic nature of the materials used, application of an oil layer on top of the used fluid is proposed [45]. Reportedly, techniques involving the capture of metalling particles using oil have already been used in the mining industry and is known to separate the particles by capturing them in a resulting froth layer [46]. The difference however, is that typically the oil is mixed in the fluid alongside with the gas such that the particles are wetted with oil throughout the column. Nonetheless, a quick experiment whereby hydrophobic polymer particle were shaken in a container containing water and oil has shown that the particles have a high tendency to reside in the oil layer. For the experiments in this study involving the use of an oil layer, olive oil is used.

3.2 Experimental Procedure

To satisfy the research questions regarding LDA as a measurement technique for particle concentrations, several different experiments are conducted. In this subsection more details are given on the used procedures when preparing for- and performing the these measurements, as well as the data processing and the data analysis.

3.2.1 Sample Preparation & Disposal

The preparation of the samples is performed in a separate lab containing fume hoods and balances. Due to safety concerns surrounding the use of nano particles, all handling of the nano powder is done exclusively under one of the fume hoods as per the recommendations of the nano particle handling guidelines. Particles are weighed on a Mettler Toledo MS105DU analytical balance, which has maximum resolution of 0.01 *mg*, and stored in microcentrifuge tubes. A detailed summary of the procedure is given as followed:

1. The different particles are retrieved beforehand from a vacuum sealed storage.

2. The tube that is used for particle storage is placed on the balance and is used for zeroing, the balance is given roughly 10 seconds to stabilize before removing the tube.
3. Particles are added from their product containers to the tube by use of a commonly used laboratory spatula.
4. The now filled tube is placed once again on the balance and given another 10 seconds to stabilize.
5. If needed, the amount particles is adjusted by either taking particles out or by adding additional particles. Steps 4 and 5 are repeated until the target weight is achieved.
6. The tube is sealed and labelled via a marker.
7. After all the samples are prepared (where steps 2-6 are repeated), the particle containers are once again sealed under a vacuum.

To save time, sample preparation was often carried out to provide enough samples for an entire week. Due to some fluctuations while performing the measurements, the sample weights are estimated to have an uncertainty of around +/- 0.1 *mg*. All of the particle contaminated water and the water-glycerol mixtures were disposed separately in a waste container.

3.2.2 Stirred Two-Phase Flow Setup

Experiments performed on the graduated cylinder were carried out to gain experience with LDA in general. The various experiments were carried out in demineralised water where a multitude of variables were adjusted to evaluate the effect on the resulting data points. These variations include:

- Particle sizes.
- Particle amounts (i.e. variation in the total weight of the used sample).
- Particle types, the aforementioned molybdenum particle and the glass bead tracer particles.
- Different fluid velocities, which are regulated by the dial on the used mixer (see subsection 3.1.1).
- And finally, different measurements locations. Typically these are variations on the measurement depth and height in the used container.

Given the nature of the setup it unavoidable to introduce some kind of positional uncertainty in between measurements when to container is cleaned. In particular, the largest error is likely to be in the measurement depth. While it was advised to calibrate the distance by focusing the laser beam on the glass surface of the cylinder, in practise, the repeatability of this method appeared to be unsatisfactory. Instead, in order to able to compare results, measurements are repeated over the entire radius of the used cylinder, which somewhat allows for shifting the data over the radial position whenever the flow of the fluid can be deemed identical. This is the case whenever the dial of the mixer is set to the exact same position with the assumption that particle-particle interaction can be neglected. Additionally, to improve the positional inconsistency between measurements, markings were used to keep track of exact the position of the cylinder. The height level of the water was also kept at a constant level. A step-by-step is given below:

1. Water used in the previous experiments is discarded.
2. The cylinder is thoroughly rinsed with tap water followed and is repeated at the very least twice with demineralized water.
3. The cylinder is filled to a specified level with demineralized water by utilizing a wash bottle, wiped clean and seated back on the marked position on top of the mixer.
4. The mixer is turned on and the fluid is given at least two minutes to form a stabilized flow.
5. Particles are added, whereby the sample tube is rinsed multiple times, and given an additional two minutes to spread through the fluid.
6. A test measurement of roughly 30 seconds is performed to validate proper placement of the container.

3.2.3 Flotation Column Setup

The bulk of the results in this study have been derived from the flotation column setup. Resulting from experience gained from the cylinder, the used methodology was refined and the setup was adjusted to enhance the consistency between different measurements. In terms of the setup itself, brackets were added to the flotation column to facilitate better consistency in the position of the column and the frame itself was fixed.

Due to the nature of the cylindrical column the laser that is oriented in the vertical direction refracts differently than the one in the horizontal direction. Consequently, the actual measurement volumes are situated at slightly different positions which makes simultaneous measurements of both velocity components unreliable. Given the shape of the cylinder, observations made during flotation and the expected flow field [47], the vertical velocity component was suspected to be the primary velocity component. As such the calculations performed to calculate the particle number density only includes the vertical components and not the horizontal components.

Concluding from the thesis produced by Lakerveld, measurements results for LIF showed very similar results when varying the measurement height in the column, suggesting strong mixing conditions and a relative homogenous distribution of the polymer particles throughout the column. Subsequently, only one measurement height is used to save time, the height at which measurements were taken is roughly halfway up the column. Most measurement are performed at an identical depth as well, which is around 5 *mm* away from the glass surface, only the measurement involving variations in the gas flow rate are carried out over the partial diameter of the column.

From experience obtained during the measurements it became apparent that reflections can play a large role in the resulting data rates. The occurrence of reflection peaks in the resulting data is particularly large when the flat outer surface of the column is completely perpendicular to the receiver and the laser. Methodology was altered to include a slight rotation to the column to avoid the direct reflections of the beam (a few degrees at most). Consistency was maintained by rotating the abovementioned observed direct reflection to a set point before each measurement.

The action of adding the particles prior or during a measurement is also performed in a consistent manner. Firstly, the sample tube is emptied directly above the fluid surface. The tube is then halfway filled with water, thoroughly shaken and emptied (this is done twice), after which the tube is rinsed one more time. Afterwards, the inner surface of the column is also rinsed. The height of the fluid is kept constant similarly to the graduated cylinder in the two-phase flow setup and the total used fluid volume was shown to be approximately 223 +/- 2 *ml*.

The water-glycerol mixtures are prepared beforehand by adding 155 *ml* of glycerol to a gradated cylinder and by then adding the remaining demineralized water up to a total of 450 *ml*. Generally, this is just enough to cover two subsequent measurements. Due to some uncertainty resulting from a small amount of trapped air in the glycerol and due to difficulties in pouring, a small variation in the resulting mixing ratio is expected.

A step-by-step summary for the basic procedures used in the preparation of the flotation column setup is given down below (following after a previous measurement):

1. Using the direct controls of the traverse system the FlowExplorer is moved back to a position in which the laser beams are focused directly on the outer surface of the outer column.
2. The air hose is disconnect from the sparger and the flotation column is removed from the setup by loosening only the top bracket. The bottom bracket is left completely untouched.

3. The outer column is then drained first and disposed of in a sink as this only contains the water used to bridge the refraction indices.
4. Afterwards, the inner column is drained by disposing the contaminated fluid in the waste container.
5. The inner column is rinsed with tab water first and then thoroughly cleaned with demineralized water twice.
6. The outer column is always filled with demineralized water and the inner column is filled with the fluid of choice.
7. The flotation column is firmly seated in the bottom bracket once again and the top bracket is secured but not fully tightened.
8. As described above, the direct reflection is set to a specific position by rotating the column slightly. The top bracket is then fully tightened.
9. The measurement position in the column is then verified by observing that the lasers are still focused on the outer surface and by measuring the horizontal and vertical (as seen from the FlowExplorer) distance to a pair of reference dots that were placed on the column.
10. The mass flow controller is adjusted if needed and the air hose is connected back to the sparger.
11. The LDA is moved forward again to the intended measurement position and the setup is given several minutes to saturate the sparger with air and to establish a stable flow in the column (this is especially important when using lower end flow rates).
12. A test measurement of around 30 second is started to verify that there are no reflections and that there are no distinct peaks which are associated with particle measurements. If particle peaks are detected, the column needs to be recleaned and the entire process in repeated from step 1 once again.

In the following subsections, the different types of measurements are detailed. An overview is given in Table 4.

Table 4. Overview of the different three-phase flow measurements.

Particle Size	**Calibration Curves**	Variations in the Gas Flow Rate and Measurement Depth	Flotation Measurements
88 micron	*Water only,* *3/9 repeats per weight*	*Water only,* *No repeats*	*None*
1-2 micron	*Both Fluids,* *3/9 repeats per weight (water)* *3 repeats per weight (water-glycerol)*	*Water only,* *No repeats*	*Both Fluids with and without using an oil film,* *3 repeats for each*
< 100 nm	*Water only,* *3/9 repeats per weight*	*Water only,* *No repeats*	*None*

3.2.3.1 Calibration Curves

A major component of this study is to investigate the repeatability of measurements and to see if it is possible to directly measure the particle concentrations during flotation. As such, it is necessary to obtain calibration curves. Measurements for the calibration curves have been carried out exactly the same for each of the three particle sizes given in subsection 3.1.3: samples starting at 1 *mg* going up to 16 *mg* in steps of 3 *mg* are considered. Furthermore, to evaluate the repeatability of these measurements each calibration curve is repeated a total of 3 times, where each curve is measured on a different date. While performing additional repeated measurements is preferable, a compromise was made due to time constraints: only the 4 *mg* and 13 *mg* samples were repeated for an additional 6 times per particle size, resulting in 9 independent measurements for these weight and only 3 for all the other weights. These two

sample weights in particular were chosen to get a better idea of the spread between separate measurements for both low and high particle concentrations. For the measurements in water-glycerol, only the abovementioned 3 repeats of the calibration curve are performed with the 1-2 micron particles. Analogue to the measurements in water, the outer column is filled with just demineralized water.

Measurements times of 10 minutes were used where the first two minutes only the bubbles themselves are measured to get a background measurement prior to adding the particles, where typically, adding the particles takes around a minute in total. First measuring the bubbles allows for the data to be used with the mean filter and provides insights in the experimental conditions when compared to other data points.

The gas flow rate was fixed to 10 *sccm* for each and every calibration curve measurement in water and 5 *sccm* for the water-glycerol calibration curves. The minimal gas flow rate is desirable when using water-glycerol due to the observed much higher gas holdup when compared to water.

3.2.3.2 Variations in the Gas Flow Rate and Measurement Depth

To observe the effects of the gas flow rate and the measurement depth on the data rate and the subsequent particle concentration, measurements have been carried out over the partial diameter of the column using all three particle sizes for a varying gas flow rate. The variation in the gas flow rate is from 5 *sccm* up to 25 *sccm* in steps of 5 *sccm* and the distance between each measurement over the depth is around 2 *mm*, starting at the same measurement point as the one used for the calibration curves. Measurement were only carried out once for each particle size in demineralized water.

A slightly difference in the used methodology when compared to the calibration curves is that the particles are added prior to starting the measurements. This is due to sequential nature of performing measurements over the diameter in one go, where each measurement point is carried out for two minutes. A weight of around 7 *mg* was used per sample, as this was observed to generally be satisfactory for obtaining a sufficiently high data rate of around a few hundred velocity realization per second.

3.2.3.3 Flotation Measurements

Using similar methodology as for the calibration curves, several measurements have been performed to obtain particle number counts during flotation. These experiments have been conducted using the 1-2 micron sized particles only with a samples weight of 10 *mg*, as these have been observed to produce higher data rates at similar weights. A total of 12 measurements were carried out on the column, three repeats for each configuration with either water or water-glycerol and with or without an applied oil film to the top surface of the fluid.

Similarly, the bubble-only measurements prior to adding the particles are also performed for a duration of 5 minutes. The particles are added after these 5 minutes, after which the measurement continues for a total measurement time of 30 minutes. The application of the oil film was performed after adding the particle by pouring the oil over the fluid until the entire surface was covered by a homogenous layer of oil.

The measurement position is identical to the one used in the calibration curve measurements. Once again, the gas flow rate was fixed to 10 *sccm* for the water measurements and 5 *sccm* for the water-glycerol measurements.

3.2.4 Gas Holdup

Observations made during the water-glycerol measurements have shown a vast increase in the gas holdup compared to water under similar operating conditions and similar gas flow rates. To verify the increase in the gas holdup and to compare it to previous measurements performed by other students, the surface

height of the water-glycerol mixture is marked and the increase in surface height is measured for various gas flow rates. The gas holdup is then calculated using the diameter of the inner column and total volume of the fluid without bubbling.
A further use case for the gas holdup is to verify the exponential relation given in Equation 12. Given the decay in data rate during the measurements detailed in 3.2.3.2 and by using data on the mean bubble sizes obtained by Lakerveld, a comparison can be made.

3.2.5 Particle Size Measurements

Particle size measurement were performed using both Dynamic Light Scattering (DLS) and Transmission Electron Microscopy (TEM) to verify the sizes of the particles used in the experiments. Both of these measurement have been performed by a trained technician, E. van den Heuvel. The used samples were prepared identically to the samples used in the LDA experiments. Obtained data from the DLS measurements were analysed and exported from the ALV-5000/E software package.

As nano powders have often been known to be larger than what is reported, it is of particular interest to see whether the samples contain actual nanosized particles or not. If this is indeed the case, the capability of LDA to measure down to at least nano sized particles may be inferred. Something which is of great interest in molten salt experiments due to the reportedly wide range of solid fission product particle sizes in molten salt.

3.3 Data Processing

As mentioned in section 3.1, signals produced by the BSA processor are displayed and stored in the BSA Flow software. The software features a number of different data processing operations by defaults and allows for data export in various formats. For the contents of this study data was exported as raw data in the .csv format and subsequently further processed and analysed in Python.

Once imported to Python the data files are converted to NumPy data arrays and subsequently stored in a series of ordered folders. Basic filtering of data is then performed to clean up the results, namely, the removal of zero velocity measurements and the removal of outliers. The removal of the outliers is either done by only keeping data that is within a number of standard deviations of the mean or by applying a low bandpass velocity filter to the dataset. The filters used to minimize the effect of bubbles on the measurements results, as outlined in section 2.2, are then subsequently applied to the datasets already filtered by the aforementioned basic data filter. Furthermore, to obtain time dependent values for the particle number density during flotation, the data is processed using a data point count dependent moving average window where data is essentially divided into overlapping blocks.

3.3.1 Uncertainty Propagation

Aside from the systematic uncertainties mentioned in the previous subsections, such as: uncertainty in the position of the measurement volume, uncertainty in the mixing ratio, uncertainty in the sample weight and uncertainty in the gas flow, there are a number of additional systematic uncertainties, some of which are accounted for.

Since the experiments were performed during multiple weeks, a variation in temperature is expected. While the LDA measurements themselves are not affected, the change in temperature does change the properties of the fluid and subsequently also the flow field. In calculating the particle concentration as per Equations 13 and 15 , the velocity realizations of the particles are used to make the computation independent of the flow field. As such., for accurate measurements of the total velocity, the error due to changes in the temperature is expected to be minimal. In this study however, only a single component of the velocity is measured which could lead to a non-trivial error due to temperature fluctuations. An estimate of this error could potentially be made by repeating measurements in a temperature controlled

environment, however this has not been performed in this study. Other unaccounted uncertainties can also be attributed to settings used for the LDA, which may not be optimal, and the BSA processor.

A calibration certificate of the LDA is available and states a 0.7% uncertainty with a coverage factor of 2 in the calibration factor. On the manufacturers website another slightly larger number is given, namely, 0.11%. Given the extremely small uncertainties that were stated, an uncertainty of 0.11% is taken for the individual velocity realizations. To calculate the resulting error in the particle concentration (Equation 15), the partial derivative with respect to the velocity is taken and the errors resulting from each and every velocity realization are quadratically summed:

$$\sigma_c = \sqrt{\sum_i \left(\sigma_{U_i} \frac{\partial}{\partial U_i} \frac{1}{|U_i|}\right)^2} = \sqrt{\sum_i \left(\frac{0.0011/2}{U_i}\right)^2} \tag{28}$$

When performing computations for statistical averages such as the mean velocity, special consideration needs to be taken to account for the velocity bias in the particle sampling. This bias arises due to the higher rate of realizations of the faster particles in the flow field. In the LDA and PDA reference manual [20], an algorithm is given to account for this bias by using the transition times as weights. Furthermore, if the data is low and the realization can be deemed uncorrelated, then weighting is not needed. An example when computing the mean velocity is given as:

$$U_{mean} = \frac{\sum_i \tau_i U_i}{\sum_i \tau_i} \tag{29}$$

Where τ_i are the transition times, the time it takes for a particle to move through the detection volume, corresponding to the individual velocity realizations U_i.

Due to the asymmetric nature of the filter mentioned in section 3.3, it is non-trivial to compute a good estimate. Possibly, an estimate can be made by using artificial data under a few assumptions of the underlying distributions, in this study however, an estimate was made by comparing the resulting values for the particle number densities before and after filtering and by taking the uncertainty as half the difference in magnitude:

$$\sigma_f = \sqrt{\sum_i \left(\sigma_{f_i}\right)^2} = \sqrt{\sum_i \left(\frac{C_{before} - C_{after}}{2}\right)^2} \tag{30}$$

Where C_{before} denotes the particle concentration as computed without filtering and C_{after} denotes the particle concentration as computed after filtering.

The random uncertainty, or the spread between different measurements is calculated as the standard error σ_{random}. Finally, the combined uncertainty for the average particle concentration is calculated as the quadratic sum of the filter uncertainties, the random uncertainty and the calibration uncertainties:

$$\sigma_{total} = \sqrt{\sigma_c^2 + \sigma_f^2 + \sigma_{random}^2} \tag{31}$$

4. Results

Results obtained from the measurements described in section 3.2 are given in this chapter. Section 4.1 provides more context for subsequent measurement by displaying the results of the particle size measurements with DLS and TEM. An overview and summary of the findings from the two-phase flow setup is given section 4.2 Furthermore, findings regarding the added complexity of bubbles and behaviour of the filters mentioned in section 2.2 are given in section 4.3. Sections 4.4 and 4.5 contain the three-phase flow measurement under varying parameters, such as the sample weight, the gas flow rate, the particles used and the measurement depth. Finally, longer duration measurements of 30 minutes during flotation are displayed in section 4.6.

4.1 Particle Size Measurements

As mentioned in chapter 3, no accurate data is available on the size distribution of the used nano powder. In order to be able to better interpret the measurement results of the nano powder, but also the 88 micron and 1-2 micron powders, several particle size measurements were conducted using DLS and TEM. Results for the 1-2 micron powder and the nano powder are displayed in the following two subsections. A further interpretation of the results is given in chapter 5, the discussion.

During the measurements themselves it was observed that the selected methods and methodologies were not suitable for the 88 micron particles, as 88 micron falls outside the measurement range for DLS and no good examples were observed using TEM. The TEM results for the 88 micron particles is likely due to the used sample, which visibly had a comparatively low particle density. Furthermore, the grid that was used in TEM was in the same order of magnitude as the 88 micron particles themselves, which may not be ideal. The border of the grid is shown on the left side in Figure 20. Some examples of unidentifiable structures found in the 88 micron powder sample are given in appendix B for completion.

4.1.1 Sub 100 nm Particles

The DLS results obtained from the nano powder are shown in Figure 19 down below. The figure shows peaks for the scattered light at 100-200 *nm* and 500-1000 *nm*. This suggests that while there are nano-sized particles, there is a detectable content of micron-sized particles present in the sample. It is important to note that the DLS results in Figure 19 and Figure 23 display the scattered light intensity as function of the particle diameter, which is not identical to the actual size distribution. As the amount of light scattered is also a function of the particle diameter, an equal amount of light scattered from two differently sized particles indicates a much higher concentration of the lower diameter particle.

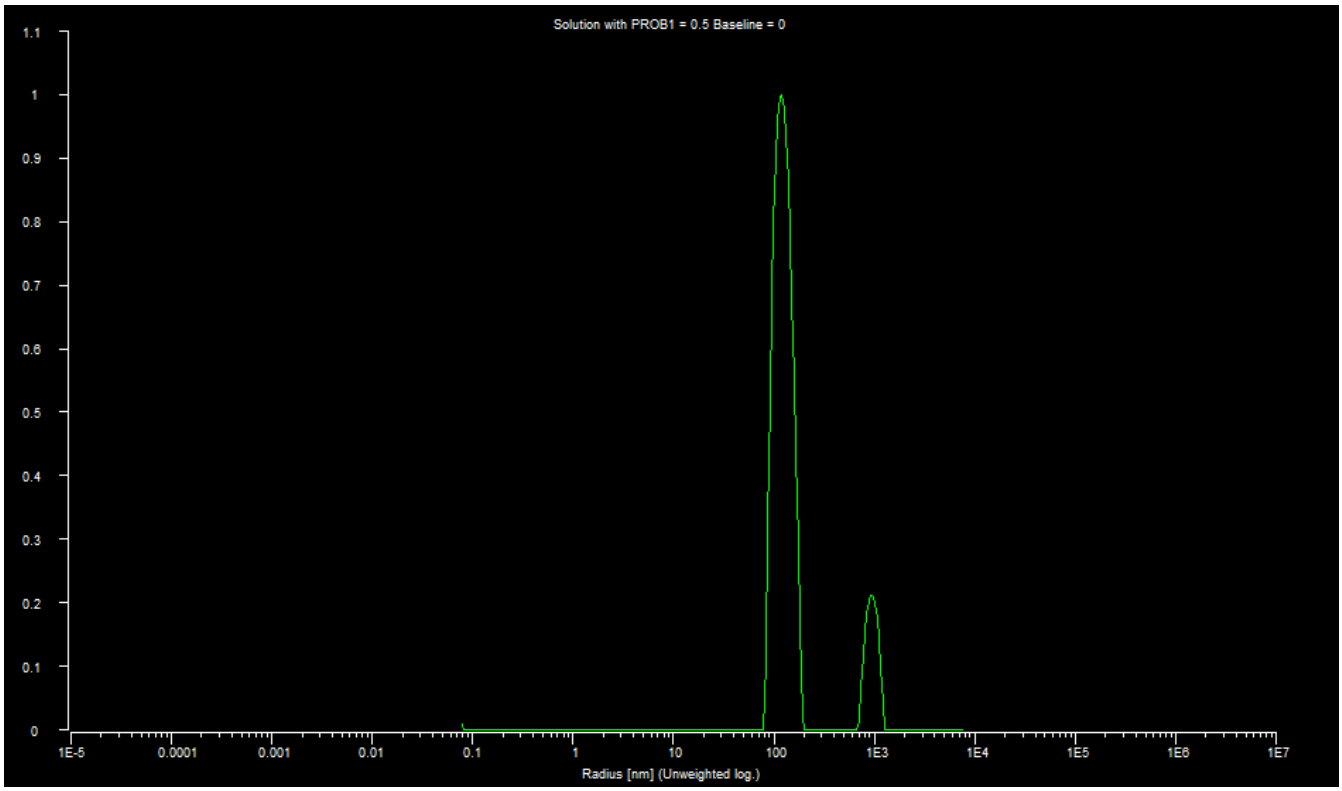

Figure 19. Scattered light intensity as function of the particle diameter for the sub 100 nm powder.

Similar to the results obtained with DLS in Figure 19, a similar conclusion can be drawn from the images obtained with TEM. In Figure 20 and Figure 21, a large number of particles can be observed that are around 100 *nm* in diameter, but some larger sized particles of around 1 micron in diameter are also observed (Figure 21). Furthermore, looking at Figure 21 and Figure 22, the particles appear to be remarkably spherical in shape. Given the presence of micron-sized particles, it is unclear whether the particles in the 100 nm range are also measured in the results obtained in subsections 4.2-4.5.

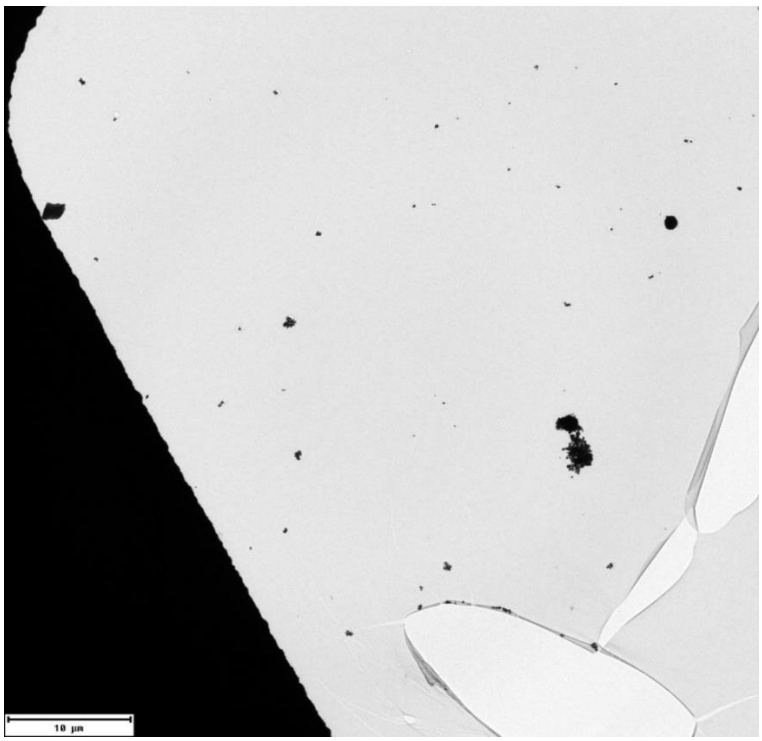

Figure 20. Overview of multiple clusters in the sub 100 nm powder under TEM with a size scale of 10 micron.

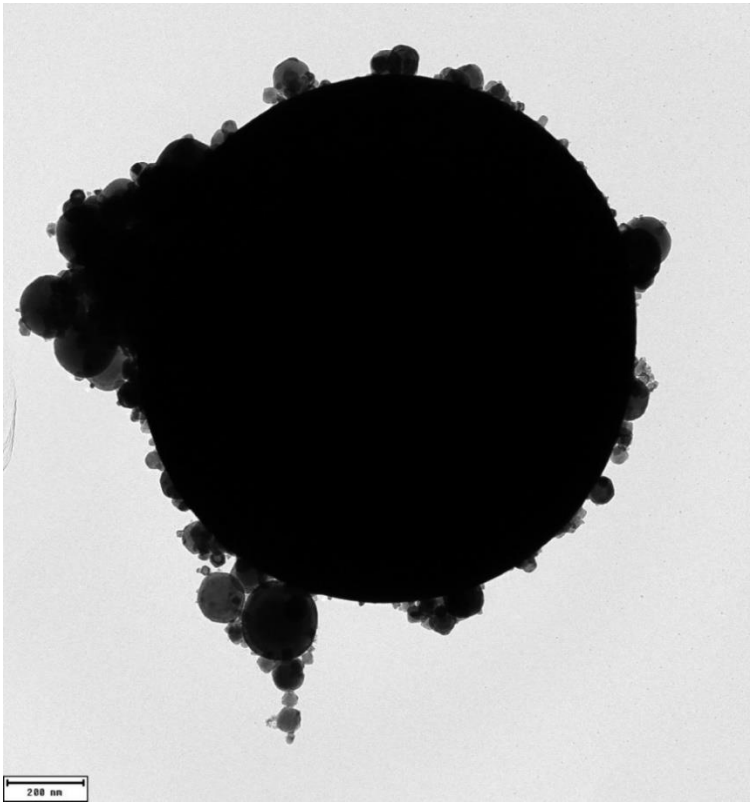

Figure 21. Example of a cluster in the sub 100 nm powder under TEM with a size scale of 200 nm.

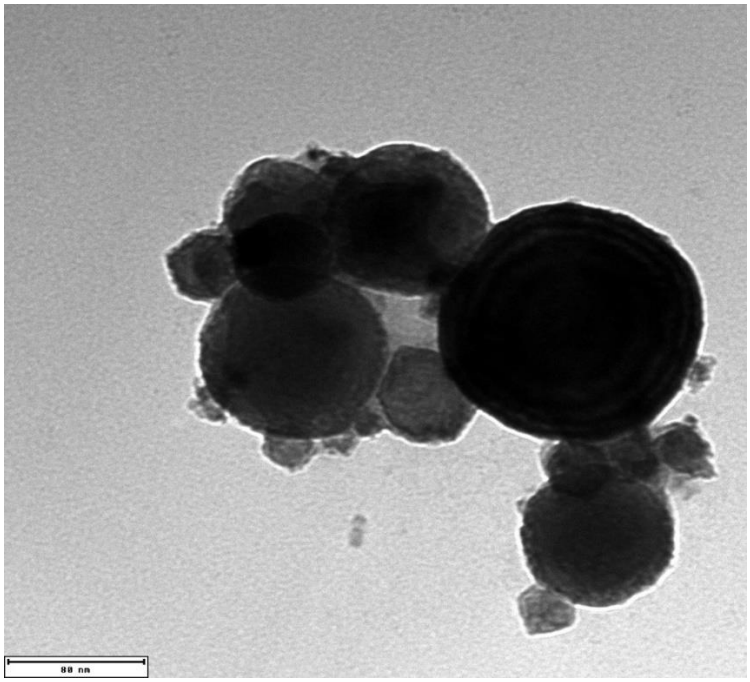

Figure 22. Second example of a cluster in the sub 100 nm powder under TEM with a size scale of 80 nm.

4.1.2 1-2 Micron Particles

Interestingly, the scattered light intensity plot for the 1-2 micron powder in Figure 23 also shows peaks around the same size ranges when compared to the nano powder. Comparatively, when looking at both Figure 19 and Figure 23 it can be observed that while the size ranges are quite similar, the ratio between micron-sized and nano-sized particles is different. The peak for the micron-sized particles in Figure 23 is

much higher in magnitude and wider relative to the one in Figure 19, which suggests a significantly larger content of micron-sized particles compared to the nano powder.

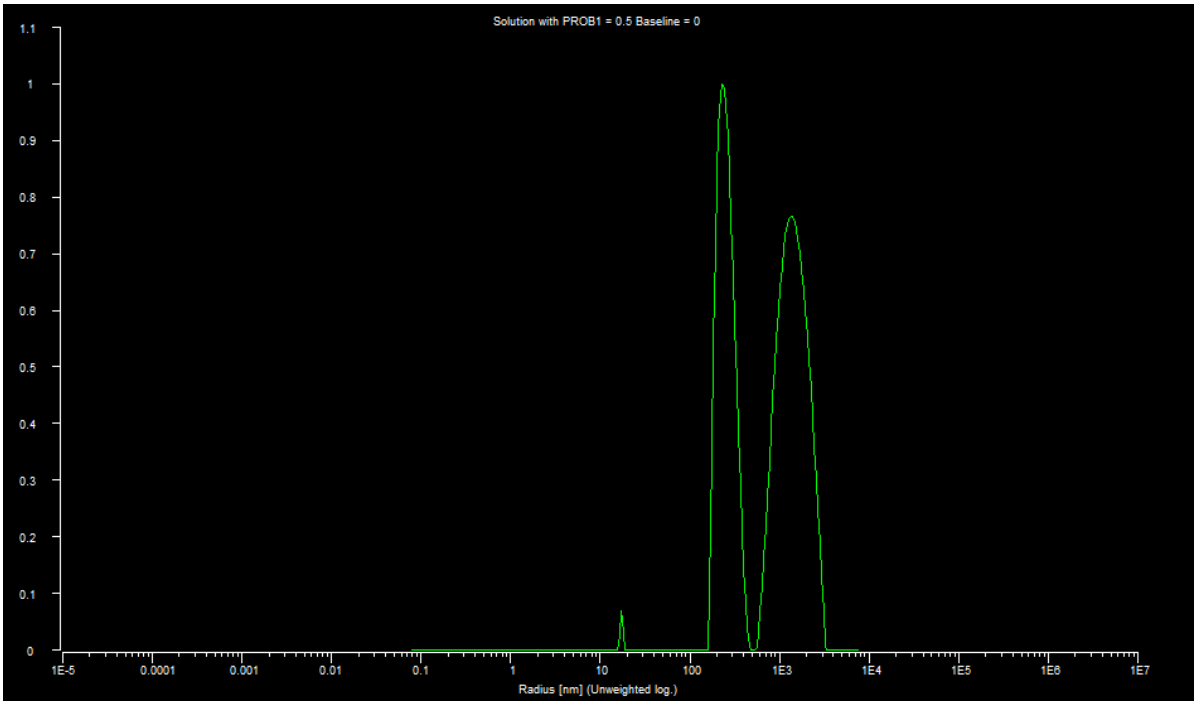

Figure 23. Scattered light intensity as function of the particle diameter for the 1-2 micron powder.

TEM images obtained with the 1-2 micron powder further supports the findings in Figure 23. In Figure 24, a particle was observed with total length of slightly more than 1 micron, while in Figure 25 another particle was found with a length of around 200 *nm*. The shape of these particles is notably different compared to the nano powder particles, which were much more spherical. Theoretically, particles with a size range of 1-2 micron should be relatively better detectable with the used LDA setup and wavelength of light As such, expected is that the 1-2 micron powder should produce the highest signal when compared to the other powders.

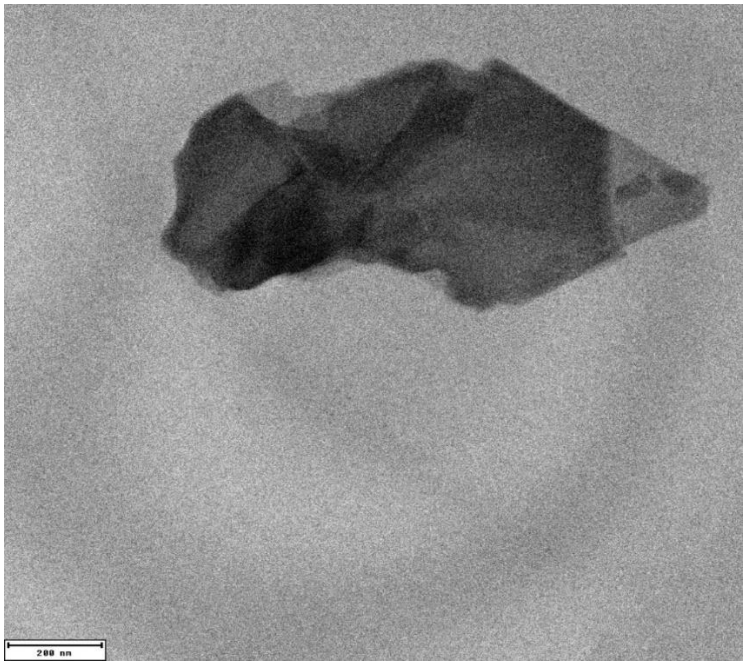

Figure 24. Example of a particle in the 1-2 micron powder under TEM with a size scale of 200 nm.

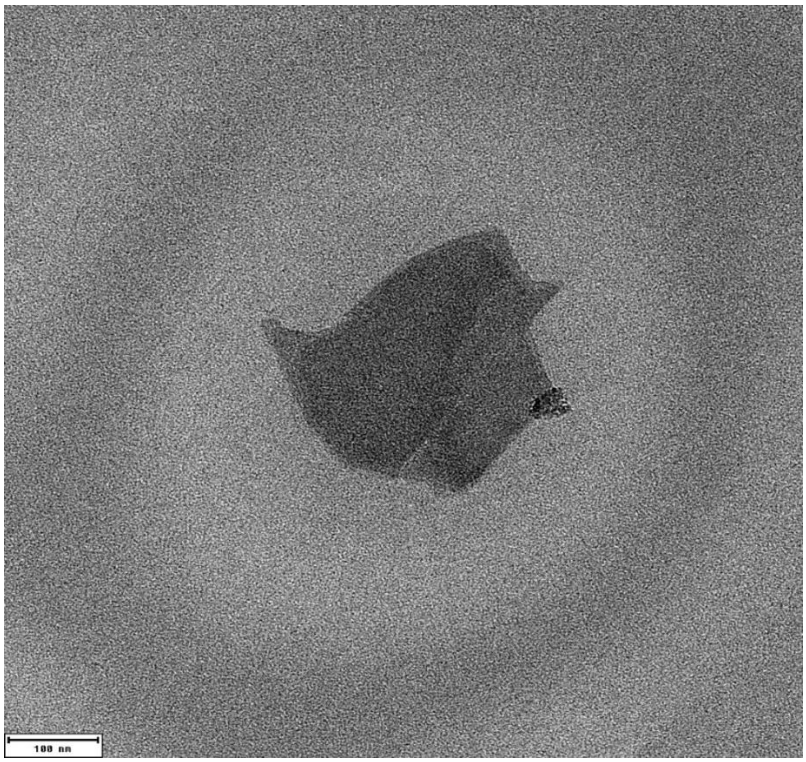

Figure 25. Second example of a particle in the 1-2 micron powder under TEM with a size scale of 100 nm.

4.2 Stirred Two-Phase Flow Setup Summary

As a stepping stone in studying LDA measurements in three-phase flows, it is instrumental to first study the behaviour of LDA measurements while varying several parameters for a simplified case where only solid particles in a liquid is considered (i.e. no gaseous phase is included). In this subsection, a more detailed report is given of the most prominent results from the two-phase flows measurement to aid in the interpretation of the three-phase flow measurement in subsections 4.3-4.6. Variations of the following parameters were include: powder type (glass beads and molybdenum particles over varying sizes), flow speed, measurement depth and the total sample weight of the used powder.

Initial measurements were performed in a stirred graduated cylinder filled with demineralized water (see 3.1.1). Due to the vortex resulting from the mixer, measurements were only performed over the radius of the cylinder. The obtained profiles show a very general shape for the normalized density distribution, typically this includes a quickly rising peak with an exponential tail. An example is given in Figure 26, where the wall distance is defined as the distance from the glass sidewall of the cylinder and the normalized density is the density as computed from Equation 15, but normalized over the various measurement depths on the x-axis.

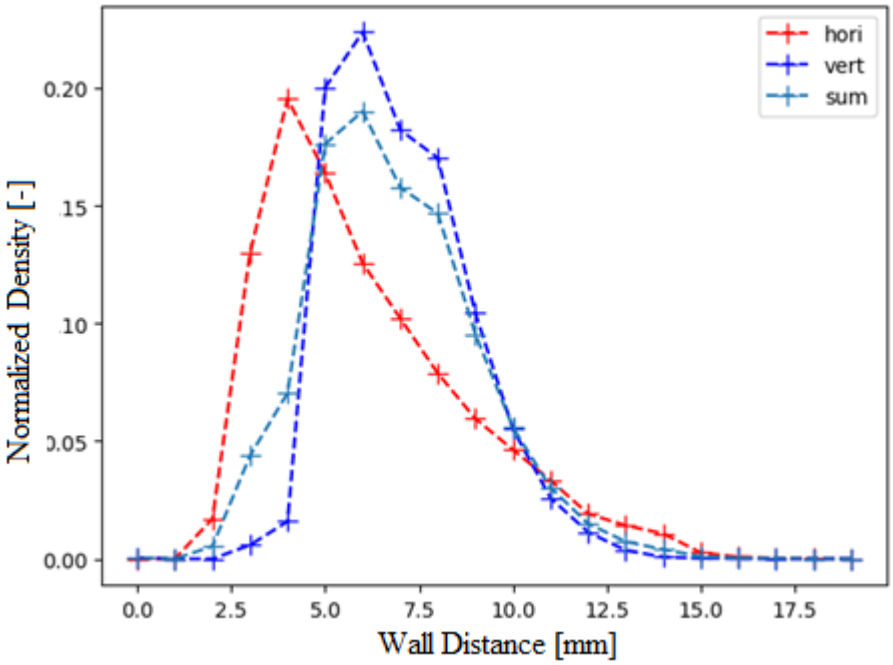

Figure 26. Example of a typical particle density plot obtained during two-phase flow using both laser pairs.

During the experiments it became apparent that reflections caused by the cylinder severely complicated certain practical aspects. Initially, it was suggested by D. de Haas to calibrate the measurement depth by focusing the beams on the glass surface, however due to inconsistencies in the data rate resulting from these reflections, this was deemed too imprecise. Moreover, observation of the data also showed that certain measurement depths are highly more sensitive to the occurrence of reflections. Partially due to this finding, subsequent measurements for three-phase flows were limited to a single point somewhat close, but not too close to the glass surface (estimated to be around 5 *mm*).

As a proof of concept for the measurement principles given in section 2.2, several series of measurements were performed whereby the velocity of the particles is changed via the dial on the magnetic mixer. Expected is that if the addition of the particle velocities as weight factors truly makes the density measurements independent of the flow field then similar results should be obtained. Especially for tracer particles, which are expected to follow the streamlines of the flow closely. To ensure consistency between measurements, the measurement were done in series whereby only the dial was changes in between measurements. These results are shown in Figure 27.

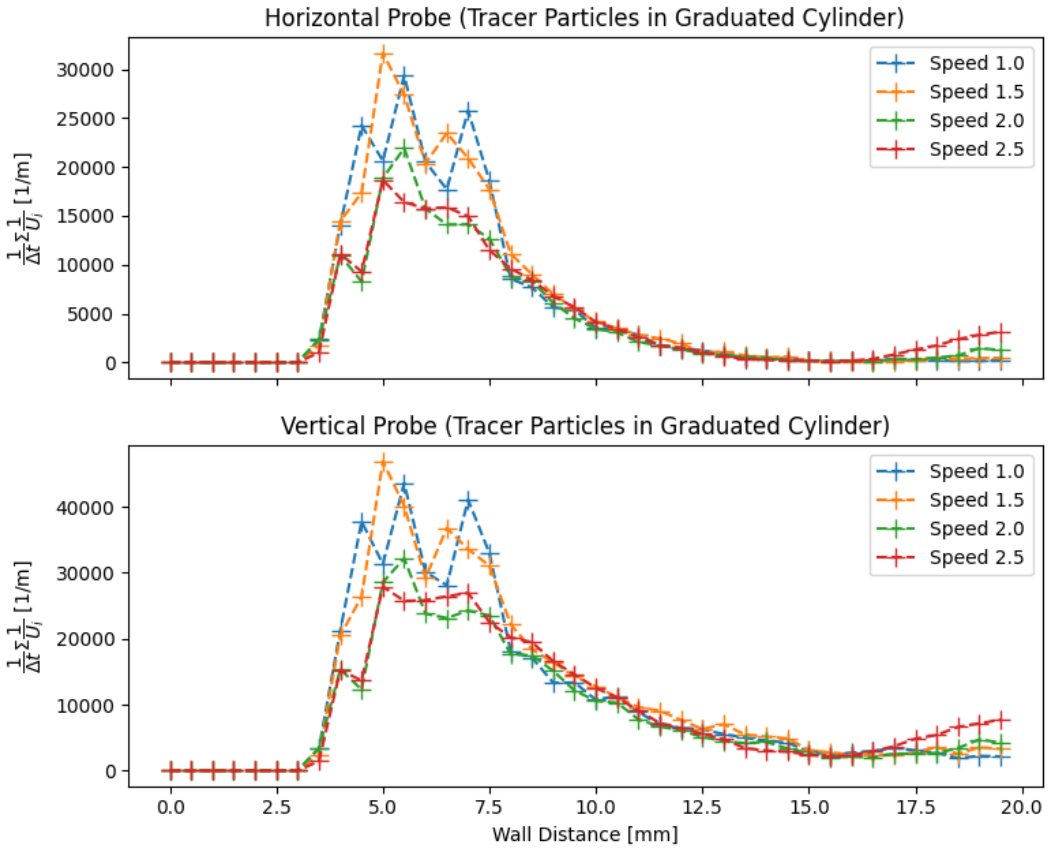

Figure 27. Particle density plots made with tracer particles for different fluid flow speeds. The cylinder was filled up to 300 ml and measurements were taken halfway between the liquid surface height and the bottom.

The above results in Figure 27 show a reasonable agreement between the different dial settings, especially from around 8 mm and further. Furthermore, the same profile is obtained as with the initial test experiments and the figure shows great consistency in both the horizontal and vertical laser pairs (top and bottom graphs), only the magnitudes differ. Nonetheless, some differences are observed between 4 and 8 *mm*. Given that the flow field is generated by a mixer, suspected is that not only the velocity of the flow field changes but also the shape of the flow field, which could partially explain the difference in the results (e.g. at increasingly higher settings an increasingly larger vortex develops in the middle of cylinder). It was assumed that the tracer particles are homogenously spread over the entire volume, which gave the expectation of a more evenly spread distribution. It is possible that this assumption was simply not quite correct as both graphs in Figure 27 show an increase in concentration between 4 and 8 *mm*. Possibly, this peak, which can also be observed in Figure 26, is the result of the steady circular motion of the flow field as induced by the mixer. Where the mixing conditions are not ideal and where the circular pattern could result in a centrifuge-like effect on the particles which would force them outwards closer to the glass surface of the cylinder.

To study the measurement of particle concentrations as function of the sample weight, an experiment was conducted whereby samples of different weights were measured under similar experimental conditions. Measurements were conducted on 1-2 micron-sized particles at various measurement depths with a dial speed setting of 2. The subsequent results are averaged over the various positions to obtain an average density per weight. These results are shown in Figure 28. Unfortunately, all results below 5 *mm* had to be rejected due to the aforementioned reflections in the data set. The obtained relation between the sample weight and the resulting signal shows a clear positive correlation and possibly suggests a linear or

exponential shape. As the actual the number of particles increases linearly with the amount of powder, the correlation in Figure 28 was also expected to be linear.

Finally, multiple measurements were performed on three different nano powders, which all returned very similar results. This suggested that nano-sized particles may be measurable.

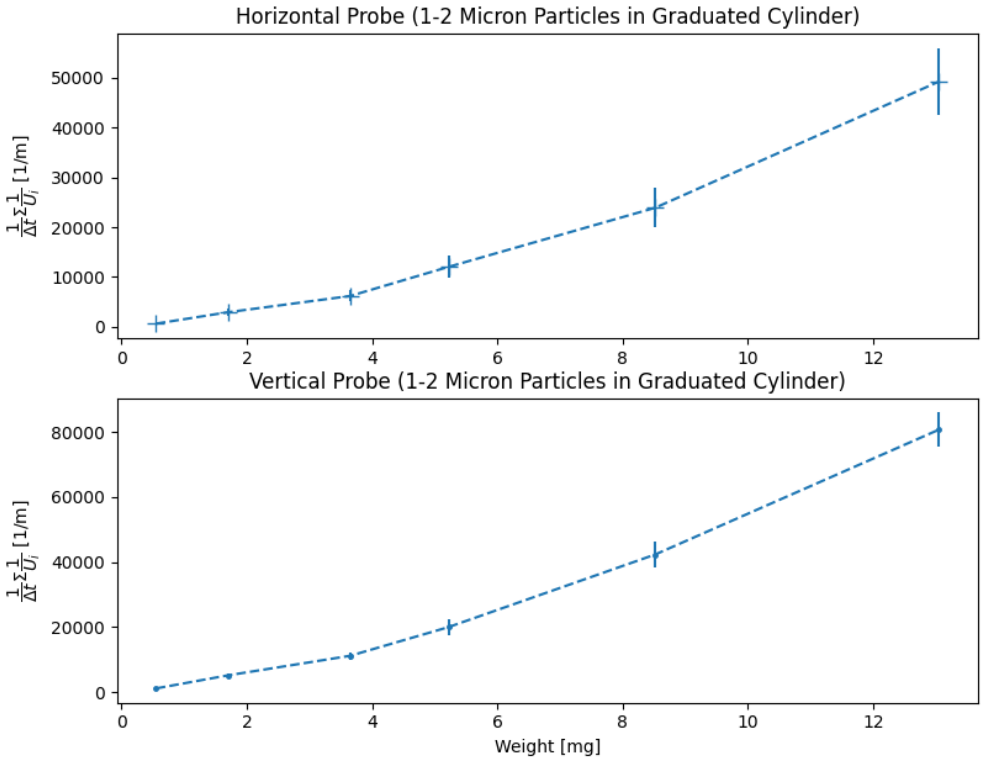

Figure 28. Position averaged particle density plot of 1-2 micron powder in two-phase flow.

4.3 Signal and Filter Characteristics for Three-Phase Flows

To get a better understanding of the additional complexity introduced by the added gas phase in the flotation column, several aspects are investigated regarding the typical velocity realizations and the subsequent velocity distributions. When looking at the individual realizations over time, results similar to the ones produced by Harteveld [24] and Mudde et al. [25] can be observed. Specifically, similar time gaps in the data that are ascribed to the passing of bubbles can be observed in Figure 29. Typically, these gap are also accompanied by the corresponding velocity gradients as mentioned in section 2.2. However, this is not always the case.

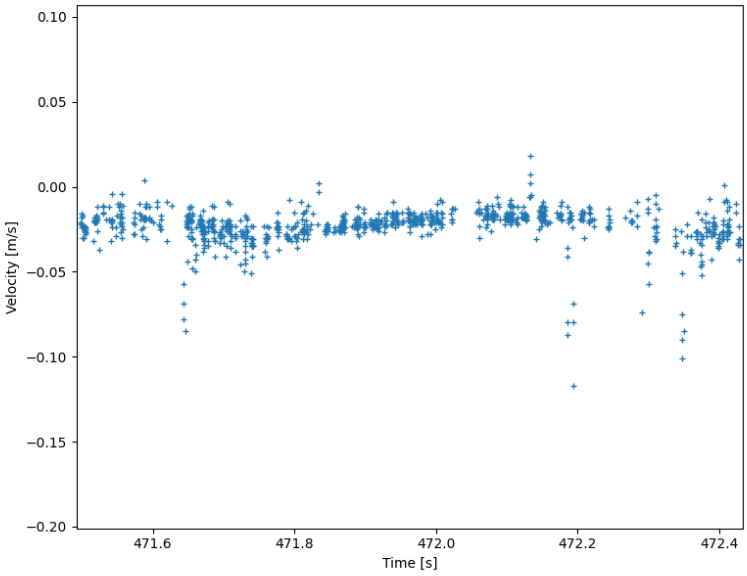

Figure 29. Showcase of gaps in the data due to passing bubbles.

Looking at velocity histograms in water before and after adding the particles reveals some interesting findings regarding the expected velocity profiles from the particles themselves and regarding the effectiveness of GMM under varying conditions (Figure 30). Generally, when performing measurements of 1-2 micron or 88 micron particles in water with a gas flow rate of 10 *sccm*, a resulting particle peak is obtained that is multiple orders of magnitude above the measurements without added particles. The observed peak, as show in Figure 30, can be seen to be approximately Gaussian with a relative small spread. Moreover, the background noise produced by the bubbles alone is also shown to be approximately Gaussian in shape under these experimental conditions.

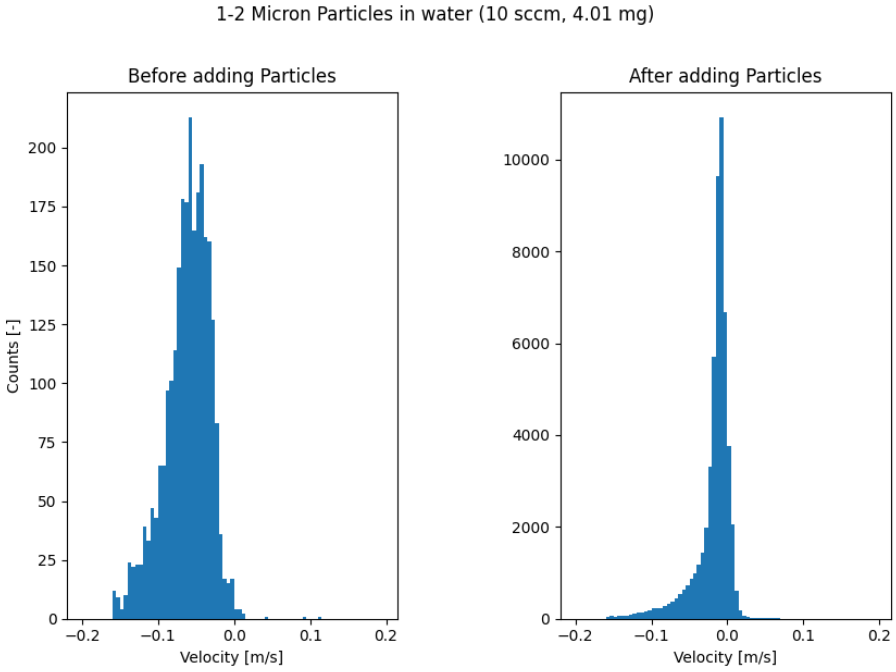

Figure 30. Histograms of velocity realizations before and after adding1-2 micron powder particles in water.

While the particle peak is distinct for larger particles, even under low sample weights, a different result is observed for the measurements with the nano-sized particles and the measurements of 1-2 micron-sized particles in aqueous glycerol. Firstly, when looking at typical results for aqueous glycerol, it can readily be observed that larger sample weights still produce a distinct particle peak. However, due to the combination of more overlap and a significant increase in the number of realization obtained from the bubbles due to an observed higher gas fraction (Figure 32), issues arise when lower sample weights are used. An example is given in Figure 33.

To quantify the increased gas holdup in aqueous glycerol, a measurement was conducted of the gas holdup as function of the gas flow rate. The obtained results shown in Figure 31 display an approximately linear response to the gas flow rate, as described by literature [39] (Equation 27). Furthermore, when compared to the results produced by Lakerveld [17] with the same setup, Lakerveld also found a similar linear relation. Some difference in the magnitude is observed, this could quite likely be due to the difference in the glycerol content of the mixture. Looking at the demineralized water results from Lakerveld suggest that that gas holdup should be comparative between the two fluid for the used gas flow rates, which is unlike what is observed during the experiments (Figure 32).

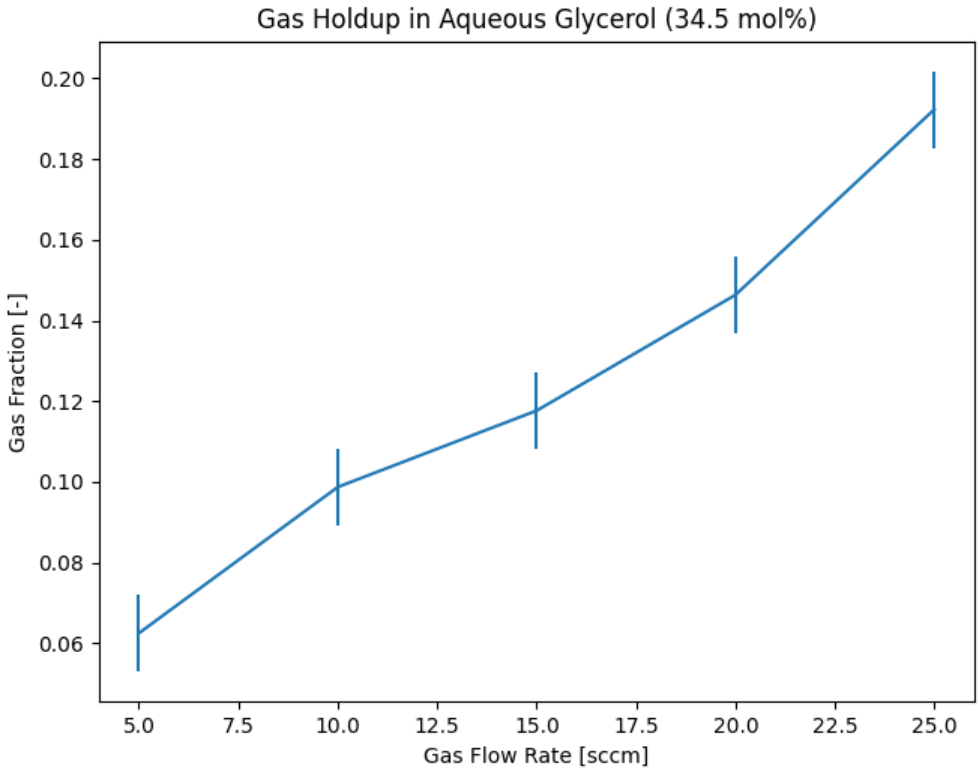

Figure 31. Measured gas holdup in aqueous glycerol with a gas flow of 5 sccm.

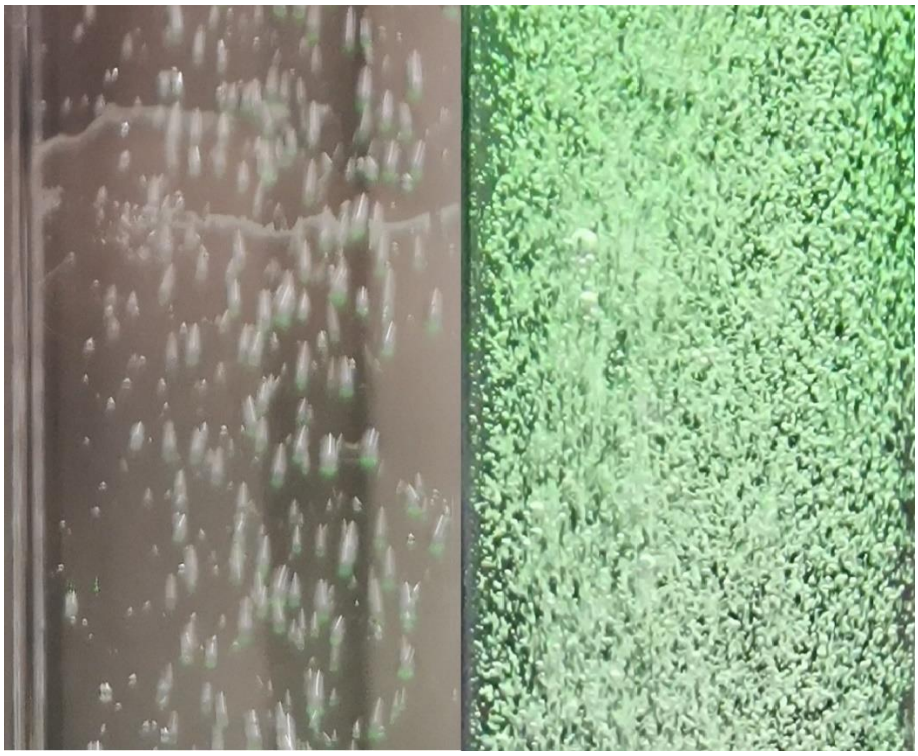

Figure 32. Visual comparison of the gas holdup in water with a gas flow rate of 10 sccm (left) and aqueous glycerol with a gas flow rate of 5 sccm (right).

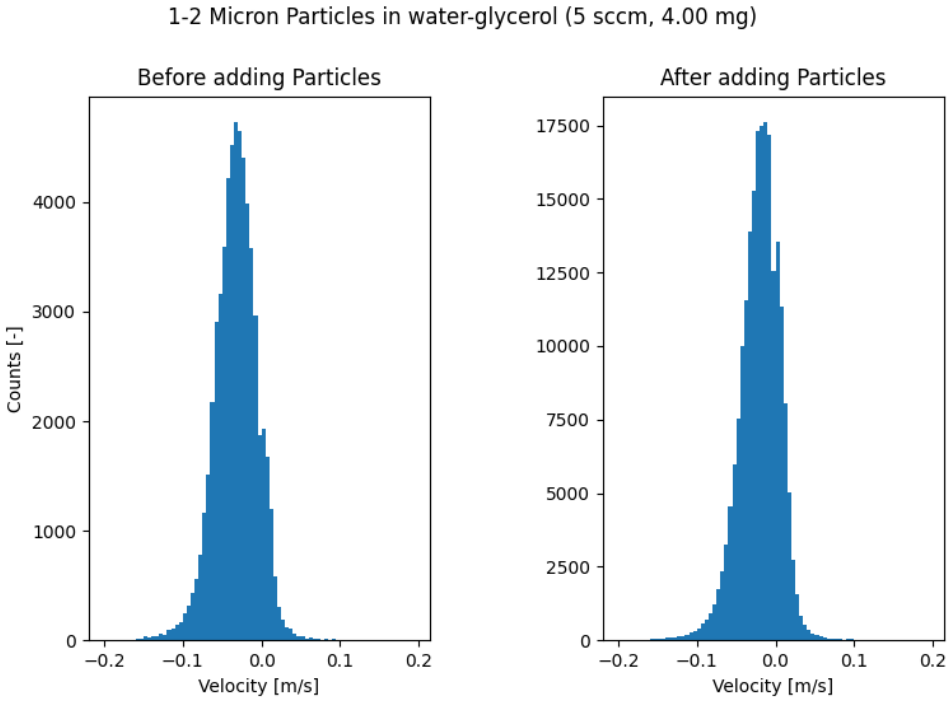

Figure 33. Histograms of velocity realizations before and after adding 1-2 micron powder particles in aqueous glycerol.

In the Figure 33, a sample weight of 4.00 *mg* is used in an aqueous glycerol measurement with a minimal gas flow rate of 5 *sccm*. The observed peak for just the bubble realization can be observed to be an entire order of magnitude above the one observed in water. After adding the particles a very faint peak can be

observed on the right side of the distribution, this could however, also be due to the random nature of the sampling. The vast majority of the particle velocity realizations are completely overlapped by the results obtained from the bubble peak. Consequently, the application of GMM in this instance fails as it becomes impossible to estimate the relative magnitudes of both distributions.

Another mode of failure for GMM occurs with low sample weight nano-sized measurements where fairly low counts are observed for both peaks. An example is given in Figure 34 with the resulting GMM output in Figure 35. By default, GMM assumes certain weights to the distributions, however, when the counts are low in both peaks the algorithm struggles to correctly estimate the relative small deviation of the particle peak. Subsequently, a curve similar in size is generated with two fairly identical distributions, unlike what is actually observed. Improvements were observed for similar cases when the measurement time was increased. Another way that has been observed to decreases the rate of failure is when the filtering of the maximum and the minimum velocities is tightened.

The gap filter is the second filter that influences the velocity distribution due to its application to velocity realizations close to gaps in the signal. Practically, the gap size and the removal band size are determined based on the observed signal, for the contents of this study values of respectively 5 *ms* and 1.75 *ms* are used. When applied to the measurements in this study, an insignificant change in the distribution is observed. The removal of realizations appears to be fairly spread.

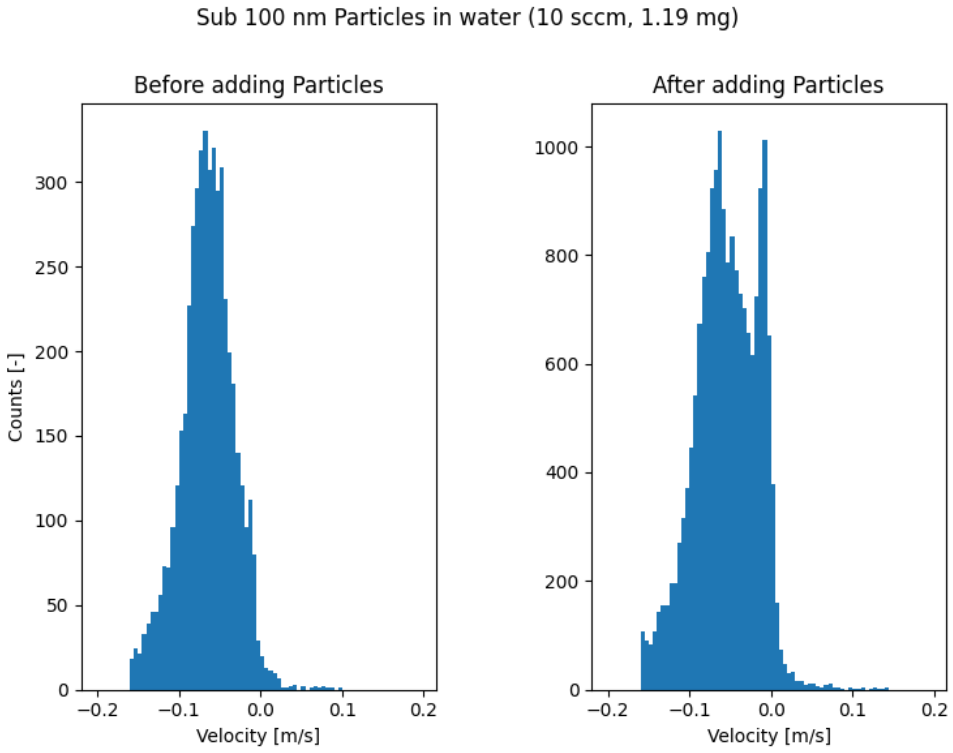

Figure 34. Histograms of velocity realizations before and after adding nano powder particles in water.

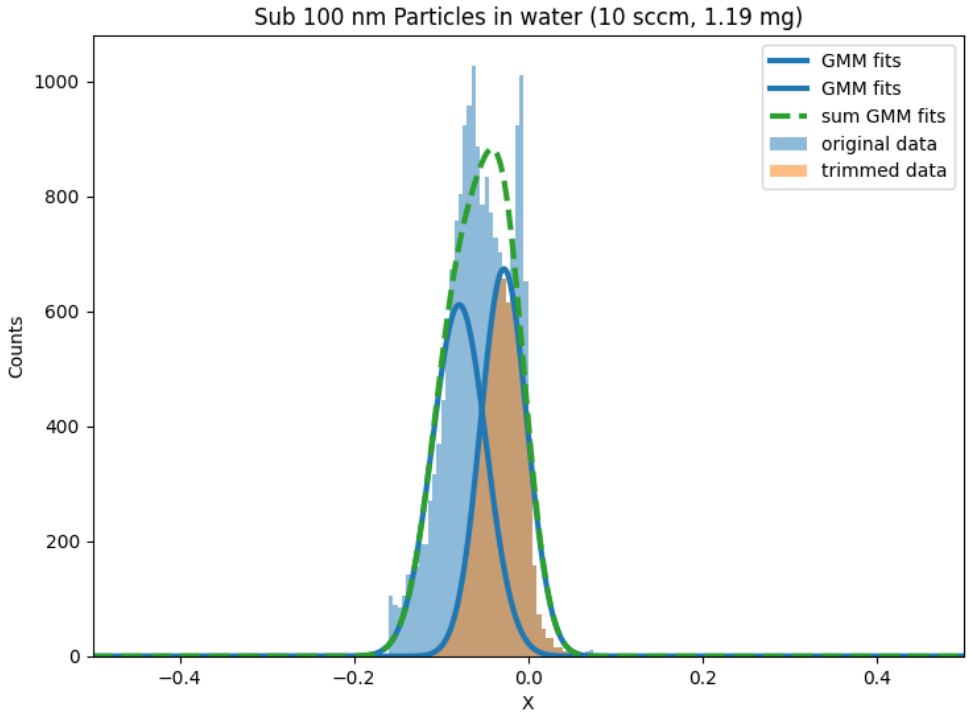

Figure 35. Showcase of GMM failing when using low weight samples with nano powder.

To summarize the findings in subsections 4.2 and 4.3 before displaying the three-phase flow results in subsections 4.4-4.6:

- Inverse velocity weighting as per Equation 15 has shown a reasonable result in eliminating the flow field dependency of particle concentration measurements in two-phase flows (Figure 27).
- The correlation between the sample weight and the corresponding measured particle concentration is expected to be linear (Figure 28).
- Particles in the size range of 100 *nm* may be detectable by LDA, but the results are not conclusive.
- Analogue to literature, the addition of a gaseous phase results in time gaps in the velocity realization due to optical blocking of the laser beams or the measurement volume.
- The gas holdup is observed to be much higher in aqueous glycerol compared to demineralized water and was shown to have a linear correlation with the gas flow rate, similar to what was expected from literature.
- The GMM filter was shown to produce good results when peaks resulting from the bubbles and the particles are distinct. Its application was shown to be limited when there is a significant overlap in the velocity distributions, this is the case for measurements in aqueous glycerol or when low sample weights are used with the nano powder.

4.4 Calibration Curves Measurements

Central to the contents of this study is the measurement of the local particle concentrations. The resulting signal produced by the sum of the inverse velocity realizations (Equation 15) needs to be properly scaled by the particle diameter and the effective probe volume cross section A_i to produce an absolute concentration. The scaling factor is obtained by performing measurements with different sample weights which can is used to construct a calibration curve. The curve can then be used to relate the signal back to a particle concentration.

To this extent, samples of varying weights are measured under similar experimental conditions and compared. The measurements in demineralised water have been carried out with a gas flow rate of 10

sccm for three different particle sizes and are post-processed using the filters mentioned in section 2.2. Measurements were conducted halfway up the column with an estimated measurement depth of 5 *mm* from the inner column wall. Graphs of the resulting values are displayed in subsections 4.4.1-4.4.3. Similar measurements were conducted using the 1-2 micron-sized particles in aqueous glycerol with a gas flow rate of 5 *sccm* to simulate the fluid dynamics of molten salt. Results are given in subsection 4.4.4. Given Equations 13 and 15, the used quantity on the y-axes is the inverse sum of the particle velocities divided by the total measurement time. This also allows for comparing the signal magnitudes between the different powders.

4.4.1 88 Micron Particles in Water

Looking at Figure 36 through Figure 39 reveals a fairly tight spread in measurements results throughout, the greatest variance between measurements is observed at 13 and 16 *mg*. In general, results appear to be fairly similar to the ones found for two-phase flows in figure Figure 28, where the correlation between the measured signal and the sample weight appears to be approximately linear in shape, especially for a sample weight higher than 7 *mg*.

Unsurprisingly, due to the relative high response to the 88 micron-sized particles when compared to the relative low response of the bubbles in demineralised water, the results obtained for the different filters, as listed in subsections 2.2.1-2.2.3 are almost identical. Analogue to comments made by Harteveld, the gap filter does remove a much larger number of datapoints which results into a comparatively larger error and a lower magnitude in the signal.

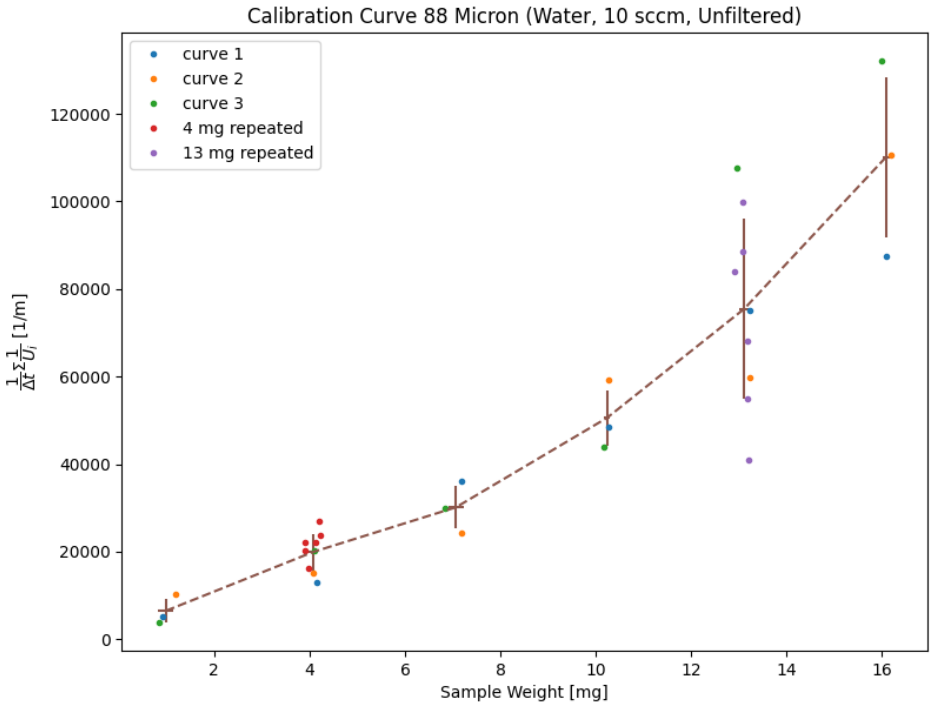

Figure 36. Calibration curve of the 88 micron -sized particles in water without filtering.

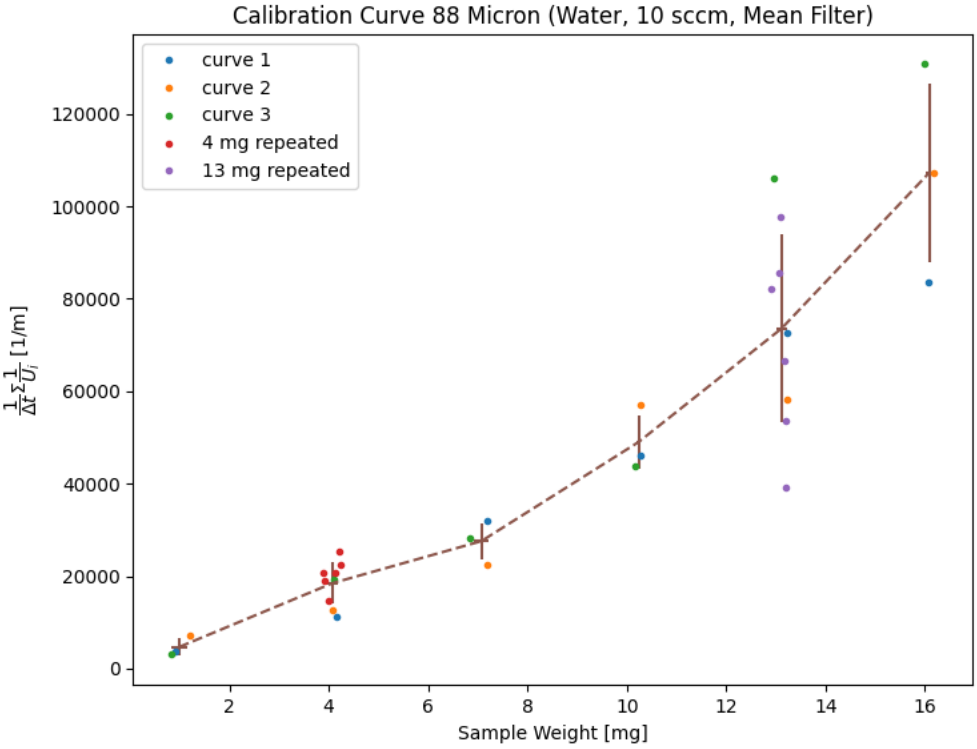

Figure 37. Calibration curve of the 88 micron -sized particles in water using the mean filter.

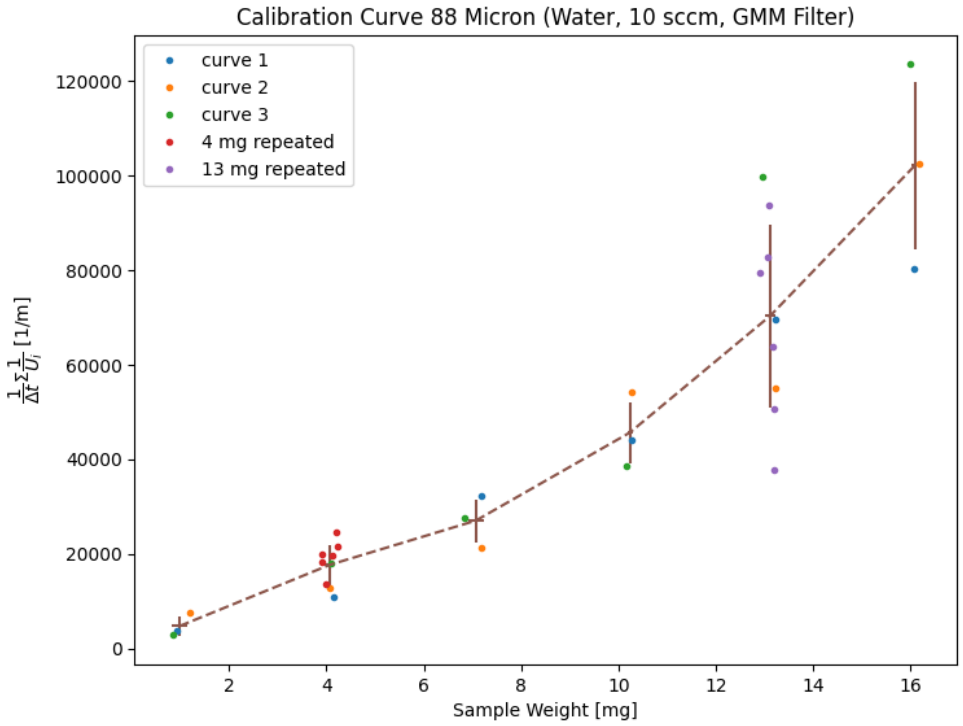

Figure 38. Calibration curve of the 88 micron -sized particles in water using the GMM filter.

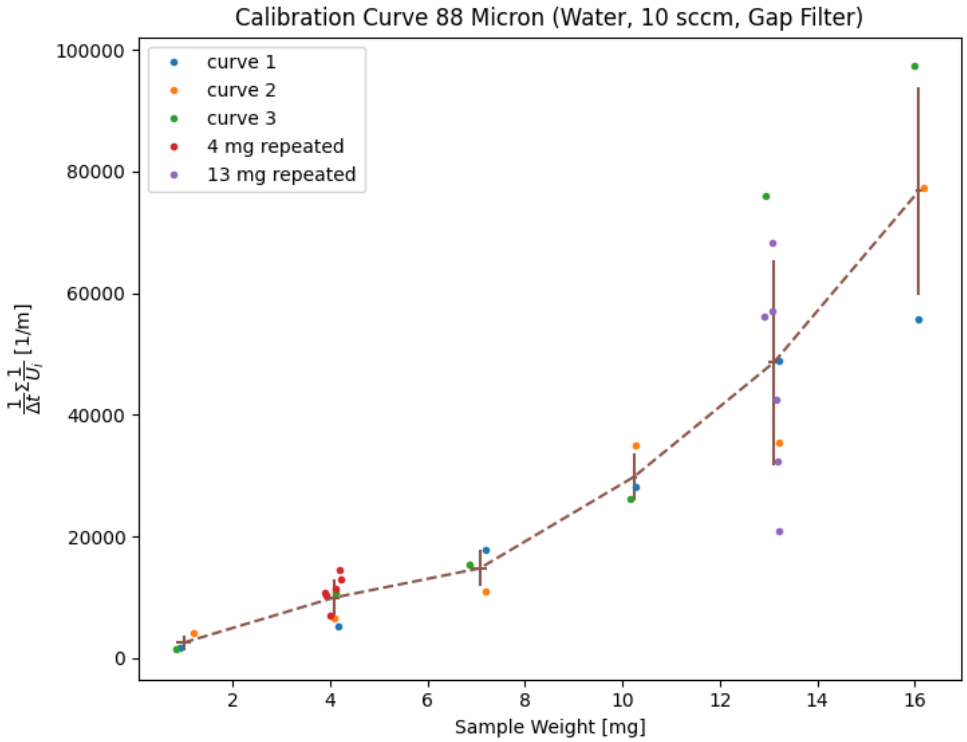

Figure 39. Calibration curve of the 88 micron -sized particles in water using the gap filter.

4.4.2 Sub 100 nm Particles in Water

Results for the nano-sized particles in Figure 40 through Figure 43 are similar to the ones obtained for the 88 micron particles, although some differences can be observed. The variance in the 7 and 10 *mg* measurements appears to be slightly larger while the spread in the 13 *mg* measurements is significantly less. Additionally, an outlier is measured in the curve 1 measurement set. The overall magnitude of the observed signal is generally more than a factor two lower. Compared to the other filters, the gap filter slightly reduces the spread in the 7 and 10 *mg* measurement sets. The correlation is observed to be noticeably less linear below 10 *mg*.

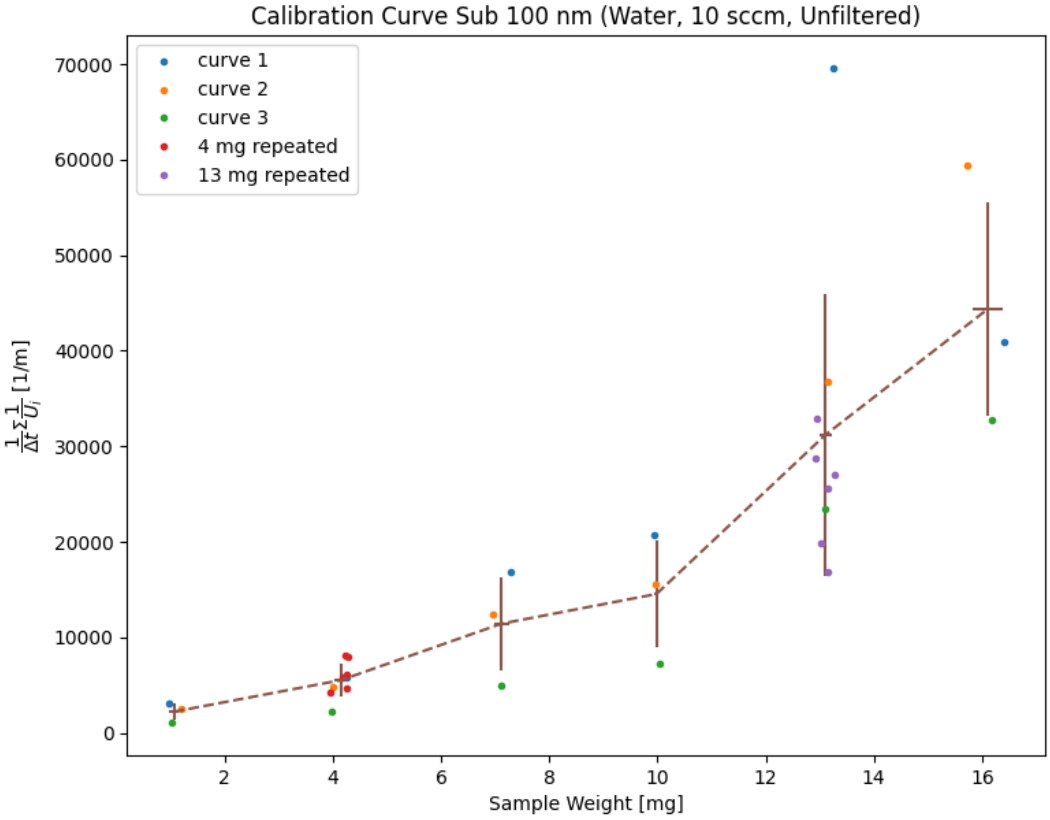

Figure 40. Calibration curve of the nano-sized particles in water without filtering.

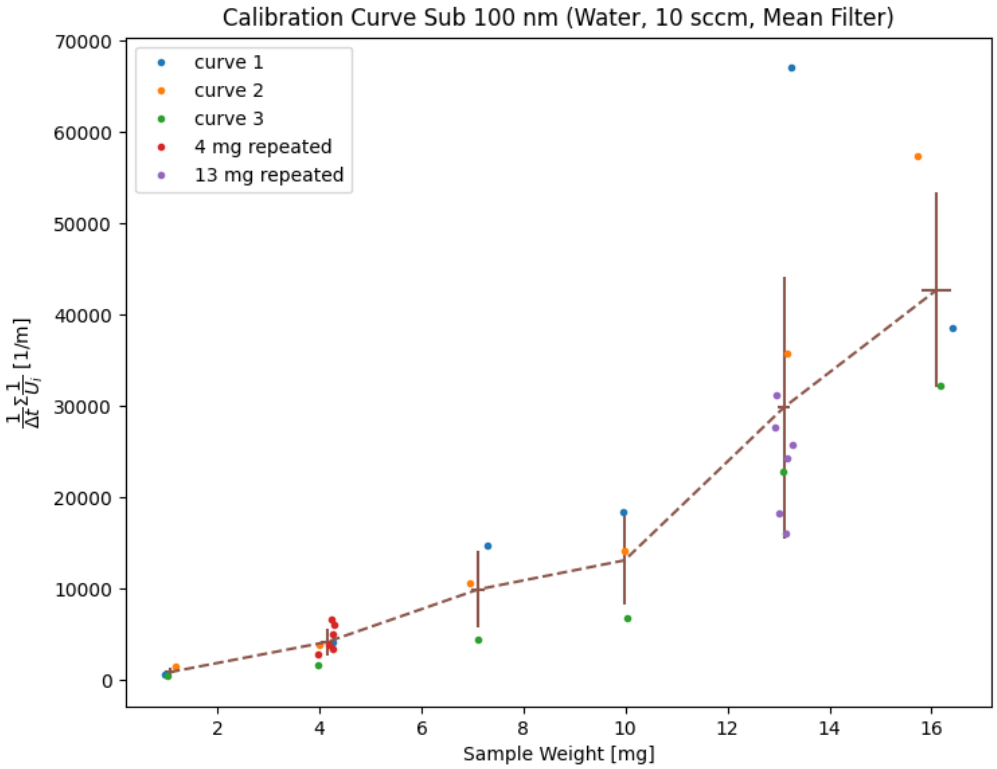

Figure 41. Calibration curve of the nano-sized particles in water using the mean filter.

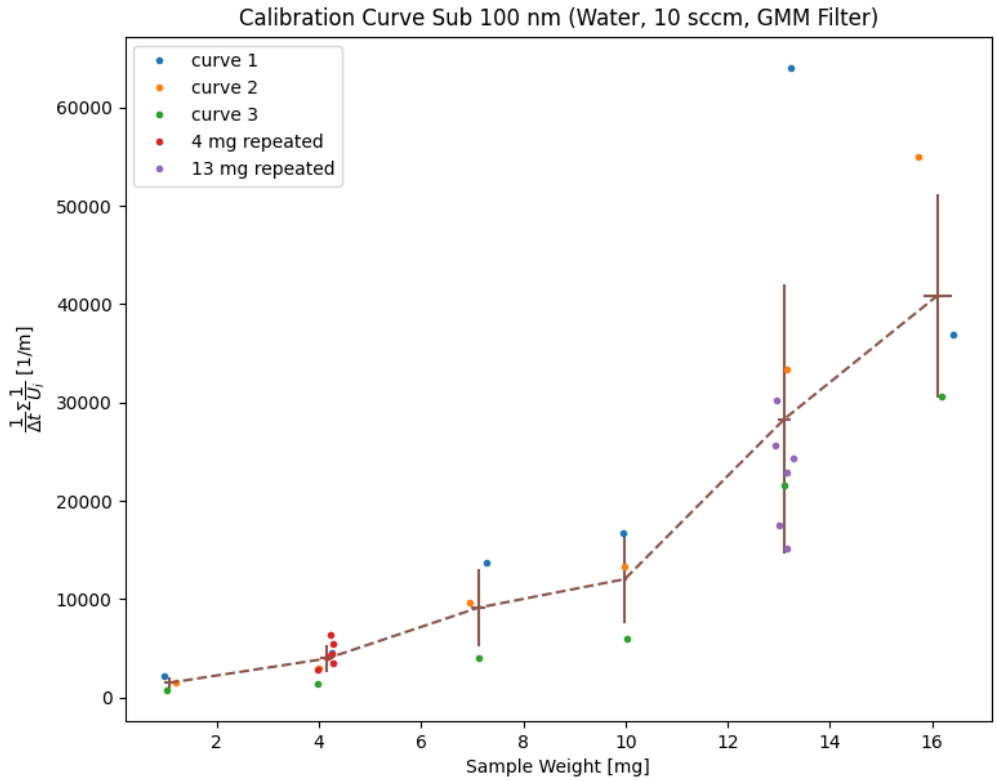

Figure 42. Calibration curve of the nano-sized particles in water using the GMM filter.

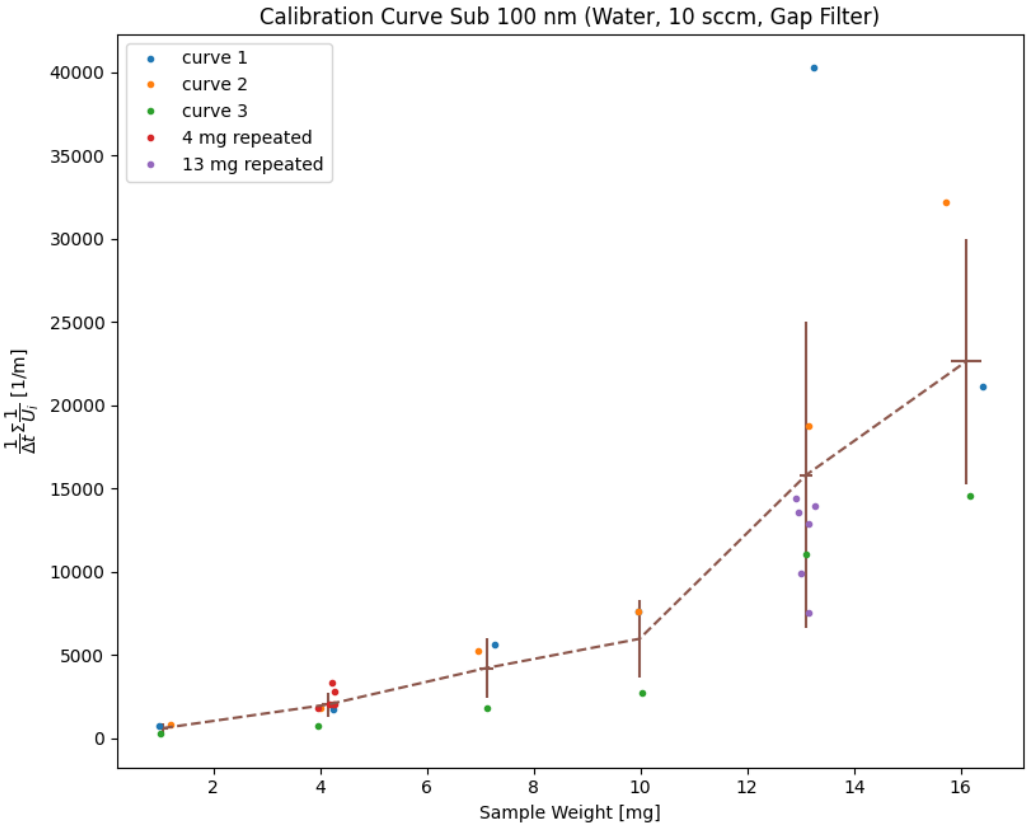

Figure 43. Calibration curve of the nano-sized particles in water using the gap filter.

4.4.3 1-2 Micron Particles in Water

The magnitude of the signal obtained using 1-2 micron particles is found to be higher than the magnitude for the other particles, i.e. the 88 micron -sized particles (Figure 36) and the sub-100 nm particles (Figure 40). The ratio between the particle-to-bubble signal ratio is higher as well, meaning that the influence of the filters is negligible. The spread of magnitudes, however, remains roughly the same, meaning that, apparently, the particle size has no significant influence on the statistical uncertainty.

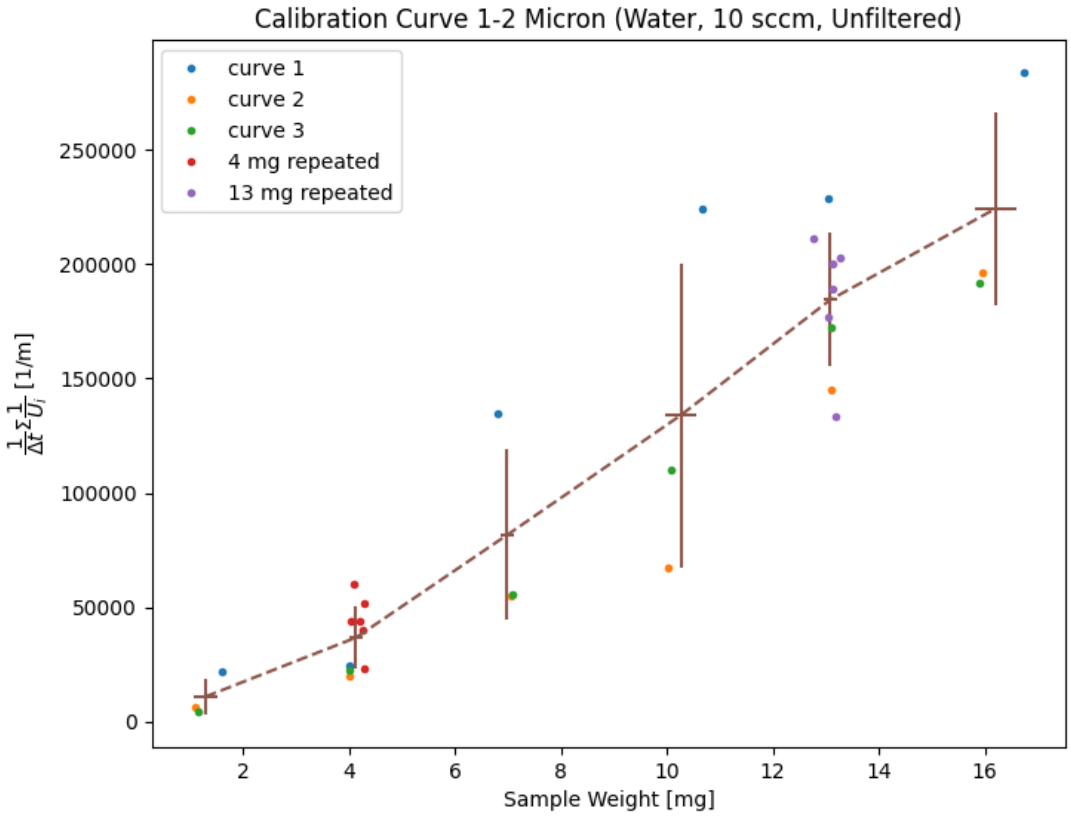

Figure 44. Calibration curve of the 1-2 micron-sized particles in water without filtering.

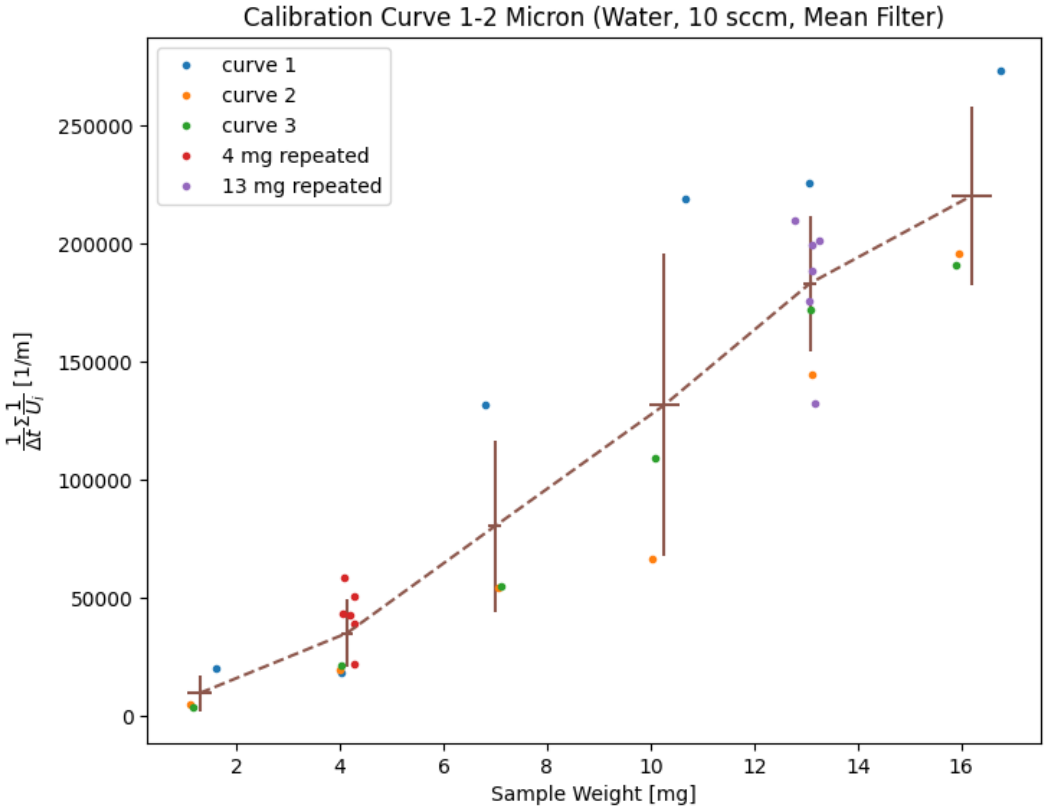

Figure 45. Calibration curve of the 1-2 micron-sized particles in water using the mean filter.

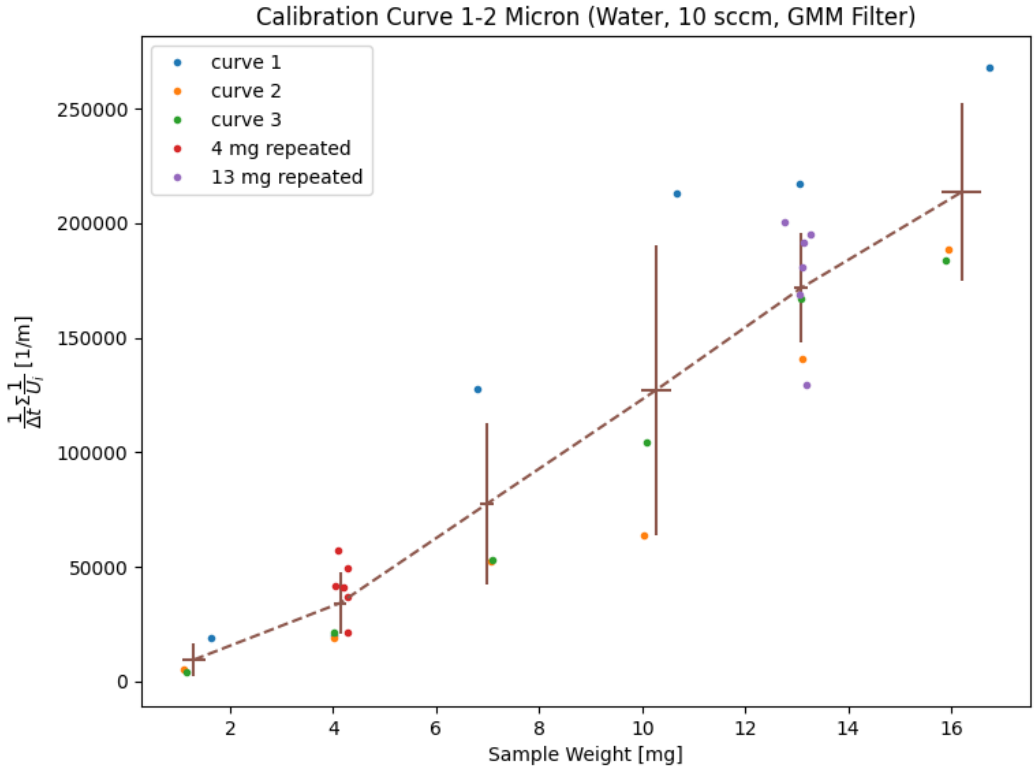

Figure 46. Calibration curve of the 1-2 micron-sized particles in water using the GMM filter.

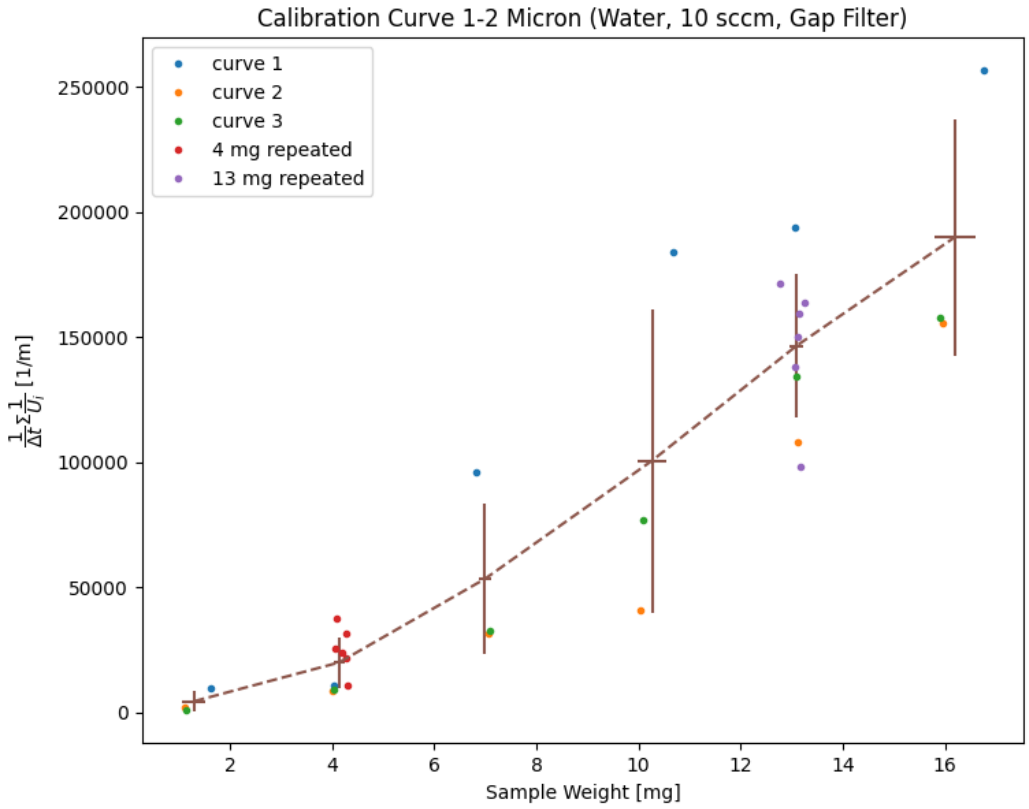

Figure 47. Calibration curve of the 1-2 micron-sized particles in water using the gap filter.

4.4.4 1-2 Micron Particles in Aqueous Glycerol

Comparing the results between measurements in water and in aqueous glycerol reveals a few key differences between the two fluids. The overall signal magnitude in aqueous glycerol is lower while the background added measurements of the bubbles is higher, e.g. compare the magnitude of the 1 *mg* measurement in water (Figure 44) to that of the one in aqueous glycerol (Figure 48). Subsequently, the ratio between the two is much lower in comparison to water. The statistical uncertainty in the measurement results appear to be similar. Observed during the measurements was a much a higher density of bubbles, or a much higher gas holdup, even for the lower gas flow rate used (Figure 32).

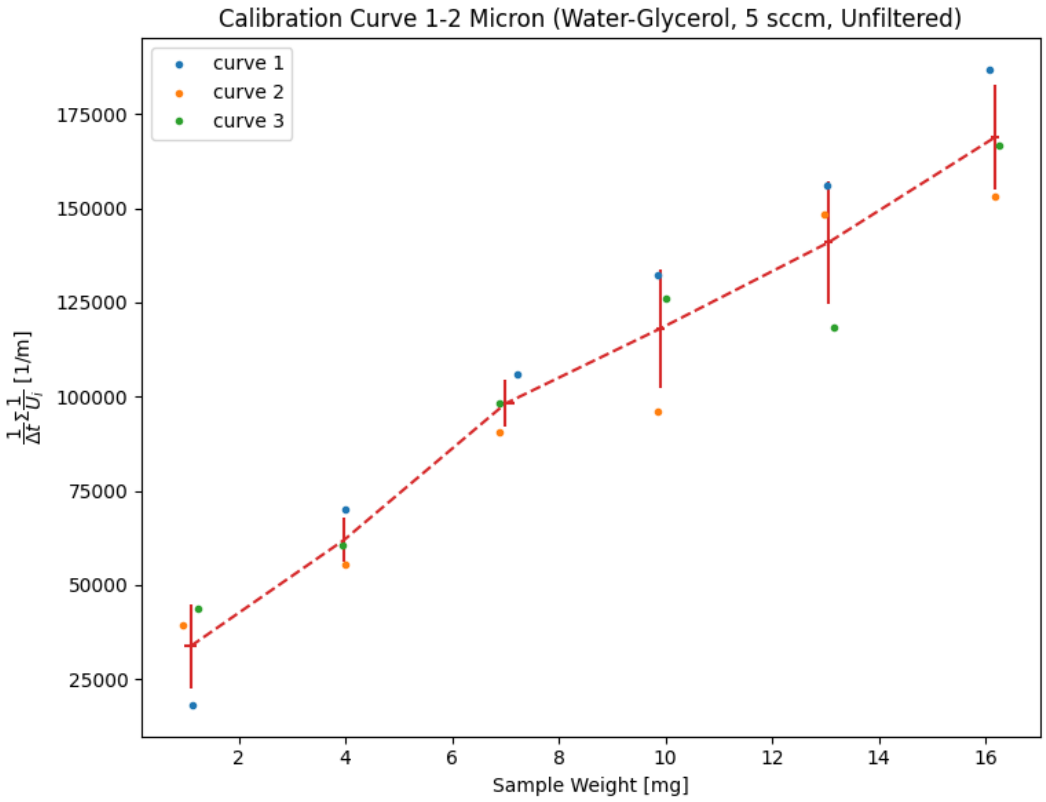

Figure 48. Calibration curve of the 1-2 micron-sized particles in aqueous glycerol without filtering.

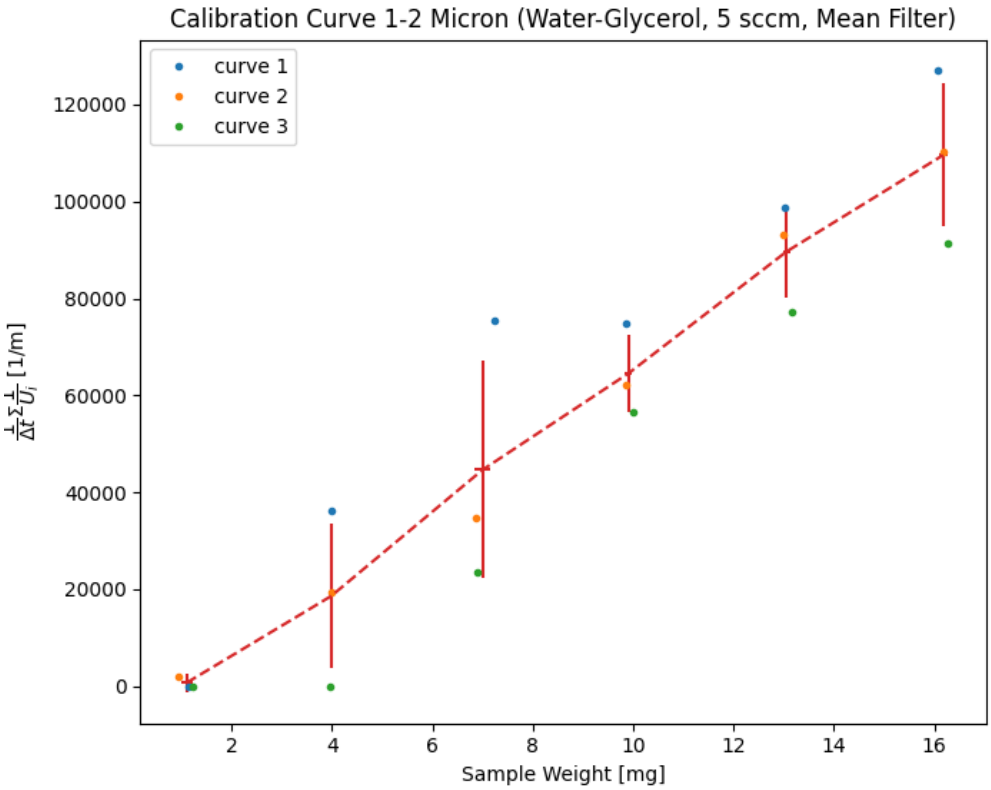

Figure 49. Calibration curve of the 1-2 micron-sized particles in aqueous glycerol using the mean filter.

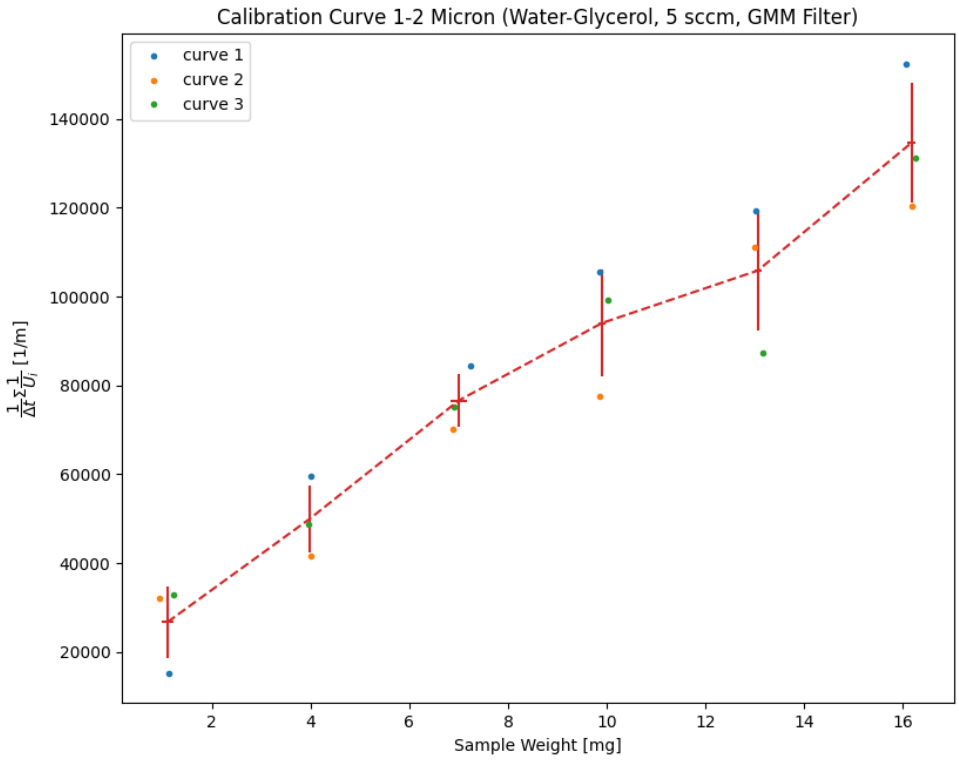

Figure 50. Calibration curve of the 1-2 micron-sized particles in aqueous glycerol using the GMM filter.

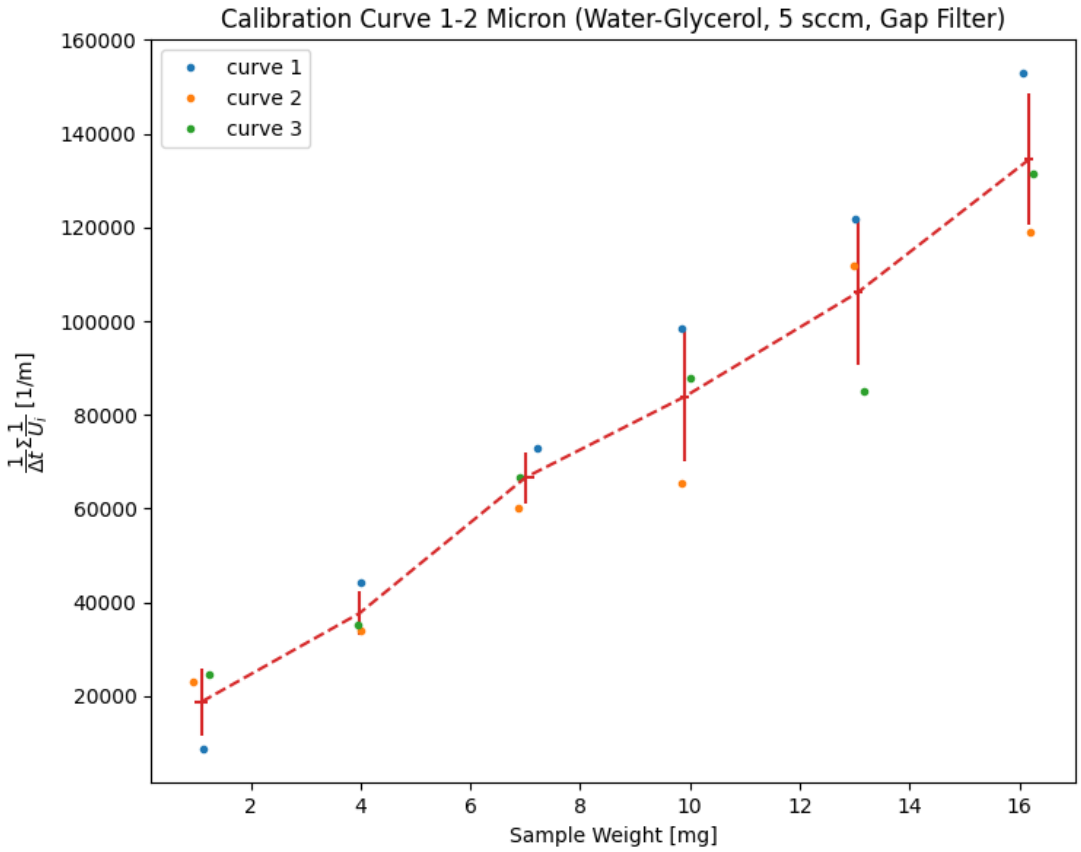

Figure 51. Calibration curve of the 1-2 micron-sized particles in aqueous glycerol using the gap filter.

4.5 Variations in the Gas Flow Rate and Measurement Depth

As mentioned in subsections 2.2 and 4.3, the addition of bubbles results in time gaps in the obtained data sets due the laser beams or the measurement volume being blocked. The frequency at which this occurs is expected to be dependent on the gas holdup and the total path length through the liquid.

To study this effect, several measurements were conducted using all three particle sizes in water for varying gas flow rate over multiple measurement depths. Results are given in Figure 52 through Figure 54. The original data set contains several more measurement depths for each gas flow rate, however, due to reflections that started occurring from 13 *mm* inwards these data points had to be discarded.

Given the relation for the decay in data rate as function of the gas holdup and the measurement depth in Equation 12, it was expected that the results for the concentration measurements would show a similar exponential decrease. Looking at the individual data points reveals that not all data points adhere to the predicted exponential shape, though it is difficult to make conclusions based on the limited data set.

To expand the data set for comparison with Equation 12, a mean of all the different gas flow rates is taken and used for fitting. This approach is not ideal, as the gas flow rate, which is directly correlated to the gas holdup influences the shape of the exponential. From literature [17], the expected change in gas holdup between 5 sccm and 25 sccm is around a factor of ~3 (from roughly 2.5% to 7-7.5%). Nonetheless, the results may still be used to infer some level of agreement with Equation 12 for the nano and 1-2 micron particles.

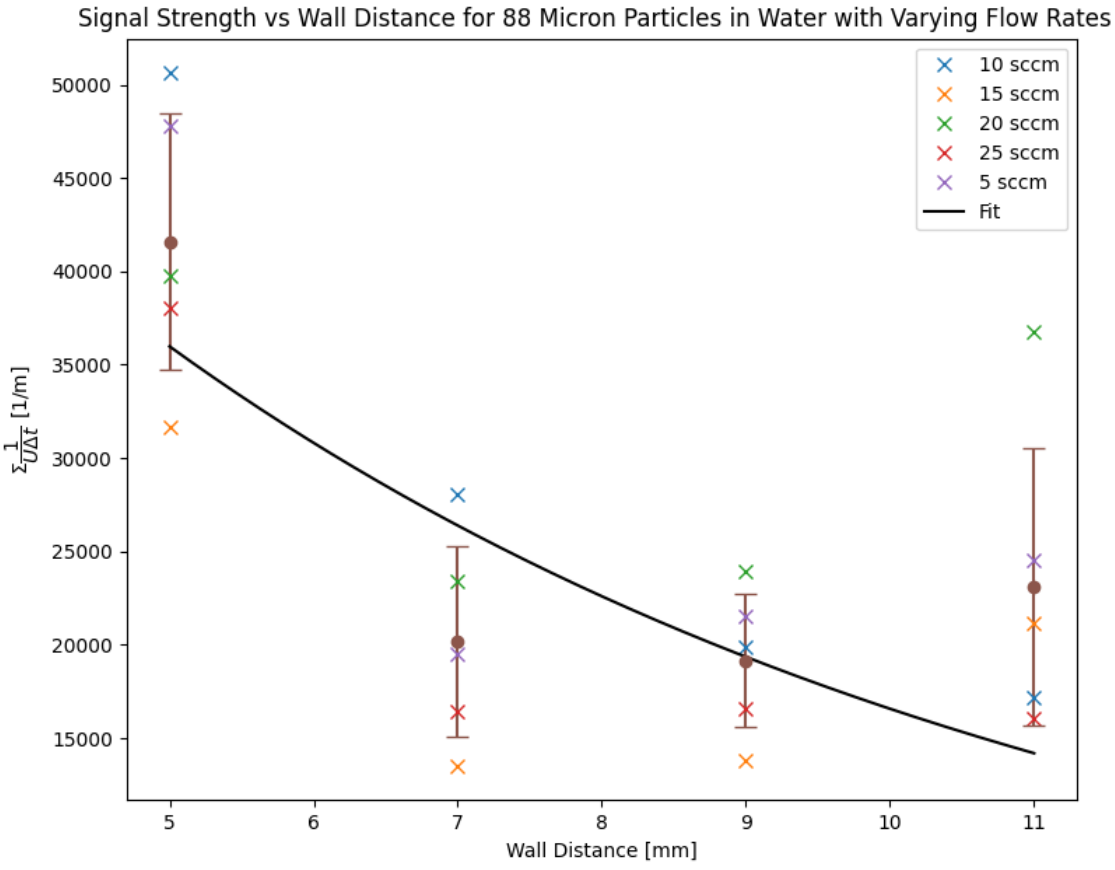

Figure 52. Decay measurements of the measured concentration for 88 micron -sized particles in water.

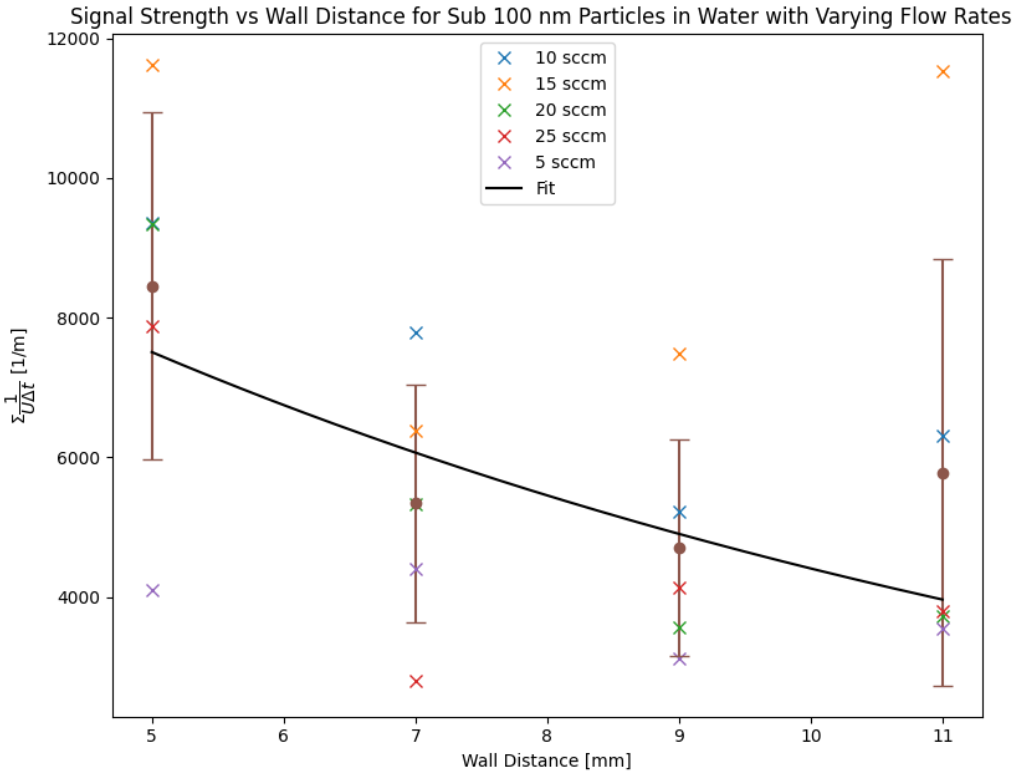

Figure 53. Decay measurements of the measured concentration for nano-sized particles in water.

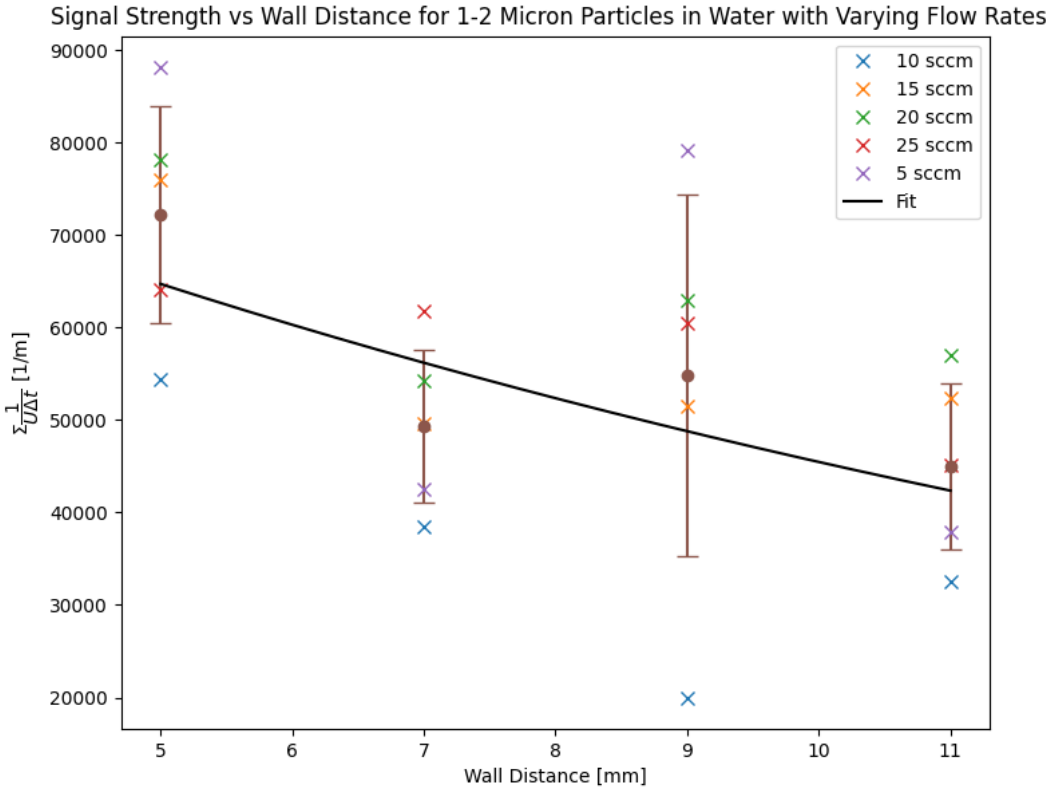

Figure 54. Decay measurements of the measured concentration for 1-2 micron-sized particles in water.

4.6 Flotation Measurements

Finally, longer measurements of around 30 minutes were performed using 1-2 micron particles in demineralized water and aqueous glycerol to obtain time series data during flotation. Measurements were limited to the 1-2 micron powder due to time constraints and due to the higher overall particle-to-bubble signal ratio of the 1-2 micron powder. Samples of 10 *mg* were added after 5 minutes of bubbling and the results were processed using GMM, which has been observed to perform adequately for the 1-2 micron powder in water, i.e. similar conditions that produced the velocity distributions in Figure 30. For the time series, a moving average window of 5000 realization is used. The results are displayed in Figure 55 and Figure 56.

To evaluated the effectiveness of the proposed oil layer for particle collection, similar measurements were repeated with the added layer (see subsections 3.1.4 and 3.2.3.3). Expected is that the signal should drop exponentially in time, similar to the relation given in Equation 18 and the results obtained by Lakerveld [17].

4.6.1 1-2 Micron Particles in Water

When looking at the results obtained in water in Figure 55, a clear distinction is observed before and after the particles are added to the column (particles are added around 5 minutes into the measurement, here indicated by a dashed red line). The overall timespan that is needed for the particles to disperse and mix in the liquid is in the order of seconds. Given the shape of the signal, the moving average window reveals a significant presence of low frequency components in the flow. On average, the magnitude is consistent with the magnitude found in the calibration curve measurement in Figure 46. A slight decrease over time is observed for all the measurements without the added oil layer. Aside from some observed dips in the signals, especially in measurement 1, the results in the top graph (measurements 1-3 in Figure 55) are consistent in terms of the average magnitude and the standard deviation of the signals.

During the measurements it was observed that a significant number of bubbles were attaching to the inner column walls which influences both the gas holdup and the obtained data rate. In particular, when the bubbles get stuck in front of the laser the data rate suddenly plummets and subsequently also the measured concentration. Distinct examples of this occurring can be seen in measurement 3 in Figure 55 (blue line) at around 12, 13.5, 20.5, 21.5 and 26 minutes into the measurement.

Finally, looking at the oil film results (Figure 55, measurements 4 and 5) suggests that the added layer does not provide any additional benefits for particle collection. Specifically, the averaged time series for measurement 5 shows a signal that is also similar to measurement 1-3 in terms of the average magnitude and the standard deviation of the signal.

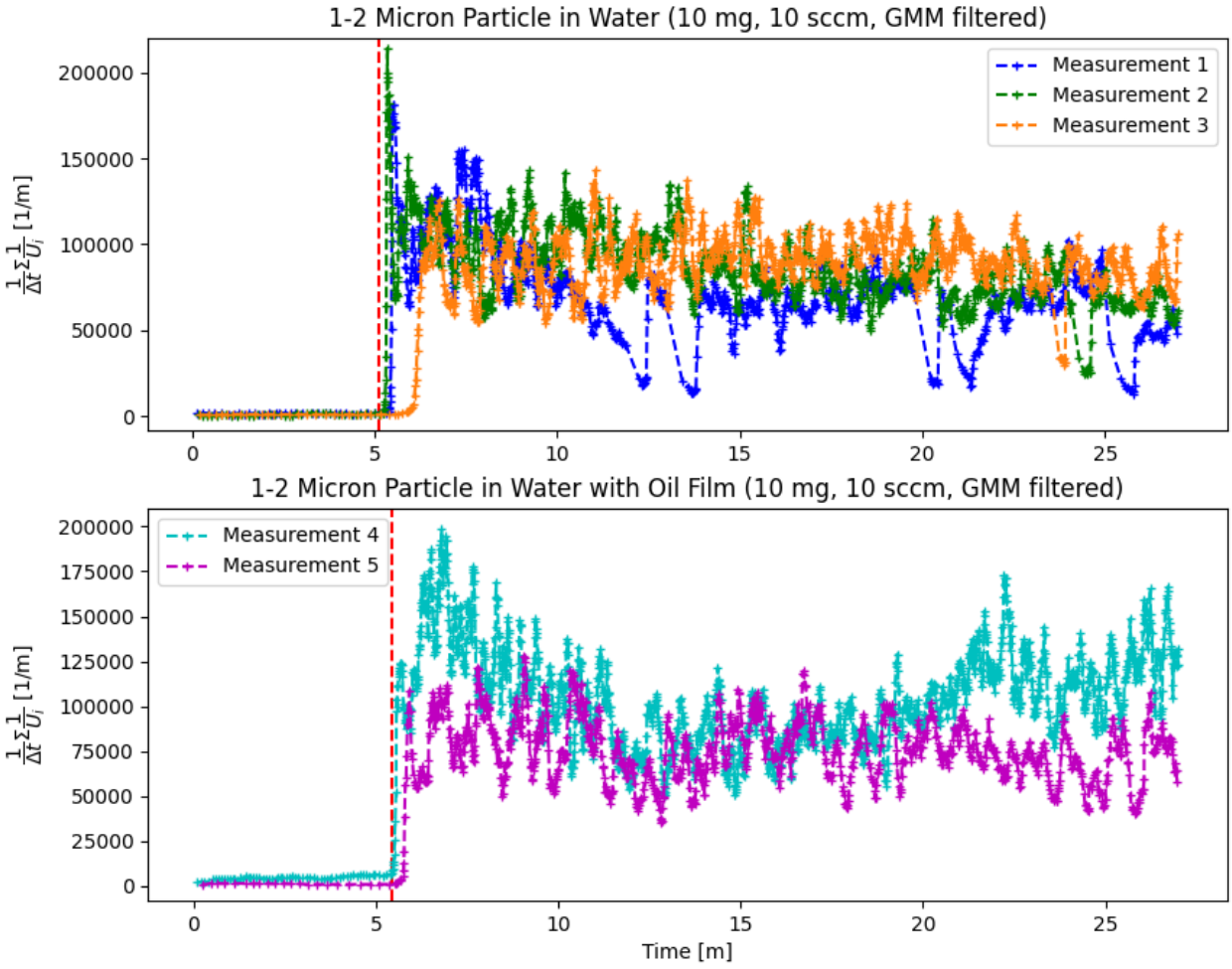

Figure 55. Time series of 1-2 micron-sized particles in water filtered with GMM. Top: without the added oil layer. Bottom: with the added oil layer. Particles are added at the red line at around 5 minutes.

4.6.2 1-2 Micron Particles in Aqueous Glycerol

Similar to the results obtained in Figure 48 through Figure 51, there is a significant signal present before adding the particles (Figure 56). A similar average magnitude is obtained when comparing measurements 1 and 2 in Figure 56 to the calibration curve measurements in Figure 50. The results without oil also appear to be consistent with one another in terms of the average magnitude and the standard deviation of the signal.

In contrast to the results obtained in water (Figure 55), a substantial increase in the magnitude of the standard deviation is observed.

Interestingly, when looking at measurement 4 in Figure 56 with the added oil, a reduction in the variation of the signal over time can be observed after the first few minutes of adding the particles, whereas the standard deviation for measurement 3 appears to be more stable.

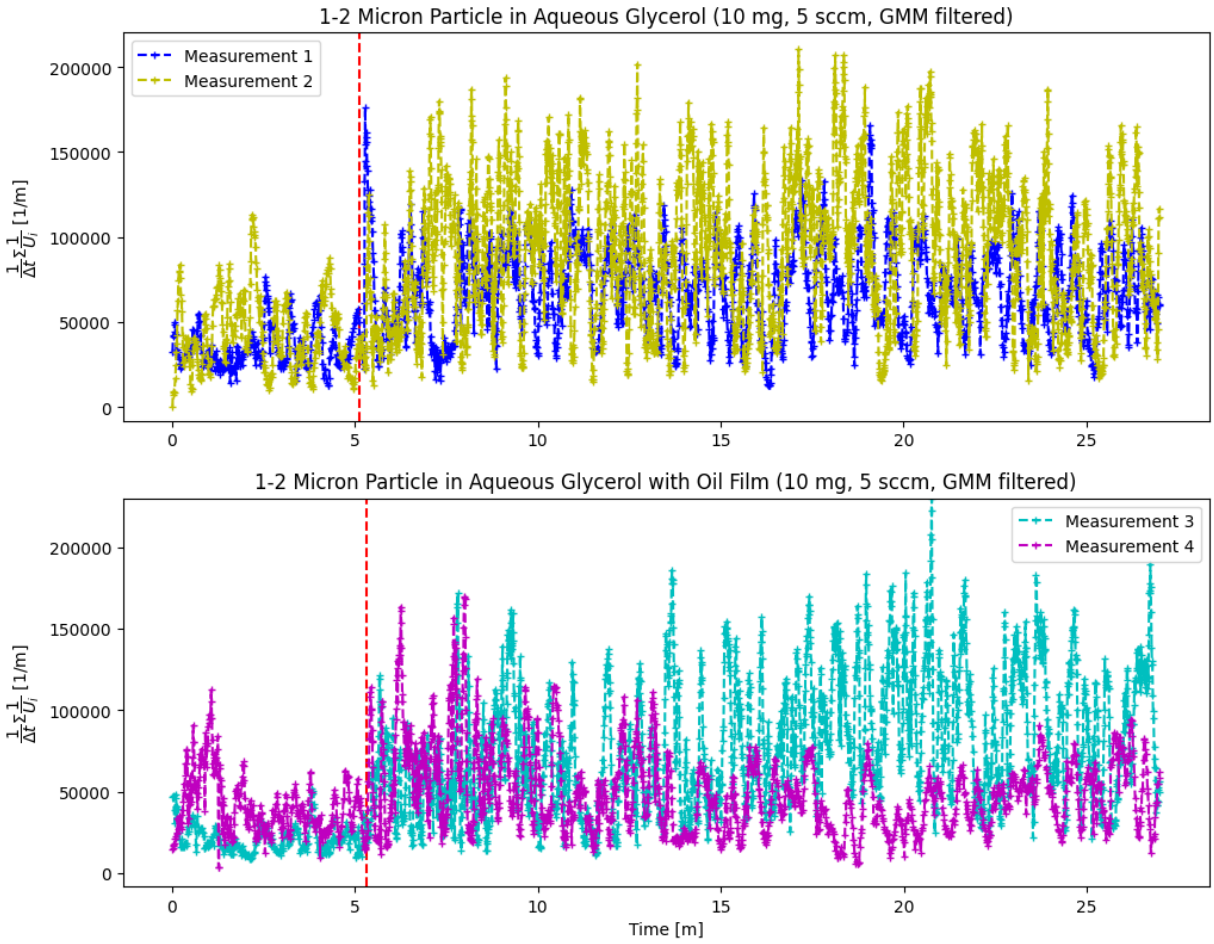

Figure 56. Time series of 1-2 micron-sized particles in aqueous glycerol filtered with GMM. Top: without the added oil layer. Bottom: with the added oil layer. Particles are added at the red line at around 5 minutes.

5. Discussion

This chapter is reserved for the interpretation of the various measurement results and for the discussion of the used methodology and the reasoning used. Section 5.1 goes into detail on the used materials and the setup, in sections 5.2 and 5.3 the results obtained in two- and three-phase flows are discussed, section 5.4 goes into more detail regarding the time series measurements and finally, in section 5.5 recommendation are given for future studies.

5.1 Experimental Setup

5.1.1 The Perspex Flotation Column

Following from observation made during the experimentation and the post-processing of data, a few comments can be made regarding the setup and the used methodology. The column, as mentioned in chapter 3, was taken from a number of different studies involving the investigation of flotation with Laser Induced Fluorescence (see Lakerveld [17] and Grooten [18]). While the design is sensible for LIF due to the reduction in distortion around the edges, it appears that the added complexity is unnecessary or even detrimental in LDA. This difference is due to the different ways in which lasers are used. In LIF a sheet is projected onto the column, where distortion plays a much larger role, while in LDA measurements are taken locally. Extra reflections added by the added interfaces results into a rejection of a non-irrelevant amount of data. Normally, these reflections can be simply filtered out by applying a high pass filter, as the reflections show up on the measurement results as a sharply peaked distribution around 0 *m/s*. However, due to the very low velocities involved in this study, there is a significant overlap present. Even when the overlap is not complete, the loss of realizations close to 0 *m/s* would result into a significant degradation of the signal as the contributions to the density computation scale with the inverse of the particle velocity.

Furthermore, the chosen shape of a cylinder also limits the potential use of multiple velocity components to increase the accuracy of the measured total particle velocity, which in reality is the sum of three orthogonal components. Having different interface shapes for the horizontal and vertical components results in a relative shift of the measurement volume, this gives rise to the question whether results obtained from coincidence measurements can accurately be described to the same particle. As a result, a choice was made to only involve the vertical component in the column measurements when doing density computations. Given the shape of the velocity distributions for both measurement directions and given that the dominant flow pattern is in the vertical direction, this was deemed to be the most sensible choice.

5.1.2 The Mass Flow Controller

Based on the findings of Grooten, the mass flow controller that is used to inject air in the sparger has a limited range in which it is accurate. Specifically, the lower limit appears to be around 5 *sccm*. However, due to the observed bubble density in aqueous glycerol it is likely preferable to be able to inject an even smaller amount of air to get a more representative holdup. To compare the gas holdup with the ones found in previous studies, a measurement was conducted, the results show a linear relation with the gas flow rate and are in relative good agreement with the ones found by Lakerveld. Some discrepancy is likely due to the slight difference in glycerol content.

5.1.3 Column Mounting

Another limitation is the limited positional accuracy that is provided by the used brackets to fix the column. Since the brackets are screw tightened, there is some error in the horizontal direction due to variation in how much the screws are tightened. Furthermore, it was observed that the rubber pads on the brackets degraded over the span of all the measurements (Figure 64) resulting in a drift of 1 or 2 *mm* in the vertical direction.

5.1.4 Water-Glycerol as a Modelling Fluid

Given that the contents of this study are a prelude to possible further experiments performed with molten salt, it cannot be overlooked that the use of aqueous glycerol can only provide limited information regarding the effectiveness of flotation for a set of different parameters. While the kinematic viscosity can be close matched by varying the glycerol content, other important parameters such as the surface tension and the density remain significantly different. Both of which significantly impact the characteristics of the bubbles and flotation process.

5.1.5 Fluid Heights

Regarding the used experimental methodology, to keep experimental conditions similar in between measurements, an identical fluid height was maintained during preparation (which is before injecting air). However, due to adding the particles later and rising with demineralized water, there is some unnecessary variation added in the resulting fluid height, which could impact the local flow pattern in the column. In hindsight, it most likely better to first add the particles and then add water until the desired height is reached. Also, during sample preparations it was observed that the used powders are not completely dry. For better consistency it may be preferable to first dry the samples.

5.2 Two-Phase Flow Measurements: Solids in Liquid

To study the viability of using LDA as a method for measuring particle densities, measurements were performed in a simplified case where only two-phase flow is considered. Looking at the results obtained in section 4.2, several things can be concluded regarding the fundamental principles. The results shown in Figure 27 show that even when the particle velocities are varied via the different dial settings on the mixer, the resulting density plots are in reasonable agreement with each other for both velocity components. This gives credence to the idea that the inverse velocities can be accurately used to separate the rate at which particles are detected from its dependency on the local flow field. There are some small observable difference in the magnitude found, however this may be resulting from only including one velocity component and from the reduction of the number of particles in the fluid due to the deposition of particles on the container floor and walls (as the measurement were performed in series in ascending order). As mentioned in subsection 4.2, another explanation may be a change in the shape of the flow field.

Density plots were obtained for a variety of different particles, including tracer particles and molybdenum particle of three different sizes. These plots show that generally, similarly shaped results are obtained for both measurement directions (Figure 26 and Figure 27). However, the magnitude of the density does change with the particle type. To answer the question whether the current LDA setup is suitable for detecting particle in the nano-size range, identical measurements were performed using three different nano powders from different manufacturers. These measurement showed very similar results, both in shape and in magnitude, and subsequently, only one of the powders was selected for use in the three-phase measurements. Looking back, when putting the results of these nano powder measurement results in context with the obtained particle size measurements in section 4.1, it can be concluded that the nano powder that was selected beforehand contains a certain content of particles with a size of around 1 micron. Consequently, the results are inconclusive and similar density and particle size measurements should be repeated for different nano powders to get a better resolution. Still, the fact that the other two powders showed a similar result for the density plots does imply that it may indeed be possible.

Another important result is the measurement of the average density as function of the used sample weights. The obtained graph for 1-2 micron-sized particles in Figure 28 shows a clear positive correlation between the two. The shape of this correlation can be seen to be either exponential or linear in nature.

Furthermore, even when the density is not averaged over the measurement depths, the same correlation can be shown for each individual measurement point. Some of the results for a few different measurements depths had to trimmed however, due to the clear prevalence of reflections in the data set.

5.3 Three-Phase Flows Measurements: Solids in Liquid with Bubbles

5.3.1 Influence of the Bubbles on Measurements

As predicted by the literature provided in section 2.2, complexity is added when a gaseous phase is introduced into the mix. Analogue to the findings of Harteveld [24] and Mudde et al. [25], observations can be made of the occurrence of time gaps in the velocity data due to the passing of bubbles either in front of one the beams or through the measurement volume (Figure 29). Comparing results before and after adding particles reveals that the particles typically show up in the measurement results as a Gaussian peak with a low spread (Figure 30). Often, the results from measuring just the bubbles shows a somewhat similar shape, however sometimes this goes paired with a tail going towards higher vertical velocities. This is possibly due to the spread in bubble sizes, something which is also observed during the experiments (Figure 32).

5.3.2 Bubble vs Particle Detection Rates

In demineralised water, the signals produced by the bubbles are typically much lower than the ones produced by the particles except for low sample weights while using the nano powder. In contrast, the signals produced by the bubbles in aqueous glycerol show a consistently high signal, sometimes even data rates up 600-800 can be observed before adding the particles. Subsequently, it was assumed that the glycerol may contain either some contamination or that solid particles had formed in the glycerol. An investigatory measurement was performed using the two-phase flow setup with the same mixture, however, no significant contamination was detected. What is most likely the case is that the observed relative high density of bubbles (when compared to the water measurements) is the cause of this high data rate. Interestingly, another difference observed is that the mean velocity of the bubble signal is closer to the particle velocity mean in comparison to the results from water. This could be a result from a combination of the lower gas flow rate used and the relative higher viscous drag on the bubbles which brings the velocities more in line with those measured for the particles. The observed tendency of bubbles in aqueous glycerol to produce even more Gaussian like velocity distributions could also be due to the increase in drag force.

5.3.3 Filter Methods

The effectiveness of the used data filters seems somewhat mixed. The assumptions made for using the mean filter can be considered approximately true in the case the particle signal is much higher than the bubble signal, which somewhat limits its use to cases where there are a significant number of particles present and when the gas holdup is low (subsection 2.2.2). The GMM filter has a more relaxed assumption, which is that the particles produce a Gaussian shaped distribution while the effect of the bubbles can be assumed to be only approximately Gaussian. Consequently, the GMM filter can be used for a wider set of experimental conditions. There are however, some experimental conditions in which the algorithm fails to separate both peaks. This typically happens when the number of data counts is relatively low or when the bubbles completely overlap the particle measurements, as is the case for low sample weights in aqueous glycerol and for low weight samples using the nano powder (Figure 33 through Figure 35). The gap filter is somewhat more difficulty to evaluate due to the high dependence on how the minimal gap size and the removal window are chosen. Harteveld reported in his study that for the values he had chosen the resulting rejection of velocity realizations was around 60%, he did however, consider flows with much higher gas holdups. In this study the values were chosen by observing the signal gaps manually (subsection 4.3). Even though the gaps have been observed to be of varying size for different experimental conditions, fixed values are used. It is likely that the values need to be adjusted

based on the experimental conditions, which can be satisfactory when only the velocity profile is of interest, but makes comparison quite difficult when performing particle density computations.

5.3.4 Calibration Curves

The figures presented in section 4.4 show positive correlation between the sample weight and the obtained concentration signals. Results obtained with the different filters are almost identical, aside from the gap filter typically showing a lower magnitude in the measured concentration, which is due to the higher rate of data rejection. The spread between measurements is observed to be typically higher for the high sample weights. It is not quite clear as to why this is the case, one explanation could be that the exact position of the measurement volume plays a much larger role for higher data rates. Another explanation is that due to the presence of some moist in the used powders, that some samples have clusters in them which fail to separate correctly resulting in fewer measurable particles. Some clusters were observed when preparing the DLS samples and these even failed to separate after vortexing.

While the resulting calibration curve shapes are similar between the different particle sizes (subsections 4.4.1-4.4.3), their magnitudes can be observed to be different. Given this observation, it is not possible to make absolute measurements of density due to lacking information regarding the particle diameter when using LDA only. However, if the distribution can be assumed to remain constant or if the distribution is monodisperse, it is possible to do relative measurements as the scaling factors in Equation 13, i.e. the effective probe volume cross section A_i and the (effective or mean) particle diameter d_i, can be assumed to be constant. A further limitation is predicted by literature as LDA is stated to be only sensitive to particles with sizes in the same range as the used wavelength of light.

5.3.5 Gas Flow Rate and Measurement Depth

The measurements of the particle concentration as function of the gas flow rate and the measurement depth were performed to evaluate the reduction in signal due to the passing of bubbles through the laser beams (section 4.5). Unfortunately, a lot of data points were observed to have reflection and had to be rejected while measurements were also only carried out once due to time constraints. The result is a fairly low number of data points which gives a fairly inconsistent picture of how the obtained concentrations are correlated to the measurement depth and the gas flow rate. To get more information out the data points, the results are averaged over the various gas flow rates to produce an average over measurement depth, which is not ideal as the shape of the expected exponential shape changes with the gas flow rate (Equation 12). When fitting this to the exponential shape from Equation 12, a reasonable agreement can be observed for the 1-2 micron and nano-sized particles (Figure 52 through Figure 54). Repeated measurements would have to be carried out to produce more definitive results.

5.3.6 Uncertainty Quantification

Something which is uncertain is whether the computed uncertainties can be deemed reasonable. While computations for the added uncertainty from the calibration uncertainty and the random uncertainty are relatively straightforward, computations for the used data filters are more complex due to their asymmetric nature of removing velocity realizations. As a result, a simple estimate was used for estimating the filter induced uncertainty. It may be possible to obtain more accurate values when evaluating the resulting output of the filters with synthetic data, though this would also require making assumptions on the data distributions, which is also not desirable.

5.4 Particle Collection and Flotation

Looking at the results obtained in section 4.6, observations can be made regarding flotation and the used oil film for particle collection. The resulting time series in Figure 55 and Figure 56 show consistency in the mean and the standard deviation between the different measurements when no oil film is applied (top

graph in both figures). The applied moving average window reveals the low frequency components in the flow and a slight downward trend is observed. A possible explanation could be that even when there is no collection device, there is still a deposition of the particles on the glass wall. This is consistent with observations of particles being present on the inner column surface around the fluid height when performing cleaning handlings in between measurements. What is quite different, is that the standard deviation in aqueous glycerol, as observed in Figure 56, is much larger when compared to water in Figure 55. As the signal before adding the particles is also significant in Figure 56, a likely explanation could be the added effect of the higher gas holdup or the larger quantity of bubbles in the column.

Measurements that included the oil film display some interesting results, in most case no reduction in particle concentration is observed (Figure 55 and Figure 56, the bottom graphs). However, only in Figure 56, measurement 4, a reduction in the standard deviation is observed to be present from 6 to 11 minutes. After which it reaches a standard deviation comparable to the one found before adding the particles, i.e. prior to the 5 minute mark. As mentioned in section 4.6, issues arose during the experimentation where bubbles were clinging to the glass surface, which resulted into the laser being completely blocked. Subsequent reductions in signal can be most easily observed in Figure 55, measurement 1, where the blue line displays random large dips in the concentration. In some measurements the issue resolved itself after some time, however, during others, it was required to physically insert a rod to remove them by hand. Consequently, the oil layer was disturbed and partially mixed. This could explain the single result showing a decrease as this is much more analogues to the application of oil in the mining industry where the oil is mixed together with the injected gas.

Interestingly, the practical issue with the bubbles sticking to the inner column also arose earlier during the experimentation when aqueous glycerol was first used. In response, it was initially decided shift focus on water alone. When looking back however, the date is consistent with a measurement in which oil was first used in a test. It is quite likely that the inner column was wetted with a very thin layer of oil which forms a stable surface for the bubbles to adhere to.

5.5 Recommendations

Concluding from the practical aspects of this study, there are a few recommendations that could noticeably improve the overall quality of the measurements. The most important change is likely to be a complete overhaul of the column design. Due to the small diameter of the inner column and the corresponding curvature it is difficult or even outright not possible to utilize both laser sets for coincidence measurements. Having these two components improves the accuracy of the measured total particle velocity and should increase the accuracy of the particle concentration measurements. To this extend, it is recommended to utilize a flat window. Furthermore, constructing the backwall with a non-reflective material may also reduce the amount of observed reflections in the data sets and a more robust solution should be implemented to fixate the setup to get more consistency in the measurement location.

The few measurement results of aqueous glycerol have shown that viscous fluids can negatively impact the results due to the relative higher gas holdup. Depending on the exact experimental conditions (i.e. properties of the fluid and the amount of gas injected), it may or not may be possible to separate the added data points from the bubbles. Instead, it may be possible to completely circumvent the added complexity of the added gaseous phase by completely separating the measurement area from the area where flotation takes place. One option could be to integrate a loop in which measurements and flotation are performed is separate place in the loop. This would however, necessitate the use of some kind of pump, which could be difficult with molten salt. Another potential option is to construct the flotation column in such a way that it has an inner and an outer channel, where gas is injected into the inner channel and measurements are only performed on downflow in the outer channel.

If taking measurements over a certain range of measurement depths is desired, then the decay in the data rate and the subsequent measured concentration as function of the measurement depth and the gas holdup should also be considered. To address this, it may be of interest to repeat the measurements performed in subsection 4.5 to verify the theoretical exponential nature of this decay. When the spatial distribution of the particles in the fluid can be considered homogenous, the aforementioned decay could potentially be compensated by proportionally sampling extra velocity realizations from the original data set. Moreover, since the current setup only allows for the measurement of two simultaneous velocity components, the resulting velocity weight factor is continuously underestimated due to the lack of a third component. The third velocity component could potentially be estimated by utilizing CFD models.

6. Conclusion

Noble metal fission products in molten salt reactors have been known to deposit on crucial reactor components which reduce their effectiveness and their lifetimes. Helium bubbling is one of the proposed method of extracting these fine particles from the molten salt and has been a well-studied topic during the recent years. Concluding from studies performed with Laser Induced Fluorescence, which has a limited applicability to real molten salt, Laser Doppler Anemometry is proposed as a measurement technique for measuring and monitoring particle concentrations. In this thesis, the use of Laser Doppler Anemometry is investigated for two- and three-phase flows using molybdenum particles of different sizes in demineralized water and aqueous glycerol. Three-phase flow measurements have been carried out using a Perspex flotation column.

Using tracer particles, measurements in two-phase flows have shown that inverse velocity weighting is a viable strategy for compensating the flow field dependent data rate to obtain estimates of the particle concentrations. For a range of different samples weights, a clear positive correlation was demonstrated to the computed particle concentration. This correlation is observed to be approximately linear in form. Further measurements with three different nano powders have demonstrated a potential capability for Laser Doppler Anemometry to detect particles as low as 100 *nm*, however, more measurements need to be performed to get a more conclusive end result.

Analogue to results found in the available literature, extra complexity due to the addition of a gaseous phase in the flotation column has been observed to result in time gaps in the data series due to the blocking of one of the laser beams or the measurement volume by passing bubbles. Calibration curve and subsequent time series measurements were carried to shown the same viability for three-phase flows. The calibration curves can be used to perform relative measurements of the particle concentration. To estimate the effect of bubbles on the measured concentration, variations of different gas flow rates and measurement depths were utilized to compare the result to relations found in literature. However, the results remain inconclusive due to a lack of measurement points that were not affected by reflections in the data sets. Finally, to simulate the flow properties of molten salt, similar calibration curve measurements were carried out in aqueous glycerol which have shown that the increase in viscosity is problematic for measurements using Laser Doppler Anemometry due to the higher number of bubbles observed and due to the larger overlap of the velocity distributions of bubbles and particles.

While the results of this study indicate that the use Laser Doppler Anemometry is viable for relative measurement of monodisperse particles, the simulated conditions using simulant materials can only give a limited view. Future studies involving molten salt will have to be carried to demonstrate the viability of using Laser Doppler Anemometry for particle concentration measurements under representative experimental conditions.

References

[1] International Energy Agency; Nuclear Energy Agency, “Technology Roadmap,” 2015. [Online]. Available: https://www.oecd-nea.org/pub/techroadmap/techroadmap-2015.pdf. [Accessed January 2019].

[2] P. Kaplan, “Developing countries eye nuclear power: report,” Reuters, 2008.

[3] International Atomic Energy Agency , “Nuclear Power Reactors in the World,” International Atomic Energy Agency , Vienna, 2018.

[4] Nuclear Energy Advisory Committee; Generation IV International Forum, “A Technology Roadmap for Generation IV Nuclear Energy Systems,” December 2002. [Online]. Available: https://www.gen-4.org/gif/upload/docs/application/pdf/2013-09/genivroadmap2002.pdf. [Accessed January 2019].

[5] Generation IV International Forum, “Gen IV International Forum,” 2018. [Online]. Available: https://www.gen-4.org/gif/jcms/c_9260/public. [Accessed January 2019].

[6] Nuclear Energy Agency; Generation IV International Forum, “Technology Roadmap Update for Generation IV Nuclear Energy Systems,” January 2014. [Online]. Available: https://www.gen-4.org/gif/upload/docs/application/pdf/2014-03/gif-tru2014.pdf. [Accessed January 2019].

[7] K. Furukawa, L. Alfred, Y. Kato and K. Mitachi, “Thorium Molten-Salt Nuclear Energy Synergetics,” *Journal of Nuclear Science and Technology,* vol. 27, no. 12, pp. 1157-1178, 1990.

[8] J. Serp, M. Allibert, S. Delpech, O. Feynberg, V. Ghetta, D. Heuer, D. Holcomb, V. Ignatiev, J. L. Kloosterman, L. Luzzi, E. Merle-Lucotte, J. Uhlír, R. Yoshioka, D. Zhimin and O. Benes, “The molten-salt reactor (MSR) in generation IV: Overview and perspectives,” *Progress in Nuclear Energy,* vol. 77, pp. 308-319, 2014.

[9] J. Campbell, *Molten Salt Reactor (MSR),* Idaho National Laboratory.

[10] H. MacPherson, “The Molten Salt Reactor Adventure,” *Nuclear Science and Engineering,* vol. 90, pp. 374-380, 1985.

[11] M. Rosenthal, P. Kasten and R. Briggs, “Molten-Salt Reactors - History, Status and Potential,” 10 October 1969. [Online]. Available: http://moltensalt.org/references/static/downloads/pdf/NAT_MSRintro.pdf. [Accessed January 2019].

[12] J. Uhlır, “Chemistry and technology of Molte Salt Reactors - history and perspectives,” *Journal of Nuclear Materials,* vol. 360, pp. 6-11, 2007.

[13] C. H. Gabbard, “Development of a Venture Type Bubble Generator for use in the Molten-Salt Reactor Xenon Removal System,” Oak Ridge National Laboratory, Oak Ridge, 1972.

[14] R. Kedl, “The Migration of a Class of Fission Product (Noble Metals) in the Molten-Salt Reactor Experiment,” Oak Ridge National Laboratory, Oak Ridge, 1972.

[15] E. Capelli, “Report static column.,” Delft University of Technology, Delft, 2018.

[16] L. Rozing, “Out-of-Core Bubbling in the Molten Salt Fast Reactor,” Delft University of Technology, Delft, 2020.

[17] I. Lakerveld, “Helium Bubbling in the Molten Salt Fast Reactor. An experimental and analytical analysis of particle entrainment.,” Delft University of Technology, Delft, 2021.

[18] A. Grooten, “Helium Bubbling in the Molten Salt Fast Reactor. Optimisation of measurement methods and reasearch on extraction methods in a flotation column.,” Delft University of Technology, Delft, 2021.

[19] D. Dynamics, “FlowExplorer LDA systems,” 2020. [Online]. Available: https://www.dantecdynamics.com/wp-content/uploads/2020/09/0492_v4-SS-LDA-FlowExplorer.pdf. [Accessed november 2022].

[20] *LDA and PDA Reference Manual,* Skovlunde: Dantec Dynamics A/S, 2011.

[21] K. D. Jensen, “Flow Measurements,” *Journal of the Brazilian Society of Mechanical Sciences and Engineering,* vol. XXVI, no. 4, pp. 400-419, 2004.

[22] Massachusetts Institute of Technology, “Laser Doppler Anemometry [LDA],” Massachusetts.

[23] I. Ayranci, G. Pinguet, N. Selcuk, R. Vaillon and F. Andre, “Effect of particle polydispersity on particle concentration measurement by using laser Doppler anemometry,” *Experimental Thermal and Fluid Science,* vol. 31, no. 8, pp. 839-847, 2007.

[24] W. Harteveld, “BUBBLE COLUMNS. Structures or stability?,” Delft University of Technology, Delft, 2005.

[25] R. Mudde, J. Groen and H. V. D. Akker, “Application of LDA to bubbly flows,” *Nuclear Engineering and Design,* vol. 184, no. 2-3, pp. 329-338, 1998.

[26] K. Ohba, I. Kishimoto and M. Ogasawara, “Simultaneous measurement of local liquid velocity and void fraction in bubbly flows using a gas laser—part I: principle and measuring procedure,” *Technology reports of the Osaka University,* vol. 26, pp. 547-556, 1976.

[27] Z. W. Gan, “Holdup and velocity profiles of monosized spherical solids in a three-phase bubble column,” *Chemical Engineering Science,* vol. 94, pp. 291-301, 2013.

[28] R. v. d. Wall and S. Soo, “Measurement of transport properties of a gas-solid suspension using,” *Powder Technology,* vol. 94, pp. 141-151, 1997.

[29] X. Liu, S. Gao and J. Li, “Characterizing particle clustering behavior by PDPA measurement for dilute gas–solid flow,” *Chemical Engineering Journal,* vol. 108, no. 3, pp. 193-202, 2005.

[30] E. Francke and J. Amouroux, “L.D.A. Simultaneous Measurements of Local Density and Velocity Distribution of Particles in Plasma Fluidized Bed at Atmospheric Pressure,” *Plasma Chemistry and Plasma Processing,* vol. 17, no. 4, pp. 433-452, 1997.

[31] W. M. Farmer, “Measurement of Particle Size and Concentrations Using LDV Techniques,” in *Dynamic Flow Conference,* Tullahoma, 1978.

[32] T. Schlagenhauf, “Expectation Maximization and Gaussian Mixture Models (GMM),” 22 Februari 2022. [Online]. Available: https://python-course.eu/machine-learning/expectation-maximization-and-gaussian-mixture-models-gmm.php. [Accessed November 2022].

[33] H. J. Schulze, Physico-chemical Elementary Processes on Flotation, Amsterdam-Oxford-New York-Tokyo: Elsevier, 1984.

[34] R. Yoon and G. Luttrell, “The Effect of Bubble Size on Fine Particle Flotation,” *Mineral Processsing and Extractive Metallurgy Review,* vol. 5, pp. 101-122, 1989.

[35] R. Prakash, S. K. Majumder and A. Singh, “Flotation technique: Its mechanisms and design parameters,” *Chemical Engineering & Processing: Process Intensification,* vol. 127, pp. 249-270, 2018.

[36] R. Yoon and L. Mao, “Predicting flotation rates using a rate equation derived from first principles,” *International Journal of Mineral Processing,* vol. 51, pp. 171-181, 1997.

[37] J. Ralston and S. Dukhin, “The interaction between particles and bubbles,” *Colloids and Surfaces A: Physicochemical and Engineering Aspects,* vol. 151, no. 1-2, pp. 3-14, 1999.

[38] R. Yoon, “Microbubble Flotation,” *Minerals Engineering,* vol. 6, no. 6, pp. 619-630, 1993.

[39] M. Massinaei, M. Kolahdoozanb, M. Noaparastb, M. Oliazadehb, J. Yianatosc, R. Shamsadinid and M. Yarahmadid, “Hydrodynamic and kinetic characterization of industrial columns in rougher circuit,” *Minerals Engineering,* vol. 22, no. 4, pp. 357-365, 2009.

[40] “Calculate density and viscosity of glycerol/water mixtures,” 4 April 2018. [Online]. Available: http://www.met.reading.ac.uk/~sws04cdw/viscosity_calc.html. [Accessed November 2022].

[41] N. S. Cheng, “Formula for the Viscosity of a Glycerol−Water Mixture,” *Ind. Eng. Chem. Res.,* vol. 47, no. 9, p. 3285–3288, 2008.

[42] S. Mallison, G. Horrocks and G. Mcbain, “Viscosity and surface tension of aqueous mixtures,” in *20th Australasian Fluid Mechanics Conference,* Perth, 2016.

[43] E. Capelli, E. M. A. Frederix, A. Mathur, R. P. Hania, J. Kloosterman and R. Konings, “Noble metal behaviour and extraction in molten salt reactor”.

[44] W. L. Carter, “Decay Heat Generation by Fission Products and 233Pa in a Single-Region Molten Salt Reactor,” Oak Ridge National Laboratory, Oak Ridge, 1968.

[45] T. Dumaire, “FInal Report PhD project,” Delft University of Technology, Delft, 2022.

[46] D. Michaud, “Flotation Principles,” 16 March 2016. [Online]. Available: https://www.911metallurgist.com/blog/flotation-principles. [Accessed November 2022].

[47] J. Groen, R. Oldeman, R. Mudde and H. V. d. Akker, “COHERENT STRUCTURES AND AXIAL DISPERSION IN BUBBLE COLUMN REACTORS,” *Chemical Engineering Science,* vol. 51, no. 10, pp. 2511-2520, 1996.

Appendix A: Product Information

Figure 57. Image of the used 1-2 micron molybdenum powder.

Figure 58. Image of the used sub 100 nm molybdenum powder.

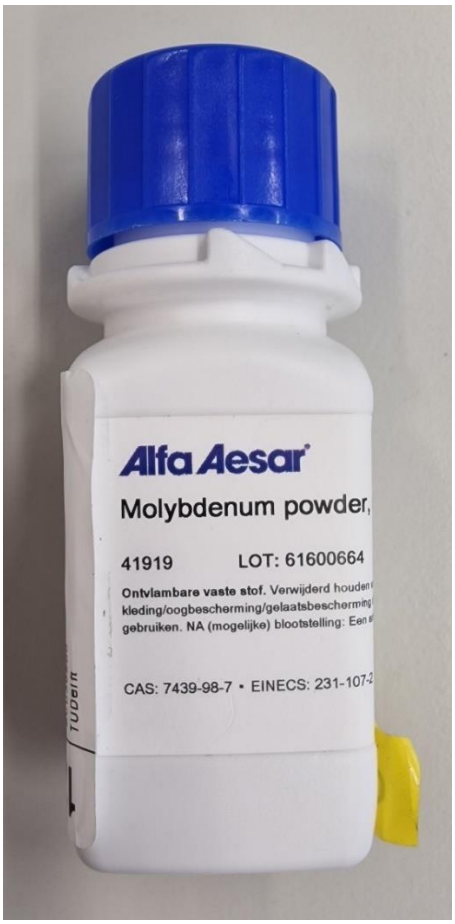

Figure 59. Image of the used 88 micron molybdenum powder.

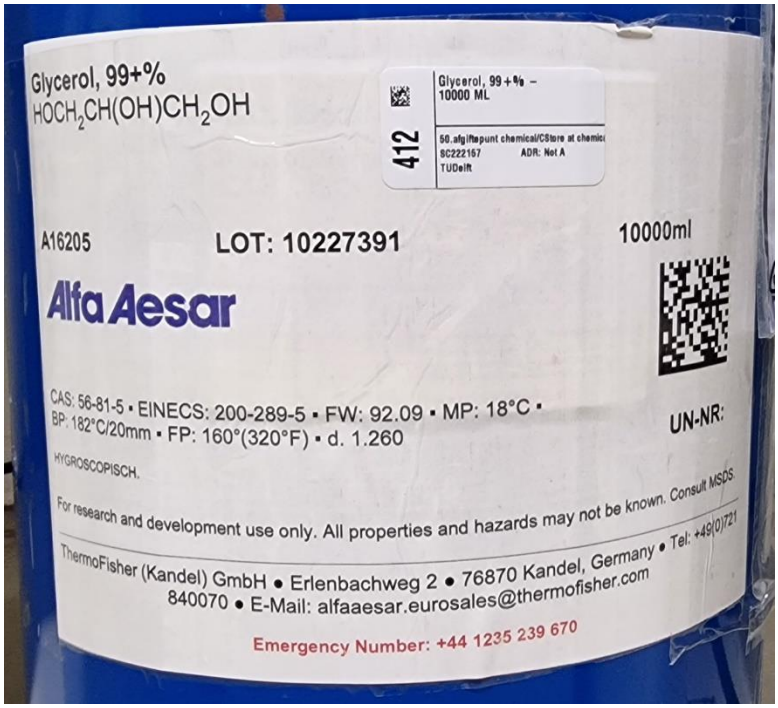

Figure 60. Image of the used glycerol.

Appendix B: 88 Micron Size TEM Images

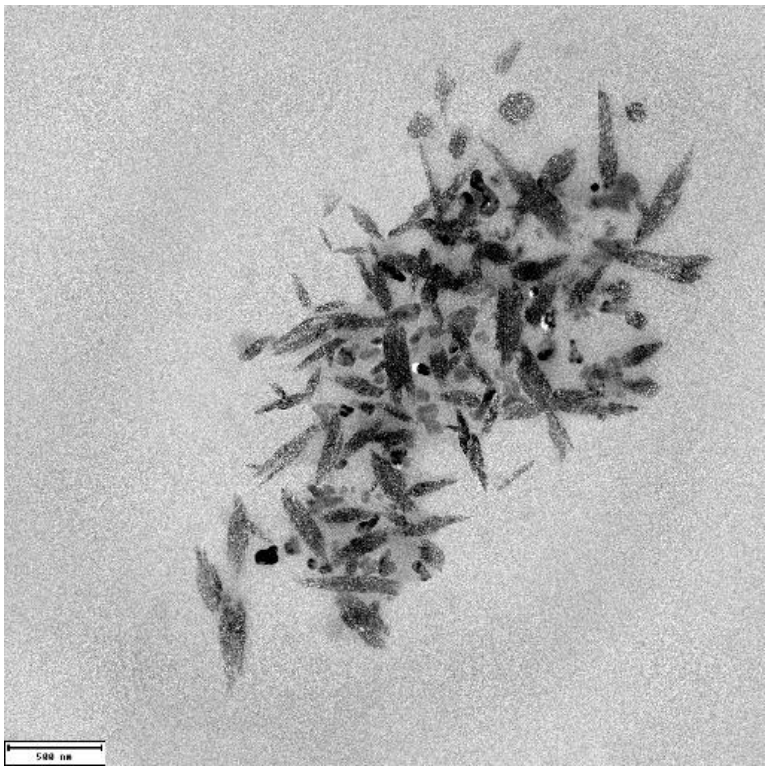

Figure 61. TEM image of unidentified particle in the 88 micron powder sample, the scale size is 500 nm.

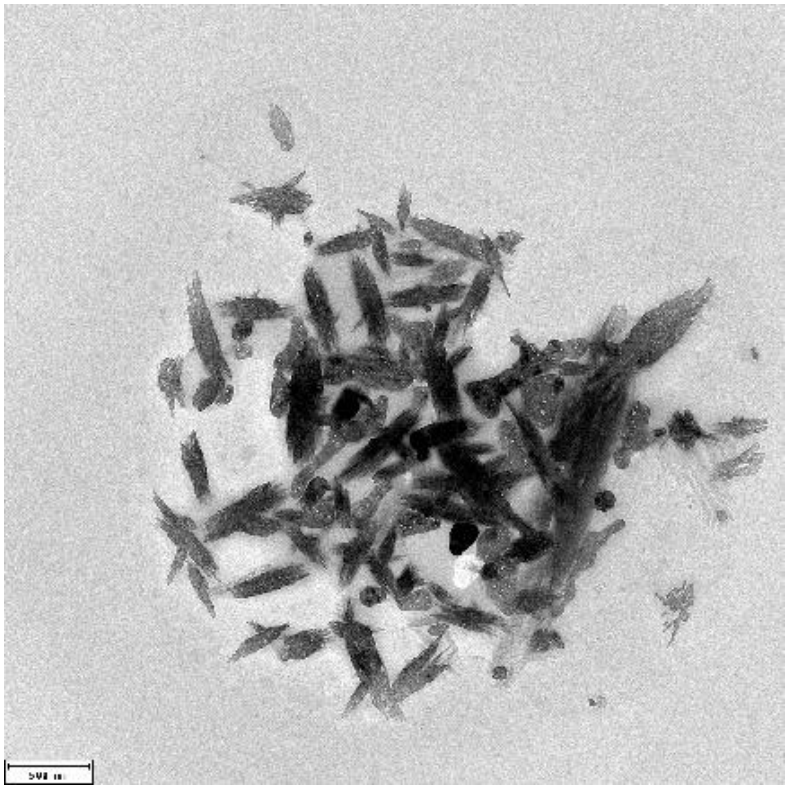

Figure 62. TEM image of unidentified particle in the 88 micron powder sample, the scale size is 500 nm.

Appendix C: Images of the used Equipment

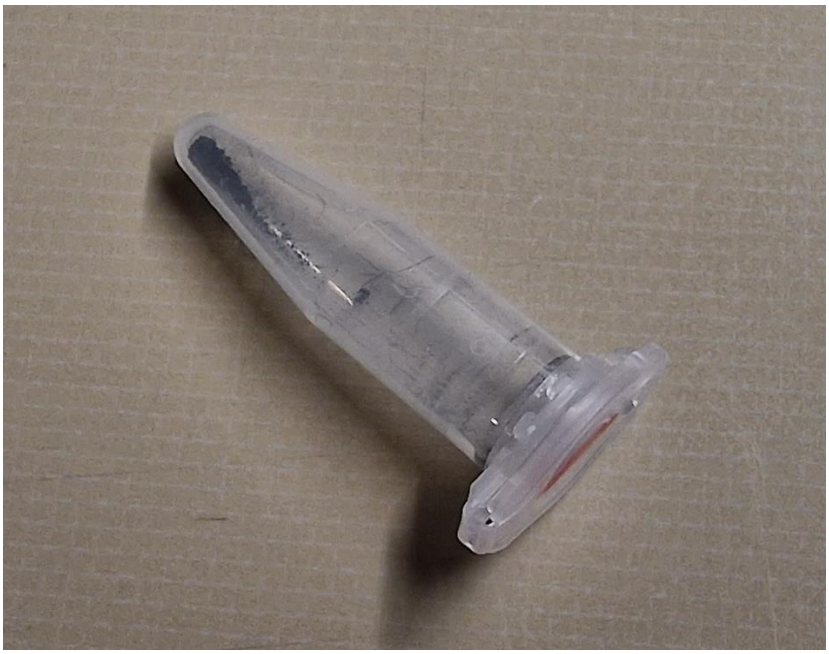

Figure 63. Microcentrifuge tubes used for storing samples.

Figure 64. Bottom bracket of the flotation column, wear on the contact surfaces can be observed.

Figure 65. Image of the used mass flow controller.

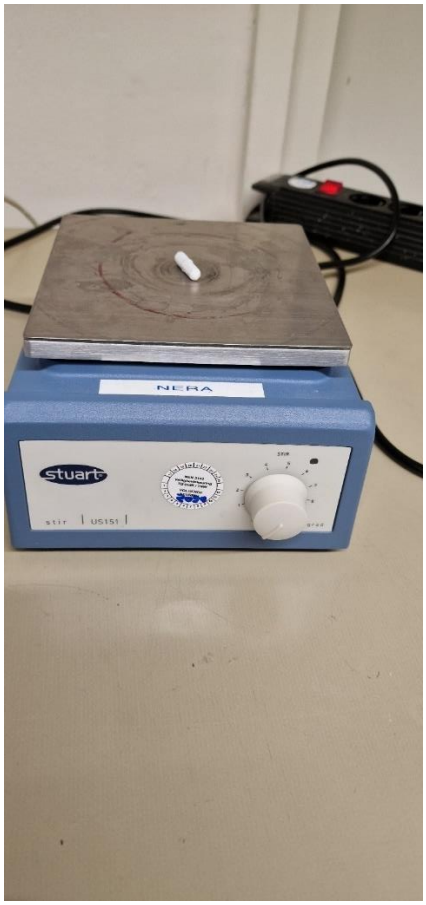

Figure 66. Image of the magnetic mixer used in two-phase flows.

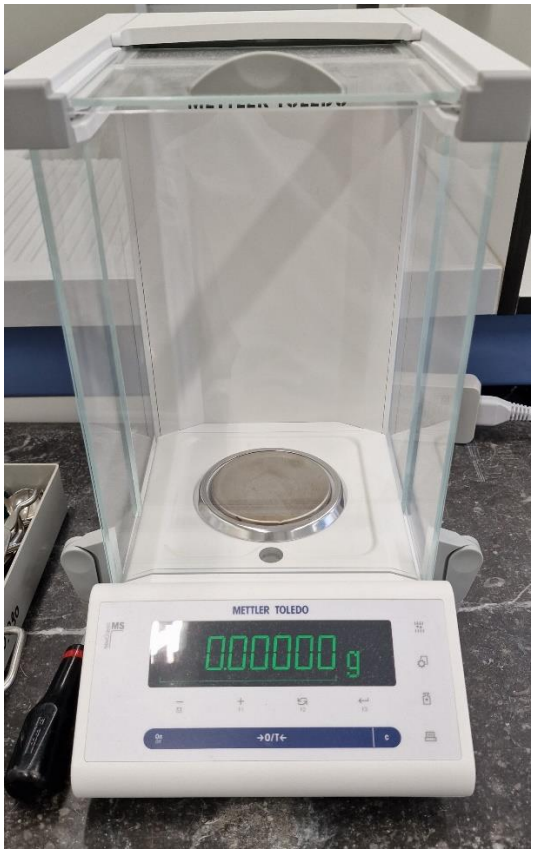

Figure 67. Image of the scale used for sample preparation.

Appendix D: Code

Coding is available at:
https://github.com/siovanovici/LDA-Data-Processing